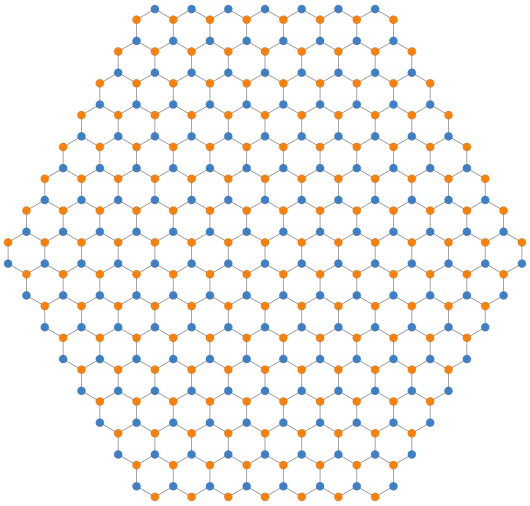

From the 1D Schrödinger Infinite Well to Dirac-Weyl Graphene Flakes

Maurício Fitz de Castro Martins Quintela
Mestrado em Física
Departamento de Física e Astronomia
2019

Orientador
João Manuel Borregana Lopes dos Santos, Professor Catedrático, FCUP

Todas as correções determinadas pelo júri, e só essas, foram efetuadas.

O Presidente do Júri,

Porto, / /

Universidade do Porto

Faculdade de Ciências

Mestrado em Física

From the 1D Schrödinger Infinite Well to Dirac-Weyl Graphene Flakes

Maurício Fitz de Castro Martins Quintela

Supervisor:
Prof. Dr. João M. B. Lopes dos Santos

A thesis submitted in fulfilment of the requirements for the degree of Master of Science

at

Departamento de Física e Astronomia

Porto, December of 2019

[This page was intentionally left blank]

Acknowledgements

As one reads through this thesis, it is important for them to know that it is written according to the learning process in condensed matter physics that has been my entire year. From wrong methods to unnecessarily complex ones, and finally to a method that finally worked but required a great deal of care and generalization to more different formalisms, it has been a very fulfilling journey. This thesis is the result of many discussions (on many topics, some more sensible than others) with a very varied group of people, some of which had nothing to do with this field. These discussions had a profound impact both on my education as on my growth as a person, and for that I am thankful.

First, I'd like to express my utmost gratitude and respect to my supervisor, Professor João Lopes dos Santos, for his patience and guidance throughout this entire learning process. Despite the "phase-shift" between our schedules, we had many fulfilling and incredibly insightful discussions which helped my growth as an aspiring (and hopefully future) physicist. Secondly, I would like to thank Professor João Viana Lopes, with whom I have had many conversations on very diverse topics on my way home from the faculty, as well as on our numerous coffee breaks, and whose insights helped in gaining a different perspective when I was stuck. Thirdly, I would like to thank my friends, among which I mention specifically Simão, Ana, Guilherme, Maria, João Pires and João Guerra, for our countless (and senseless) conversations about nothing in particular at lunch and coffee, and for their encouragement during this entire process. Despite not being mentioned by name, I also wholeheartedly thank everyone that took an important role in my life during these past two-and-a-half years. A thank you is also owed to all the professors and staff in the department of physics, whose worked contributed profoundly to my academic development. Lastly, and most importantly, I would like to thank my mother Manuela, as well as my grandparents Armanda and Fernando and my uncles Rui and Fernando João, for their immense love and their unconditional support all of these years in my studies in this sometimes cryptic area.

The author acknowledges financing of Fundação da Ciência e Tecnologia, of COMPETE 2020 program in FEDER component (European Union), through projects POCI-01-0145-FEDER-028887 and UID/FIS/04650/2013. The author also acknowledges financial support from Fundação para a Ciência e Tecnologia, Portugal, through national funds, co-financed by COMPETE-FEDER (grant M-ERA- NET2/0002/2016 - UltraGraf) under the Partnership Agreement PT2020.

[This page was intentionally left blank]

Abstract

The initial objective of this thesis was to study the angle dependence of the spectrum for the regions of dominant AA-stacking in twisted bilayer graphene using a continuum method. These regions are hexagonal, which means that we must first find a way to solve the Dirac-Weyl equation in polygonal enclosures.

Due to the inexistence of analytical solutions of partial differential equations for most polygonal enclosures, we replicate a method used originally in the study of flexural vibrations of regular polygonal plates. With this method, we obtain the low-energy eigensystem of Schrödinger's equation in polygons with hard boundaries, which we compare to existing exact theoretical results, and to numerical diagonalization of the Laplacian operator.

To address the spectrum of the Dirac-Weyl equation in finite regions, we first review possible types of boundary conditions and generalize the polynomial method for two component spinors. We were able to replicate an exact solution for a triangular flake with boundary conditions such as found in graphene zigzag edges. We found, however that this is a very special case, essentially equivalent to the solution of Schrödinger's equation. We also studied hexagonal and square shaped flakes with more general boundary conditions, which constitute a non-trivial generalization of the polynomial method for two-component spinors.

Resumo

Esta tese tinha como objectivo inicial o estudo da dependência angular do espectro para as regiões de stacking-AA dominante em grafeno twisted bilayer, utilizando para isso um modelo de contínuo. Estas regiões são hexagonais, o que cria a necessidade de encontrar um métod para a resolução da equação de Dirac-Weyl em regiões poligonais.

Devido à inexistência de soluções analíticas de equação diferenciais ás derivadas parciais para a maior parte das regiões poligonais, replicamos um método utilizado originalmente para o estudo de vibrações flexurais de placas poligonais encastradas. Com este método conseguimos obter o sistema-próprio da equação de Schrödinger em polígonos com fronteiras rígidas, soluções estas que comparamos com os resultados teóricos existentes, assim como com diagonalização numérica do operador Laplaciano.

Para tratar o espectro da equação de Dirac-Weyl em regiões finitas, começamos por rever as condições fronteira possíveis, assim como generalizar o método polinomials para spinors de dois componentes. Reproduzimos uma solução exact para um floco triangular com condições fronteira como as encontradas em flocos de grafeno com fronteiras em zigzag. Concluímos, no entanto, que este se trata de um caso especial, essencialmente equivalente à solução da equação de Schrödinger. Também estudamos os flocos hexagonais e quadrados com condições fronteira mais gerais, que constituem uma generalização não-trivial do método polinomial para spinors de dois componentes.

Keywords: graphene, twisted bilayer, Dirac-Weyl, continuum, zero-energy, Schrödinger, polynomial, edge-states

[This page was intentionally left blank]

Contents

List of Figures

[This page was intentionally left blank]

1. Introduction

1.1. A Brief Overview of the Existing Literature and Our Motivations

Ever since the discovery and isolation of graphene in 2004 by Geim and Novoselov [1, 2], this material has been the focus of many theoretical and experimental studies. In particular, the Dirac-cone structure that gives graphene massless fermions [2], leading to both fractional [3] and unconventional integer [4, 5, 6] quantum Hall effects, ultrahigh carrier mobility, and many other novel and interesting phenomena. In 2007 and 2012, Lopes dos Santos, Peres, and Castro Neto [7, 8] discussed the renormalization of the Fermi velocity in twisted bilayer graphene for low twist angles using a continuum model, as well as the the relation between discrete energy levels at zero in regions of dominant AA-stacking (regions which display a clear hexagonal structure) and the appearance of strong localization and dispersionless bands. In these articles, the authors stated by reviewing with a more symmetry based approach the geometric conditions for the presence of a commensurate structure, which is defined by the appearance of a periodic moiré superlattice. These geometric conditions had previously been considered by both Mele [9], and Shallcross *et al* [10]. The authors formulate the continuum model by spatially-modulating the interlayer hoppings, which allows them to analytically define its Fourier components, valid for small angles and any type of structure (commensurate or not). Other authors also tackled the problem of the continuum model of twisted bilayer graphene, among which we salient Bistritzer and MacDonald [11] that first measured the oscillations of the Fermi velocity at the magic angles, and Shallcross *et al* [12].

More recently, the focus in twisted bilayer graphene has reemerged with the discovery of superconducting states (with a critical temperature up to $T_c \sim 1.7\,K$) at very specific angles [13]. Among all the articles that attempt to explain this phenomena, we will emphasize works from Peltonen *et al* [14], Lin and Tománek [15], Moon and Koshino [16], Zhang [17], and Tarnopolsky *et al* [18], works which we will now briefly summarise.

Peltonen *et al* [14] utilize the previously mentioned continuum model's Hamiltonian to first study the normal state at low energy. Following from that, they introduce a Coulomb pseudo-potential in a BCS-type [19] mean field model, with which the authors are able to derive a self-consistency equation. This equation allows them to find a critical value for the order parameter and, therefore, the mean-field critical temperature. This allows them to put an upper bound on the transition temperature from 3K to 20K.

Lin and Tománek [15] construct a tight-binding Hamiltonian considering only three parameters extracted from both monolayer graphene and untwisted bilayer graphene. With this model, the authors are able to reproduce the electronic structure of twisted bilayer graphene, including the value of the first angle where the bands at the Fermi energy flatten (without an overlap) and two gaps open, one on either side. The authors were also able to predict the next two angles where this phenomena occurs again.

Moon and Koshino [16] utilize a tight-binding Hamiltonian similar to that of Tománek, in which they introduce a uniform perpendicular magnetic field. The authors work through the process of Peierls substitution [20], through which they are able to write the tight-binding wavefunctions and diagonalize the Hamiltonian matrix. They finally study the energy spectrum, Hall conductivity and the band structure for several commensurate angles, as well as describing the evolution from the semi-classical Landau levels to the fractal band structure, for which they obtain the minimum magnetic field (as a function of the angle) required for its formation.

Zhang [17] starts again by taking the continuum limit and recapitulating the moiré band structure. With this model, the author focuses on the spatially modulated Dirac mass term that appears from the interlayer hopping part of the Hamiltonian. This term generates a vortex structure around the center of specific stacking regions, which form an emergent honeycomb lattice. Projecting the Dirac Hamiltonian onto the subspace of the zero-energy states (zero modes), the author obtains a tight-binding model on the emergent honeycomb lattice. Using this effective Hamiltonian of the low-energy moiré band (which becomes extremely flat at the magic angle), given by a Hubbarb model [21], the author is able to derive the existence of a Mott insulating phase [22].

Tarnopolsky *et al* [18] start also from a continuum model, with which they solve the zero-mode Dirac equation [23], finding that at exactly at the magic-angles (where the wavefunction is zero at the center of BA-stacking regions) the obtained wave functions of the flat band satisfy the zero-mode equation in the entire moiré Brillouin Zone and become localized in the AA-stacking regions. The authors then study the dependence of the Fermi velocity on the twist angle, which leads them to do perturbation theory in $\frac{1}{\theta}$ (θ being the twist angle). This perturbation theory reveals a certain periodicity in the magic angles, as well as a calculated first magic angle extremely close to the one that is measured experimentally.

As the AA-stacking regions of twisted bilayer graphene appear to be fundamental in understanding the physics of this material, the focus of this thesis will be the development of an analytical method to obtain their spectrum, using a continuum model. This method may be adapted for other purposes in the future, for example including the presence of a magnetic or electric field. As these regions are hexagonal, we will first attempt to find a way of solving differential equations on these sorts of polygonal enclosures. This proved to be quite a challenge, as we were unable to find any exact solutions of the Dirac-Weyl equation [23, 24] in bidimensional enclosures taking into account different boundary conditions in the existing literature.

We found, however, a solution based on numerical integration of partial differential equations in an article by Zarenia *et al* [25]. For us to be able to analyze and reproduce this article, we would need to find a way to write functions that obey the necessary boundary conditions. As such, we first tackle Schrödinger's equation [26] as it is simpler to both visualize and impose boundary conditions.

1.2. Structure of this thesis

The second chapter begins by attempting to solve Schrödinger's equation in polygonal plate enclosures. This method is necessary because, while some enclosures are trivial due to the simplicity of performing separation of variables (square and circle, for example), others are not so simple and require an intensive use of the group symmetries (the triangle [27], for example), and for others like the hexagon no exact solution was found in the literature. To obtain the spectrum of these non-trivial enclosures, we first attempt several approaches before settling on the orthogonal plate function method, introduced by Liew and Lam [28], and Bhat [29]. Using this technique, we first test it against the purely academic 1-dimensional infinite potential well, with which we can verify its validity and rate of convergence. Afterwards, we use its 2-dimensional generalization to compare against the exact results for the square infinite potential well, as well as testing a pre-diagonalization approach by taking advantage of the symmetries of the enclosure in question. We apply this technique to find the spectrum for an hexagonal infinite well, which we compare against both the solutions from numerical integration and the group symmetry separation method. To close the chapter, we study the evolution of the spectra from the polynomial method as a function of the number of sides of the enclosing polygon.

In the third chapter we begin by generalizing the orthogonal plate functions method so that we can use it to work with Dirac billiards. For that, we begin by solving the 1-dimensional case for arbitrary boundary conditions, which we then use to test the validity of the new method. We also discuss the necessary changes when treating a boundary with generic orientation and boundary conditions. Afterwards, we review Gaddah's [30] solution for the triangular Dirac billiards with boundary conditions equivalent to zigzag in the discrete. Following from this, we utilize a modified version of our polynomial method developed for the Schrödinger problem to obtain the spectrum and some of the lowest-energy eigenfunctions. After that, we work on writing the Dirac-Weyl equation in polar coordinates so that we can treat the circular well with infinite mass confinement boundary conditions.

In the fourth chapter, we utilize the polynomial approach to study the square with infinite mass confinement in all of the edges. We study the convergence of the spectrum, and utilize the Helmholtz equation to obtain the low-energy eigenfunctions. We then discuss the possibility of having zero-energy states for the Dirac equation in a polygonal-enclosure.

In the fifth and final chapter, we return to the problem of graphene. After numerically integrating the Dirac equation, we discuss the origin of exactly-zero energy states in tight-binding models. We then discuss the validity of Zarenia *et al* [25]'s results. Following from that, we apply the polynomial method for the zigzag-boundary hexagon and obtain its spectrum. We then utilize the Helmholtz equation in the same system, where we obtain matching results. Finally, we discuss the similarities between the results for the triangle and the hexagon, and the equivalence of the two systems.

2. Classical Regime: Schrödinger's Equation

We want to find a method of obtaining the low energy spectrum of an arbitrary (convex polygonal) plane enclosure with Schrödinger's equation. For that, we start by solving Schrödinger's equation in polar coordinates for the circle, where we find the well-known solutions given by the Bessel Functions of the first kind [31].

Secondly, we attempt a decomposition of the enclosure into triangular wedges to simply the treatment and facilitate the imposition of boundary conditions. After several manipulations of the resulting equations, we arrive at the conclusion that we are simply doing a polynomial fit and that there must be a simpler way of doing so.

After that, we apply the technique introduced by Liew and Lam [28] to the 1D infinite well, where we find very quick convergence between this polynomial method and the exact result. Following that, we compare the polynomial results for the square well with the exact energy levels for different basis sizes in order to better study the convergence of this method. Finally, we use this technique to obtain the spectrum of the hexagonal well. We also generate the higher order polynomials for each 2D enclosure using their intrinsic symmetries, which allows for a much faster calculation of the spectrum due to the orthogonality of different irreducible representations (which diagonalizes the Hamiltonian matrix by blocks and significantly speeds up the calculation of its eigenvalues).

2.1. Schrödinger's Equation in Polar Coordinates

Starting from the regular expression of the time-independent Schrödinger's equation for the free particle ($V(r) = 0$),

$$-\frac{\hbar^2}{2m}\nabla^2\psi(x,y) = E\psi(x,y) \tag{2.1.1}$$

we need to re-write the Laplacian operator in polar coordinates

$$\nabla^2 f = \frac{\partial^2 f}{\partial r^2} + \frac{1}{r}\frac{\partial f}{\partial r} + \frac{1}{r^2}\frac{\partial^2 f}{\partial \theta^2} \tag{2.1.2}$$

By direct substitution in Schrödinger's equation, we get

$$-\frac{\hbar^2}{2m}\left[\frac{\partial^2}{\partial r^2} + \frac{1}{r}\frac{\partial}{\partial r} + \frac{1}{r^2}\frac{\partial^2}{\partial \theta^2}\right]\psi(r,\theta) = E\psi(r,\theta) \tag{2.1.3}$$

To solve this, we assume a complete set of functions that will have the form

$$\psi_m(r,\theta) = R_m(r)\,\Theta_m(\theta) \tag{2.1.4}$$

with

$$\Theta_m(\theta) = e^{im\theta} \tag{2.1.5}$$

This gives us

$$\frac{-\hbar^2}{2m}\left[\frac{\partial^2 R_m(r)}{\partial r^2}\Theta_m(\theta) + \frac{1}{r}\frac{\partial R_m(r)}{\partial r}\Theta_m(\theta) + \frac{R_m(r)}{r^2}\frac{\partial^2\Theta_m(\theta)}{\partial\theta^2}\right] = ER_m(r)\,\Theta_m(\theta) \tag{2.1.6}$$

Defining $k^2 = \frac{2mE}{\hbar^2}$, and dividing by ψ, we get the two equations

$$\frac{\partial^2\Theta_m(\theta)}{\partial\theta^2} + m^2\Theta_m(\theta) = 0 \tag{2.1.7}$$

$$\frac{\partial^2 R_m(r)}{\partial r^2} + \frac{1}{r}\frac{\partial R_m(r)}{\partial r} + \left(k^2 - \frac{m^2}{r^2}\right)R_m(r) = 0 \tag{2.1.8}$$

The solutions of the Θ equation are of the form $e^{\pm im\theta}$, and are single-valued only if m is an integer. This quantum number is the L_z angular momentum.

The radial equation is a very well-known equation in mathematical physics, the Bessel equation. We must solve it with two conditions:

1. The wave function must vanish at the wall ($r = a$);
2. The wave function must be finite at $r = 0$.

Fortunately, the Bessel equation has been thoroughly studied and its solutions are well known.

2.1.1. Energy Spectrum

As we saw previously, the solutions for Schrödinger's equation in this boundary are just

$$\psi_m(qr) = e^{im\theta}\mathcal{J}_m(qr) \tag{2.1.9}$$

where $\mathcal{J}_m$ are the same Bessel functions as before. We want to find the zeros of these functions for a specific $r = R$ to satisfy boundary conditions. The order of the zero will be closely related to number of nodes of the function. As the exponential will only create sinusoidal oscillations around the circular boundary (breaking the θ symmetry and creating an angular modulation of these modes), and we want the zeros of the modulus, we can focus only on the Bessel function itself, i.e. finding qR so that

$$\mathcal{J}_m(qR) = 0 \tag{2.1.10}$$

Looking at four values of $m \in [0, 3]$ (just for visualization) for the same range of qR as we used before, we obtain Figure 2.1.1:

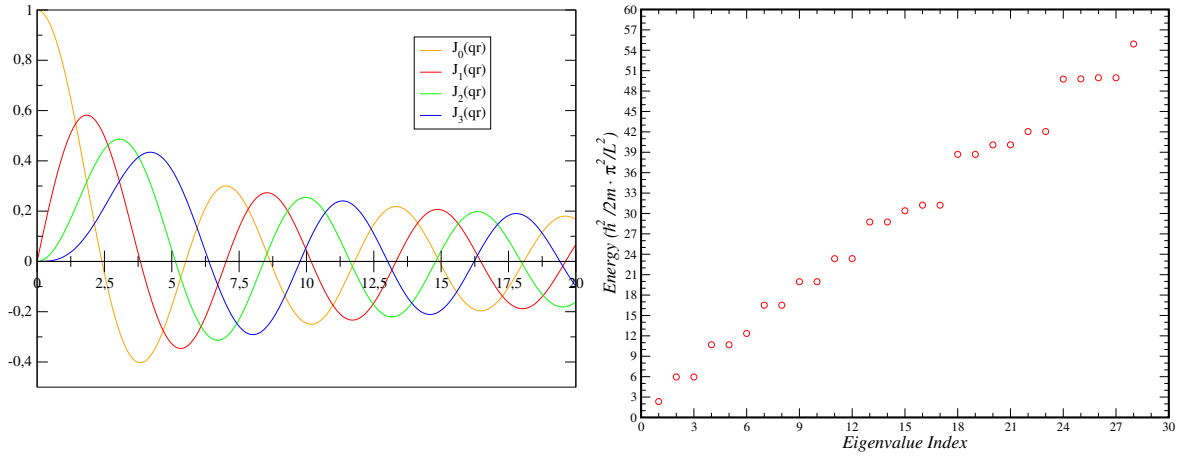

Figure 2.1.1.: (Left) Plot of $\mathcal{J}_m$ with $m \in [0, 3]$
(Right) Energy Spectrum in units of $\frac{\hbar^2}{2m}\left(\frac{\pi}{2}\right)^2$.

From this, we get the expected energy levels for the circular infinite potential well with Schrödinger's equation:

$$E_{n,m} = \frac{\hbar^2}{2m}\left(\frac{k_{n,m}}{R}\right)^2 \tag{2.1.11}$$

where $k_{n,m} = (qR)_{n,m}$ is the n^{th} zero of the Bessel function $\mathcal{J}_m(qR)$.

2.1.2. Fourier Shape Transform

Suppose we have a region with a boundary defined by $r(\theta)$ and want to find the spectrum of a free particle confined to such a region, i.e. with boundary condition $\psi(r(\theta),\theta)=0$. Let us write $r(\theta)=c\rho(\theta)$, where c is some length scale characteristic of the enclosure and ρ a dimensionless function.

The wave function will be a superposition of plane waves with a given energy E

$$\psi(r,\theta)=\int_0^{2\pi} d\varphi f(\varphi)e^{i\overrightarrow{q}\cdot\overrightarrow{r}} \tag{2.1.12}$$

where q in the case of Schrödinger's equation is

$$q=\sqrt{2mE/\hbar^2} \tag{2.1.13}$$

In polar coordinates, we have

$$\overrightarrow{q}\cdot\overrightarrow{r}=qr\left(\cos\varphi\cos\theta+\sin\varphi\sin\theta\right)=qr\cos\left(\varphi-\theta\right) \tag{2.1.14}$$

To impose the boundary condition

$$\int_0^{2\pi} d\varphi f\left(\varphi\right)e^{iqr(\theta)\cos(\varphi-\theta)}=\int_0^{2\pi} d\varphi f(\varphi)e^{iqc\rho(\theta)\cos(\varphi-\theta)}=0 \tag{2.1.15}$$

A complete set of functions of φ is

$$g\left(\varphi\right)=\sum_m g_m e^{im\varphi} \tag{2.1.16}$$

where

$$g_m=\frac{1}{2\pi}\int_0^{2\pi} d\varphi g\left(\varphi\right)e^{-im\varphi} \tag{2.1.17}$$

For a function of two angular variables,

$$g\left(\theta,\varphi\right)=\sum_{m,n} g_{n,m}e^{in\theta}e^{im\varphi} \tag{2.1.18}$$

where $g_{n,m}$ is the 2D-analogous of the previous Fourier amplitudes,

$$g_{n,m}=(2\pi)^{-2}\int_0^{2\pi}\int_0^{2\pi} d\varphi d\theta g\left(\theta,\varphi\right)e^{-in\theta}e^{-im\varphi} \tag{2.1.19}$$

As such,

$$\psi\left(r\left(\theta\right),\theta\right)=\sum_m g_m\int_0^{2\pi} d\varphi e^{im\varphi}e^{iqc\rho(\theta)\cos(\varphi-\theta)}=\sum_{m,\,n} g_m h_{n,-m}\left(qc\right)e^{in\theta}=0 \tag{2.1.20}$$

where

$$h_{n,m}\left(qc\right)=\int_0^{2\pi} d\theta\int_0^{2\pi} d\varphi e^{-in\theta}e^{-im\varphi}e^{iqc\rho(\theta)\cos(\varphi-\theta)} \tag{2.1.21}$$

The boundary condition is

$$\sum_m h_{n,-m}(qc)\, f_m = 0 \tag{2.1.22}$$

The homogeneous linear equation (Equation 2.1.21) must have a non-zero solution given by a linear combination of the coefficients f_m. The eigenvalues are determined by the zeros of the determinant of the matrix $h_{n,m}(qc)$,

$$\det h_{n,m}(qc) = 0 \tag{2.1.23}$$

This matrix is infinite, but we can assume an approximation with a finite dimension and check the evolution of the eigenvalues as the basis size increases.

To parameterize the edges of regular polygon as a function of only θ, we want to write $r(\theta) = c\rho(\theta)$. To do this, we take the Fourier shape transform [32] of the polygon to parameterize the edge. This transform has the coefficients

$$\alpha_{j\ m+b} = \left(\frac{m}{\pi(jm+b)} \sin\left(\frac{\pi}{m}\right)\right)^2 \tag{2.1.24}$$

where j is the summation index, m is the number of sides and b describes how the vertexes are connected (basically connecting the b^{th} neighbors). As such, we have the truncated series up to order k

$$\rho_k(\theta) = \left|\sum_{j=-k}^{k} \alpha_{j\ m+b} e^{i(jm+1)\theta}\right| \tag{2.1.25}$$

The $+1$ in the exponent can be factorized, as it has no dependence on the sum. Taking it out of the sum, its modulus is just 1 so it vanishes.

$$\rho_k(\theta) = \left|\sum_{j=-k}^{k} \alpha_{j\ m+b} e^{i(jm)\theta}\right| \tag{2.1.26}$$

This expression clearly displays a $\theta \to \theta + \frac{2\pi}{m}$ symmetry: by direct substitution, the new factor will just be $e^{i2\pi \cdot j} = 1$. A comparison of this series approximation is visible in Figure 2.1.2.

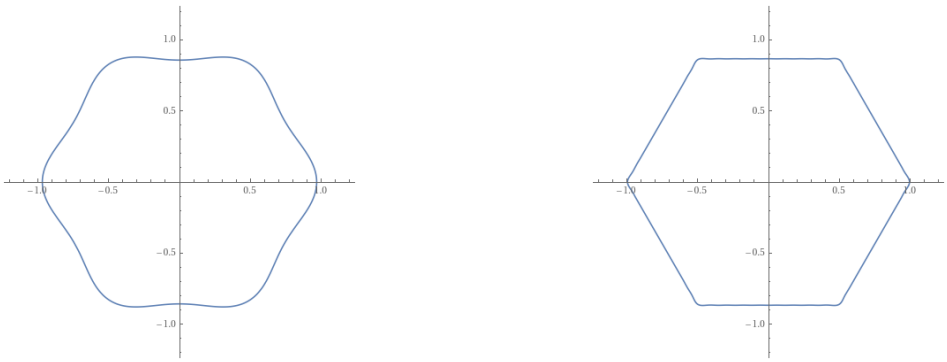

Figure 2.1.2.: Fourier shape transform of an hexagon with $k = 1$ (left) and $k = 8$ (right).

By manipulating Equation 2.1.21, and defining $\alpha = \phi - \theta$, we find that

$$\begin{aligned} h_{n,m}(qc) &= \int_0^{2\pi} d\theta \int_0^{2\pi} d\varphi e^{-in\theta} e^{-im\varphi} e^{iqc\rho(\theta)\cos(\varphi-\theta)} \\ &= \int_0^{2\pi} d\theta \int_0^{2\pi} d\alpha e^{-in\theta} e^{-im\theta} e^{-im(\varphi-\theta)} e^{iqc\rho(\theta)\cos(\varphi-\theta)} \\ &= \int_0^{2\pi} d\theta e^{-in\theta} e^{-im\theta} \int_0^{2\pi} d\alpha e^{i(-m\alpha+qc\rho(\theta)\cos(\alpha))} \\ &= \frac{1}{2\pi} \int_0^{2\pi} d\theta e^{-i(n+m)\theta} \mathcal{J}_{-m}\left[qc\rho_k(\theta)\right] \end{aligned} \tag{2.1.27}$$

What we want to find are the zeros of

$$\det\left[h_{n,m}(qc)\right] = \det\left[\frac{1}{2\pi} \int_0^{2\pi} d\theta e^{-i(n+m)\theta} \mathcal{J}_{-m}\left[qc\rho_k(\theta)\right]\right] \tag{2.1.28}$$

Unfortunately, this method failed to provide a spectrum that was satisfactory for any matrix size tested. As such, we need to find a different method to treat the edges.

2.1.3. More Suitable Coordinates?

Suppose now that we want to solve Schrödinger's equation in a wedge with $\theta \in \left[-\frac{\pi}{n}, \frac{\pi}{n}\right]$ and $x \in [0, a]$ with periodic boundary conditions $\psi\left(x, -\frac{\pi}{n}\right) = \psi\left(x, \frac{\pi}{n}\right)$ and $\psi(a, \theta) = 0$, where n is the number of sides of the polygon we want to decompose in triangular wedges, as seen in Figure 2.1.3.

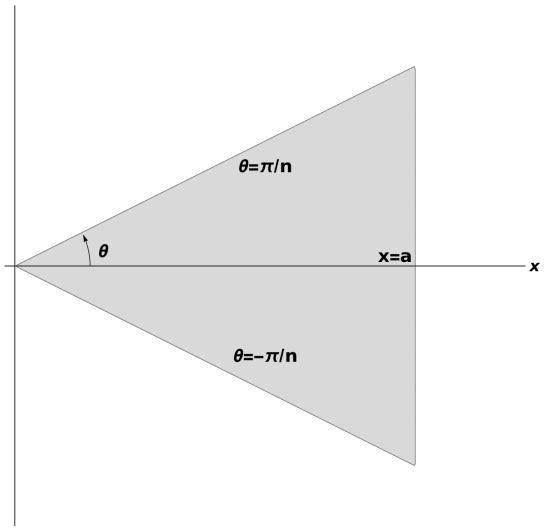

Figure 2.1.3.: Triangular wedge with the new coordinate system.

Defining a new coordinate system from the usual polar coordinates, we have

$$\begin{aligned} x &= r\cos\theta \\ \phi &= \theta \end{aligned} \tag{2.1.29}$$

with the inverse transformation

$$\begin{aligned} r &= \frac{x}{\cos\phi} \\ \theta &= \phi \end{aligned} \tag{2.1.30}$$

In these new coordinates, the boundary conditions for s-type states (invariant under rotations) are exactly the ones we are looking for:

$$\psi\left(a,\phi\right) = 0 \tag{2.1.31}$$

$$\psi\left(x,-\frac{\pi}{n}\right) = \psi\left(x,\frac{\pi}{n}\right) \tag{2.1.32}$$

We, however, lost the orthogonality between the coordinates. Therefore, we need to find the metric. In polar coordinates, the invariant interval is

$$ds^2 = dr^2 + r^2 d\theta^2 \tag{2.1.33}$$

Rewriting the infinitesimal segments in our new coordinates, we have

$$dr = \frac{1}{\cos\phi}dx + \frac{x\sin\phi}{\cos^2\phi}d\phi \tag{2.1.34}$$

by direct substitution, we get

$$\begin{aligned} ds^2 &= \frac{1}{\cos^2\phi}dx^2 + 2\frac{x\sin\phi}{\cos^3\phi}dxd\phi + \left(\frac{x^2\sin^2\phi}{\cos^4\phi} + \frac{x^2}{\cos^2\phi}\right)d\phi^2 \\ &= \frac{1}{\cos^2\phi}\left[dx^2 + 2x\tan\phi dxd\phi + x^2\left(1+\tan^2\phi\right)d\phi^2\right] \end{aligned} \tag{2.1.35}$$

The metric tensor can be obtained from this equality remembering that

$$ds^2 = g_{\mu\nu}dx^\mu dx^\nu \tag{2.1.36}$$

which gives us

$$g_{\mu\nu} = \frac{1}{\cos^2\phi}\begin{bmatrix} 1 & x\tan\phi \\ x\tan\phi & \frac{x^2}{\cos^2\phi} \end{bmatrix}$$

The inverse of this tensor, which we need to obtain the Laplacian operator, is given by

$$g^{\mu\nu} = \begin{bmatrix} 1 & \frac{-\cos\phi\sin\phi}{x} \\ \frac{-\cos\phi\sin\phi}{x} & \frac{\cos^2\phi}{x^2} \end{bmatrix} \tag{2.1.37}$$

which, by direct application, gives us the expected result

$$g^{\mu\rho}g_{\rho\nu} = \delta^{\mu}_{\ \nu} \tag{2.1.38}$$

With this, the Laplacian operator is obtain directly from its definition

$$\begin{aligned} g^{\mu\nu}\partial_\mu\partial_\nu &= \partial_x^2 - \frac{2\sin\phi\cos\phi}{x}\partial_x\partial_\phi + \frac{\cos^2\phi}{x^2}\partial_\phi^2 \\ &= \partial_x^2 - \frac{\sin(2\phi)}{x}\partial_x\partial_\phi + \frac{\cos^2\phi}{x^2}\partial_\phi^2 \end{aligned} \tag{2.1.39}$$

The problem we are now solving is

$$-\frac{\hbar^2}{2m}\left[\partial_x^2 - \frac{\sin(2\phi)}{x}\partial_x\partial_\phi + \frac{\cos^2\phi}{x^2}\partial_\phi^2\right]\psi(x,\phi) = E\psi(x,\phi) \tag{2.1.40}$$

with boundary conditions

$$\begin{aligned} \psi(a,\theta) &= 0 \\ \psi\left(x,-\frac{\pi}{n}\right) &= \psi\left(x,\frac{\pi}{n}\right) \end{aligned} \tag{2.1.41}$$

The solution has the form

$$\psi(x,\phi) = \sum_p f_p(x)\, e^{ipn\phi}, \;\; p \in \mathbb{Z} \tag{2.1.42}$$

and the functions of x satisfy the boundary condition

$$f_p(a) = 0 \tag{2.1.43}$$

The fundamental question now is: can we find a reasonable answer with a variational function

$$\begin{aligned} \psi(x,\phi) &= \sum_{p=0}^{N} c_p\left[x^{pn}(a-x)\right]\left(e^{ipn\phi} + e^{-ipn\phi}\right) \\ &= \sum_{p=0}^{N} c_p\varphi(x,\phi) \end{aligned} \tag{2.1.44}$$

by choosing the coefficients c_p? These f_p functions are chosen for two reasons:

- they are zero at $x = a$, thus enforcing automatically the boundary condition of Equation 2.1.31;
- they present the same asymptotical behaviour has the Bessel functions (which we know are the solutions for the circular well) in the neighbourhood of $x = 0$.

As these functions are bounded and will converge quickly (since they behave like Bessel functions near the origin), we do not need to use an unreasonably large N to have their full

behaviour. We now want to find the energy levels for these wave functions. Applying each one of the derivatives of the Laplacian operator to ψ_s, we have that

$$\partial_x^2 \psi_s(x,\phi) = \sum_{p=0}^{N} a^{pn-1} c_p \left[pn(pn-1)\left(\frac{x}{a}\right)^{pn-2}\left(1-\frac{x}{a}\right) - 2pn\left(\frac{x}{a}\right)^{pn-1}\right]\left(e^{ipn\phi}+e^{-ipn\phi}\right) \tag{2.1.45}$$

$$\partial_x \partial_\phi \psi_s(x,\phi) = \sum_{p=0}^{N} a^{pn} c_p \left(\frac{x}{a}\right)^{pn-1}\left[pn\left(1-\frac{x}{a}\right)-\frac{x}{a}\right]\left[ipn\left(e^{ipn\phi}-e^{-ipn\phi}\right)\right]$$

$$\partial_\phi^2 \psi_s(x,\phi) = \sum_{p=0}^{N} a^{pn+1} c_p \left(\frac{x}{a}\right)^{pn}\left(1-\frac{x}{a}\right)(ipn)^2\left(e^{ipn\phi}+e^{-ipn\phi}\right)$$

Multiplying by each respective geometric factor, we get

$$\begin{aligned}\nabla^2 \psi_s(x,\phi) = \sum_{p=0}^{N} a^{pn-1} c_p \Bigg\{ &\left[\left(pn(pn-1)\left(\frac{x}{a}\right)^{pn-2}\left(1-\frac{x}{a}\right) - 2pn\left(\frac{x}{a}\right)^{pn-1}\right)\left(e^{ipn\phi}+e^{-ipn\phi}\right)\right] + \\ &+ \left(\frac{x}{a}\right)^{pn-1} ipn\left(e^{ipn\phi}-e^{-ipn\phi}\right)\left(1-pn\left(1-\frac{x}{a}\right)\right)\left(\frac{e^{i2\phi}-e^{-i2\phi}}{2i}\right) \\ &+ \frac{1}{2}\cdot\left(\frac{x}{a}\right)^{pn-2}\left(1-\frac{x}{a}\right)(ipn)^2\left(e^{ipn\phi}+e^{-ipn\phi}\right)\left(1+\frac{e^{i2\phi}+e^{-i2\phi}}{2}\right)\Bigg\}\end{aligned} \tag{2.1.46}$$

This expression quickly became unwieldy, and we would need to fix not only the continuity in the ϕ edges, but also the continuity of the derivatives in these same edges so that we could glue them together (even if we added an angular momentum term).

We are essentially applying a polynomial fit and then solving a functional eigenvalue problem. As such, there must be a better way to apply these same principles to a simple polynomial model.

2.2. A "New" Approach: Orthogonal Plate Functions

The problem of vibrations of plates of different shapes has been studied intensively throughout history [33] for many applications in different fields of engineering. The obtained results were usually for rectangular, circular, elliptical or triangular plates as the study for more general plates was limited due to the implicit relation between the two variables describing the plate geometry. In 1987, Bhat [29] wrote an article describing a method of applying characteristic polynomials to create of functions with which one can solve the eigenvalue problem for more general enclosures. Following from that, in 1990 Liew, Lam and Chow [34] study the convergence of this method for a rectangular plate by comparing the obtained vibration modes against the exact results. Finally, in 1991, Liew and Lam [28] formalize this method for different boundary conditions (i.e., edges with both $\phi = \nabla\phi = 0$ versus edges with just $\phi = 0$ versus free edges) and also by taking into account the thickness of the plates, the maximum strain for a harmonic vibration, and the rigidity of the plate.

As we will utilize this method for the study of Schrödinger's equation, we will first test it for the simple case of the one-dimensional infinite potential well.

2.2.1. One-Dimensional Problem

Let us first consider the well-known problem of the one-dimensional infinite potential well of size L. Let us also suppose that we want to write the solutions to this problem as a basis that satisfies boundary conditions. The simplest polynomial that goes to zero in the edges is just

$$\phi_1(x) = N_1 x(L - x) \tag{2.2.1}$$

where N_1 is a normalization factor obtained simply from setting

$$\int_0^1 dx\,(\phi_i(x))^2 = 1 \tag{2.2.2}$$

We now define the pre-normalization functions through Gram-Schmidt orthogonalization [31] as

$$\tilde{\phi}_i(x) = x^{i-1}\phi_1(x) - \sum_{j=1}^{i-1} \langle x^{i-1}\phi_1(x)\,|\phi_j(x)\rangle \phi_j(x) \tag{2.2.3}$$

where the scalar product is defined as

$$\langle f_1(x)\,|f_2(x)\rangle = \int_0^1 dx f_1(x)\cdot f_2(x) \tag{2.2.4}$$

After orthogonalization, we finally normalize each function

$$\phi_i(x) = N_i\tilde{\phi}_i(x) \tag{2.2.5}$$

Because every function will have a factor $\phi_1(x)$ (by construction), they will immediately satisfy boundary conditions.

The Gram-Schmidt process ensures that each new basis function will be orthogonal to all

previous ones. As such, we have the orthogonality condition we were looking for

$$\langle \phi_i(x) | \phi_j(x) \rangle = \delta_{ij} \tag{2.2.6}$$

In this basis, the Hamiltonian matrix is

$$H_{ij} = -\frac{\hbar^2}{2m} \int_0^L dx \phi_i(x) \cdot \left(\nabla^2 \phi_j(x) \right) \tag{2.2.7}$$

or, in units of $\frac{\hbar^2}{2m} \frac{\pi^2}{L^2}$ as we will use throughout this thesis,

$$E_{ij} = -\frac{1}{\pi^2} \int_0^1 dx \phi_i(x) \cdot \left(\nabla^2 \phi_j(x) \right)$$

and taking its eigenvalues after truncating the basis at $i = 12$, we get

$$E = \{1.0000, 4.0000, 9.0000, 16.000, 25.001, 36.004, 49.451, 65.192, 98.216, 128.45, 352.31, 466.90\} \tag{2.2.8}$$

As we can see, the lowest energy values match the expected ones for the one-dimensional infinite potential well. By increasing the number of polynomials used, we get better and better values for the higher energies.

Comparing the exact solution for the free particle in the one-dimensional box with the one obtained from this method, we obtain convergence, which is clearly observable in Figure 2.2.1.

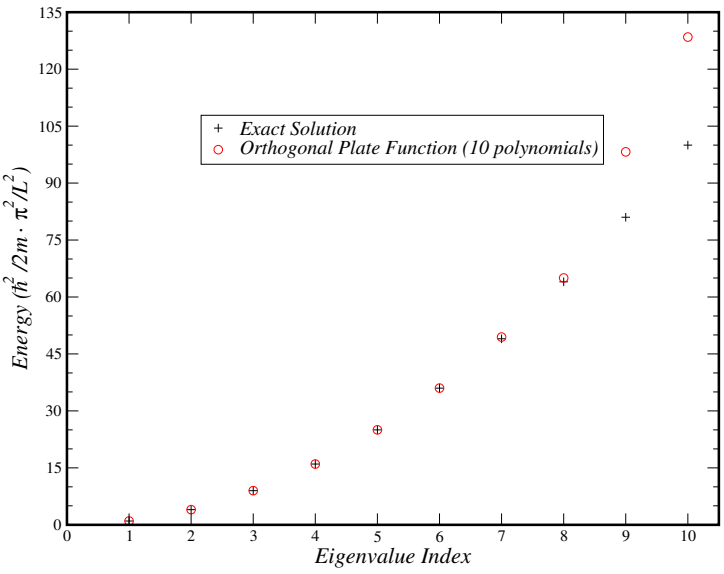

Figure 2.2.1.: Exact versus Orthogonal Plate Functions energies for a basis size of 10 polynomials.

With this formalism it is also simple to modify the potential. For example, in the case of

the harmonic potential inside the confining box

$$E_{ij} = -\frac{1}{\pi^2}\int_0^1 dx\phi_i(x)\cdot\left(\nabla^2\phi_j(x)\right) + \frac{1}{2}m\omega^2\int_0^1 dx\phi_i(x)\left(x-\frac{1}{2}\right)^2\phi_j(x) \tag{2.2.9}$$

which will change the energy eigenvalues. Defining $\alpha^2 = \frac{m^2\omega^2}{2\hbar^2}$, we have

$$E_{ij} = -\frac{1}{\pi^2}\int_0^1 dx\phi_i(x)\cdot\left(\nabla^2 - \pi^2\alpha^2\left(x-\frac{1}{2}\right)^2\right)\phi_j(x) \tag{2.2.10}$$

Looking at the energy units, one would expect to obtain the harmonic oscillator spectrum when

$$\frac{1}{2}m\omega^2\pi^2 \gg \frac{\hbar^2}{2m}\frac{\pi^2}{L^2} \tag{2.2.11}$$

which reduces simply to

$$\alpha^2 L^2 \gg 1 \tag{2.2.12}$$

Fixing $L = 1$, and setting $\alpha = 100$, we obtain the spectrum

$$E' = \{0.5007, 1.5302, 2.6756, 3.7532, 4.8532, 6.0243, 7.2103, 9.8312, 12.235, 18.247, ...\} \tag{2.2.13}$$

which, dividing by 2α due to the system of units we are using, translates into roughly the spectrum for the harmonic oscillator, visible in Figure 2.2.2. Due to the massive harmonic potential, the lowest energy states to not "feel" the potential from the walls, which makes it so they converge extremely quickly to the exact values.

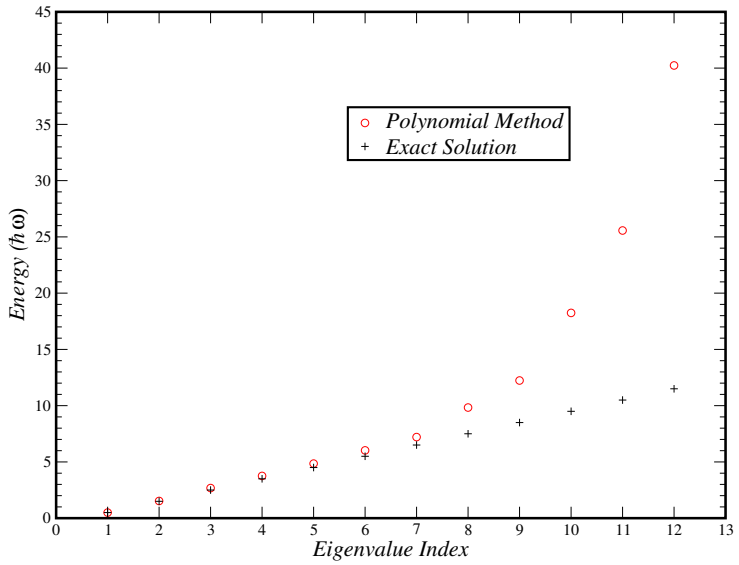

Figure 2.2.2.: Exact harmonic oscilator versus Orthogonal Plate Functions energies for a basis size of 12 polynomials.

2.2.2. Two-Dimensional Problem

In the case of the two-dimensional problem, we need to write a function ψ_i that is analogous to the ϕ_i that was used in the 1D case. Obtaining the initial polynomial does not present any problems: using the same logic as before, we can write it as

$$\psi_1(x,y) = N_1 \prod_{s=1}^{n} \varphi_s(x,y) \tag{2.2.14}$$

where n is the number of sides of the polygon and $\varphi_s(x,y)$ are the line equations for the sides of the polygon. The normalization is defined the same way as before, but now taking into account the specific area A we are integrating over

$$N_1 = \frac{1}{\sqrt{\iint_A dxdy \left(\prod_{s=1}^{n} \varphi_s(x,y)\right)^2}} \tag{2.2.15}$$

These two expressions are easily generalized for any number of dimensions, having just to integrate over the hyper-volume element instead.

The energy functional matrix will be obtained in the same way,

$$E_{ij} = -\frac{1}{\pi^2} \iint_A dxdy \psi_i(x,y) \cdot \left(\nabla^2 \psi_j(x,y)\right) \tag{2.2.16}$$

To generate the higher order ψs, we need to generalize Equation 2.2.3. As we did in the 1D case, we again apply Gram-Schmidt orthogonalization

$$\tilde{\psi}_m(x,y) = f_m(x,y)\psi_1(x,y) - \sum_{i=2}^{m-1} \langle f_m(x,y)\psi_1(x,y) | \psi_i(x,y)\rangle \psi_i(x,y) \tag{2.2.17}$$

where the scalar product is the same as the one used before, but now in 2 dimensions:

$$\langle \phi_i(x,y) | \phi_j(x,y)\rangle = \iint_A dxdy \phi_i(x,y) \cdot \phi_j(x,y) \tag{2.2.18}$$

The problem, now, is writing $f_m(x,y)$. The method utilized by Liew and Lam [28] sorts the multiplying monomials f_m according to the pattern

$$\left\{1, x, y, xy, x^2, y^2, x^2y, xy^2, x^2y^2, x^3, y^3, x^3y, xy^3, x^3y^2, x^2y^3, x^3y^3, x^4, y^4, x^4y, xy^4, (...)\right\} \tag{2.2.19}$$

With this, we can define every $\psi_m = N_m \tilde{\psi}_m$ and use it to calculate the energy spectrum for the respective enclosure. The article mentioned above also includes a weighting function $\epsilon(x,y)$ that they associate with the thickness of the plates, but they take it as being 1 as they study uniformly thick plates. As it does not make much sense to talk about the "thickness" of a bi-dimensional shape, we omit it (i.e., we just replace it with 1).

As Gram-Schmidt orthogonalization is highly inefficient, and scales with the basis size as $\mathcal{O}(n^3)$, we would like to find a faster method. To do so, we utilize the "Orthogonalize[ ]"

built-in method in *Wolfram Mathematica*® with a list

$$\{\psi_1(x,y) * f_1(x,y), ..., \psi_1(x,y) * f_n(x,y)\}$$

where n is the size of the basis we want to create (we still need to normalize each element, but the normalization run-time is negligible in comparison), and the intended inner product function (in this case just the usual definition). This method is significantly faster than the previous one, giving a $\sim 600\%$ performance improvement for a basis with 10 functions. The main problem with this approach is the drastically increase in memory usage ($\sim 1000\%$ more for the same number of polynomials) which makes it completely unfeasible to expand the basis size. As such, we will mainly use it for smaller basis sizes.

There are several significative optimizations that we can insert into this process. Despite Gram-Schmidt orthogonalization being an inherently single-threaded procedure, we can accelerate it significantly by computing the sum

$$\sum_{i=2}^{m-1} \langle f_m(x,y)\, \psi_1(x,y) \,|\psi_i(x,y)\rangle \psi_i(x,y)$$

in parallel. We can also greatly optimize the process of integration of the Hamiltonian matrix. As we know this matrix to be Hermitian, we only need to integrate half of the matrix (and the diagonal) and add its transpose. This cuts the elements that we need to calculate from n^2 to $\frac{n(n+1)}{2}$, which is a very significant improvement. Still, the computation time of the Hamiltonian grows as $\mathcal{O}\left(n^2\right)$ with the basis size n. By parallelizing the sum in Equation 2.2.17, the computation time falls to about $\mathcal{O}\left(n^{1.5}\right)$.

2.3. Square Plane Enclosure

2.3.1. Cartesian Coordinates

For this shape of enclosure, the solutions are trivial. As one can immediately apply separation of variables, we just have

$$\psi(x,y) = \sin(k_x x)\sin(k_y y) \tag{2.3.1}$$

where the bottom-left corner of the square has been defined as the origin. In the top-right vertex (making the side of the square a), we have

$$\psi(a,a) = \sin(k_x a)\sin(k_y a) = 0 \tag{2.3.2}$$

If this condition is verified, the boundary condition in the edges $x = a$ or $y = a$ are immediately satisfied. By the choice of the function basis, the edges with $x = 0$ or $y = 0$ already obey to the desired boundary condition. Solving for k_x and k_y, this equation immediately gives a quantization of $k_{x,y}$

$$k_{x,y} = n_{x,y}\frac{\pi}{a} \tag{2.3.3}$$

which, by direct application, gives the energy levels

$$E_{n_x,n_y} = \frac{\pi^2}{a^2}\left(n_x^2 + n_y^2\right) \tag{2.3.4}$$

Which reduces to the well-known spectrum of the infinite square well

$$E = \frac{\pi^2}{a^2}\{2,5,5,8,10,10,13,13,17,17,18,20,20,25,25,32,(...)\} \tag{2.3.5}$$

We will now compare this spectrum to the one we will obtain from the Orthogonal Plate Functions formalism.

2.3.2. Orthogonal Plate Functions

We now want to apply the method described in Section 2.2 to this same enclosure. For simplicity in writing the polynomials, we redefine the origin as the center of the square. The lowest order polynomial that satisfies boundary conditions is given by

$$\psi_1(x,y) = N_1\left(L^2 - y^2\right)\left(L^2 - x^2\right) \tag{2.3.6}$$

Integrating Schrödinger's equation as was described previously,

$$E_{ij} = -\frac{1}{\pi^2}\iint_A dxdy\psi_i(x,y)\cdot\left(\nabla^2\psi_j(x,y)\right) \tag{2.3.7}$$

we get the ground-state's energy

$$E = 2.026424 \tag{2.3.8}$$

The 3D plot of $-\psi_1(x,y)$ is visible in Figure 2.3.1, and has the shape that one would expect given the symmetries of the enclosure in question. In Section A.1, we have the plots of $\psi_i(x,y)$

with $i \in [1, 8]$.

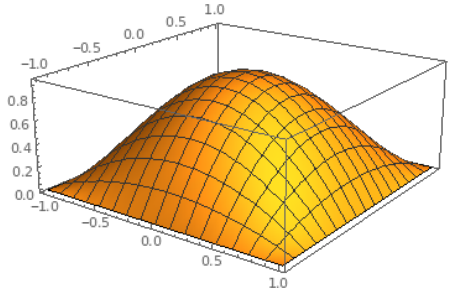

Figure 2.3.1.: Plot of $-\psi_1(x, y)$ for the square enclosure.

To better analyze the convergence of this method, we want to plot the energies for different numbers of polynomials.

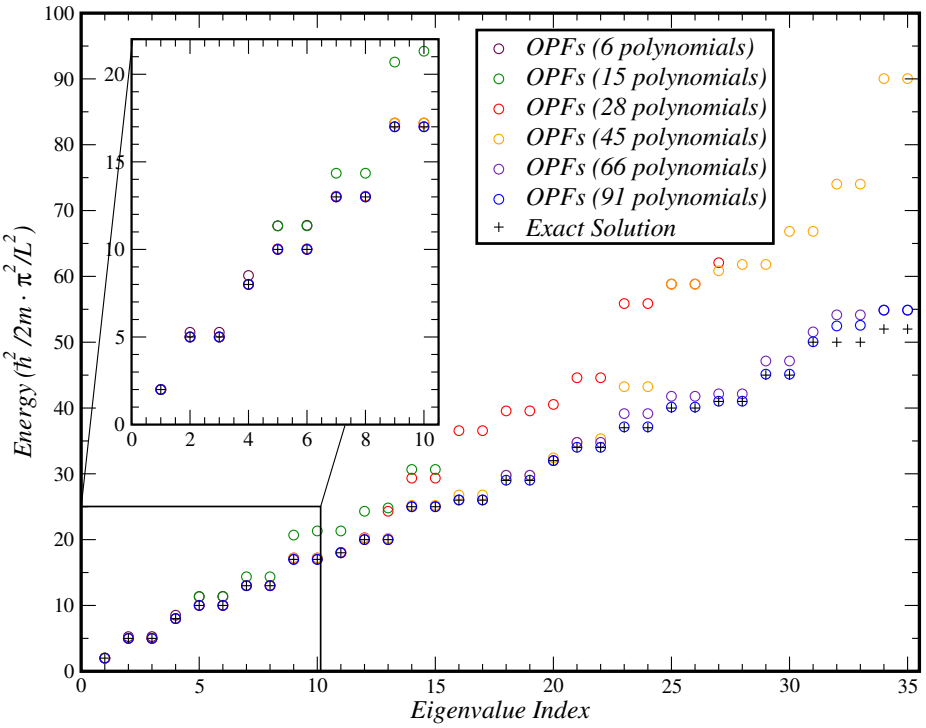

Figure 2.3.2.: Convergence of orthogonal plate functions method for different number of polynomials against the exact solution.

As can be seen in Figure 2.3.2, the lowest energies obtained from the orthogonal plate function method match almost perfectly with the exact solution starting at a very small basis size, possibly due to the enclosure's symmetries. It makes sense to try and generate the f_m functions taking into account the symmetries of the enclosure in question. If we do this, the Hamiltonian will be diagonalized by blocks of each irreducible representation of the symmetry group of the enclosure (discussed in Appendix A.2).

2.3.3. Orthogonal Plate Functions with C_{4v} Group Symmetries

Seeing as we are dealing with a square enclosure, it makes sense to treat it using the symmetries of the C_{4v} group [35]. This group has 8 elements, and its character table is visible in Figure 2.3.3.

C_{4v} (4mm)	E	$2C_4$	C_2	$2\sigma_v$	$2\sigma_d$		
A_1	1	1	1	1	1	z	x^2+y^2, z^2
A_2	1	1	1	−1	−1	R_z	
B_1	1	−1	1	1	−1		x^2-y^2
B_2	1	−1	1	−1	1		xy
E	2	0	−2	0	0	$(x, y)(R_x, R_y)$	(xz, yz)

Figure 2.3.3.: Character table of C_{4v}.

Here, C_4 denotes rotations of $\pm\frac{\pi}{2}$, $C_2 = C_4^2$, σ_v are the reflections on the two axis, and σ_d are the reflections on the diagonal symmetry axis of the square. Defining the invariant polynomial (the lowest order one that is zero on all boundaries) as

$$\tilde{\phi}_0(x,y) = \left(1-x^2\right)\left(1-y^2\right) \tag{2.3.9}$$

where the tilde ($\tilde{}$) identifies an un-normalized function. The higher order polynomials will be obtained by multiplication with a set of polynomials $f_{n,i}(x,y)$ that form irreducible representations of C_{4v}. Since ϕ_0 belongs to A_1 (is invariant under any symmetry operation), $f_m\phi_0$ belongs to the same irreducible representation as f_m. Here, the n denotes the order of this polynomial, and the i is merely an identifier inside each order of polynomials. Trivially, for $n = 0$ the only possible f is

$$f_0 = 1 \tag{2.3.10}$$

which belongs to A_1.

For $n = 1$, there are only 2 possible first-degree polynomials. As we want them to be orthogonal, we write

$$\begin{aligned} f_{1,1} &= x \\ f_{1,2} &= y \end{aligned} \tag{2.3.11}$$

which are elements of the irreducible representation E. With this knowledge, we can build the higher order polynomials recursively by taking products of this representation E with the existing lower order representations. From this point on, we will require the direct product table for this symmetry group, reproduced in Table 2.3.4.

	A_1	A_2	B_1	B_2	E
A_1	A_1	A_2	B_1	B_2	E
A_2		A_1	B_2	B_1	E
B_1			A_1	A_2	E
B_2				A_1	E
E					$A_1 + [A_2] + B_1 + B_2$

Figure 2.3.4.: Direct product table for C_{4v}.

For $n = 2$, we want to calculate $E \otimes E$. Applying the basic properties of decomposition, we

get

$$E \otimes E = A_1 \oplus A_2 \oplus B_1 \oplus B_2 \tag{2.3.12}$$

This presents us with a problem: there are only three 2nd order independent polynomials, but we have four irreducible representations. It becomes clear which is the one we can ignore when we write the three polynomials (obtained with regular multiplication of $f_{1,1}$ and $f_{1,2}$)

$$\begin{aligned} f'_{2,1} &= x^2 \\ f'_{2,2} &= y^2 \\ f'_{2,3} &= xy \end{aligned} \tag{2.3.13}$$

rearranging these, we get

$$\begin{aligned} f_{2,1} &= x^2 + y^2 \\ f_{2,2} &= x^2 - y^2 \\ f_{2,3} &= xy \end{aligned} \tag{2.3.14}$$

which are all orthogonal amongst themselves. We can clearly see that $f_{2,1} = x^2 + y^2$ is just the distance element, and is therefore obviously invariant under the action of any of the elements of the group. As such, it belongs to A_1. As $f_{2,2}$ is invariant under $x \to -x$ and $y \to -y$ transformations (i.e., the action of the two σ_v transformations) and changes signs under $(x, y) \to (\pm y, \pm x)$ (i.e., the action of the two σ_d transformations), it must belong to B_1. As for $f_{2,3}$, its properties of invariance are the inverse of those of $f_{2,2}$. Therefore, it must belong to B_2. Why are there no elements in A_2? For the simple reason that one cannot make a 2nd degree polynomial that is not invariant under both σ_v and σ_d, i.e., an anti-symmetric 2nd order polynomial.

For $n = 3$, we again must apply E to each one of these representations. Again with the assistance of the product table, we have that

$$\begin{aligned} E \otimes A_1 &= E \\ E \otimes B_1 &= E \\ E \otimes B_2 &= E \end{aligned} \tag{2.3.15}$$

Also, we will only have four 3rd order polynomials. The ones coming from the first product are quite simple, as A_1 is the invariant of the group:

$$\begin{aligned} f_{3,1} &= x\left(x^2 + y^2\right) \\ f_{3,2} &= y\left(x^2 + y^2\right) \end{aligned} \tag{2.3.16}$$

Of the two remaining polynomials, one should come from each one of the remaining irreducible representations:

$$\begin{aligned} f_{3,3} &= (x + y)\left(x^2 - y^2\right) \\ f_{3,4} &= (x + y)(xy) \end{aligned} \tag{2.3.17}$$

To see in which irreducible representation these fit, we can just apply the same procedure as before. With that, we see that they are not invariant or anti-symmetric under either σ_v or σ_d. As such, they can only belong to E, as expected.

Now finally onto $n = 4$. We are, again, applying E to itself, so we will have again Equation 2.3.12. As we are in 4^{th} order, we will have five independent polynomials. Without any further thought, we already know one of them:

$$f_{4,1} = \left(x^2 + y^2\right)^2 \tag{2.3.18}$$

which obviously belongs to A_1. Building the other fs from $n = 2$, we get

$$\begin{aligned} f_{4,2} &= \left(x^4 - y^4\right) \\ f_{4,3} &= xy\left(x^2 + y^2\right) \\ f_{4,4} &= \left(x^2 - y^2\right)^2 \\ f_{4,5} &= xy\left(x^2 - y^2\right) \\ f_{4,6} &= x^2y^2 \end{aligned} \tag{2.3.19}$$

Unfortunately, we have one polynomial too many. Looking at the product table and at the initial irreducible representations that were used to obtain these functions, we know that both $f_{4,2}$ and $f_{4,6}$ belong in A_1, along with $f_{4,1}$. We can clearly see that these three functions are not independent:

$$4 \cdot f_{4,6} = f_{4,1} - f_{4,4} \tag{2.3.20}$$

As such, the five functions will be $f_{4,1}$ to $f_{4,5}$, and their irreducible representations are

$$\begin{aligned} f_{4,1} &\to A_1 \\ f_{4,2} &\to B_1 \\ f_{4,3} &\to B_2 \\ f_{4,4} &\to A_1 \\ f_{4,5} &\to A_2 \end{aligned} \tag{2.3.21}$$

We can repeat this process up to any order, and the functions will be (by construction) orthogonal. Up to this order, the polynomials are grouped as

$$\begin{aligned} f_0, f_{2,1}, f_{4,1}, f_{4,4} &\to A_1 \\ f_{4,5} &\to A_2 \\ f_{2,2}, f_{4,2} &\to B_1 \\ f_{2,3}, f_{4,3} &\to B_2 \\ f_{1,1}, f_{1,2}, f_{3,1}f_{3,2}, f_{3,3}, f_{3,4} &\to E \end{aligned} \tag{2.3.22}$$

The polynomials will need to be orthogonalized amongst the same irreducible representation between different orders, and then normalized. After that, we multiply each one by ϕ_0 to then insert into the energy functional and obtain the spectrum. By definition of the irreducible representation, the Hamiltonian matrix will be diagonal by blocks of each representation.

Applying this method, we obtain the energies

$$\begin{aligned} E_{A_1} &= \{2.0000, 10.038, 20.691, 36.575\} \\ E_{A_2} &= \{24.317\} \\ E_{B_1} &= \{10.037, 36.571\} \\ E_{B_2} &= \{8.0123, 24.816\} \\ E_E &= \{5.0029, 5.0029, 14.603, 14.603, 21.328, 21.328\} \end{aligned} \tag{2.3.23}$$

where the index denotes the irreducible representation of the generating polynomials. It is quite noteworthy that some of the degenerate levels come from different irreducible representations. It makes sense that some energy levels' degeneracy is separated between two different representations. Let us consider, for example, the 2-times degenerate level $E = 10$: one of the solutions is equivalent the expression (we are performing the expansion up to 6^{th} order)

$$\cos(3\pi x)\cos(\pi y) + \cos(\pi x)\cos(3\pi y)$$

where the other one comes from

$$\cos(3\pi x)\cos(\pi y) - \cos(\pi x)\cos(3\pi y)$$

Clearly, the first expression has the symmetries of the representation A_1, where the second one has the ones from B_1. In the case of the energy level $E = 5$, we have a different situation: the two original functions are

$$\sin(2\pi x)\cos(\pi y) + \cos(\pi x)\sin(2\pi y)$$
$$\sin(2\pi x)\cos(\pi y) - \cos(\pi x)\sin(2\pi y)$$

which belong to the irreducible representation E.

This separation in irreducible representations has a few great advantages:

1. The solutions display more clearly the intrinsic symmetries of the problem at hand;

2. The computational time falls drastically: instead of diagonalizing a 15×15 matrix, we are diagonalizing at most a 6×6 one; also, we are skipping most of the Gram-Schmidt Orthogonalization, which grows as $\mathcal{O}\left(n^3\right)$;

3. The degeneracy lifting due to an additional potential is more clearly seen, as most of the degenerate levels are split between two irreducible representations.

Graphically, the spectrum translates to Figure 2.3.5.

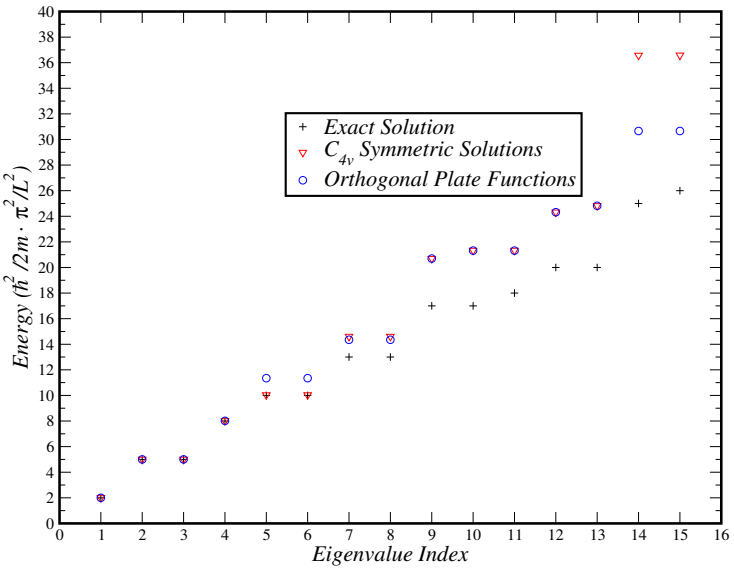

Figure 2.3.5.: Energy levels of a square infinite potential well compared between the exact solution, the C_{4v} block diagonalization and the "brute-force" approach.

Separating this spectrum by irreducible representations (due to the large difference in number of polynomials in each representation), we obtain Figure 2.3.6.

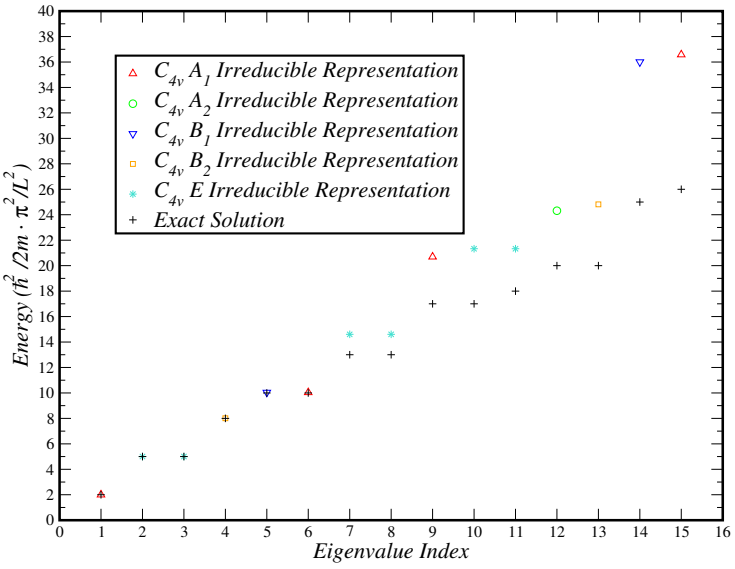

Figure 2.3.6.: Energy levels C_{4v} block diagonalization separated by irreducible representation.

We will now try to solve the hexagonal well problem, first with the "brute-force" method, and then using the C_{6v} symmetries.

2.4. Hexagonal Plane Enclosure

2.4.1. Orthogonal Plate Functions - Cartesian Coordinates

As we did in the case of the square enclosure, we again apply the method described in Section 2.2. The first wavefunction is

$$\psi_1(x,y) = N_1\left(\frac{3L^2}{4} - y^2\right)\left[L^2 - \left(x - \frac{y}{\sqrt{3}}\right)^2\right]\left[L^2 - \left(x + \frac{y}{\sqrt{3}}\right)^2\right] \tag{2.4.1}$$

For simplicity, the side of the hexagon will be defined as 1 (we later multiply by it's area to get the expected results, $A = \frac{3\sqrt{3}}{2}L^2$ where L is the side of the hexagon). N_1 is calculated as in the case of the square enclosure. The integrals over the area are performed to include only the inside of the enclosure:

$$\iint_A dxdy \to \int_{-\frac{\sqrt{3}}{2}L}^{\frac{\sqrt{3}}{2}L} dy \int_{-L+\frac{|y|}{\sqrt{3}}}^{L-\frac{|y|}{\sqrt{3}}} dx \tag{2.4.2}$$

Integrating Schrödinger's equation as was described previously, we get the ground-state's energy

$$E = 1.132806 \tag{2.4.3}$$

The 3D plot of $-\psi_1(x,y)$ is visible in Figure 2.4.1.

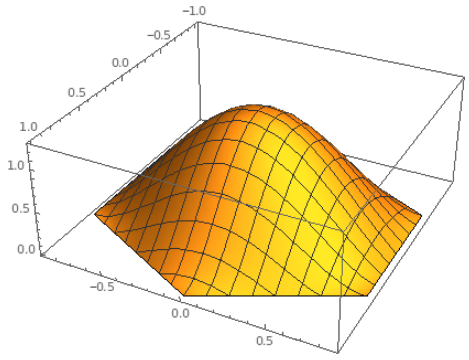

Figure 2.4.1.: Plot of $-\psi_1(x,y)$ for the hexagonal enclosure.

In Appendix A.3 we have the plot of $\psi_i(x,y)$ with $i \in [1,8]$.

Doing this calculation now with increasing order of multiplying-monomials, we obtain the energy spectrum (considering different numbers of polynomials to perform the same comparison that was done for the convergence in the scenario of the square well).

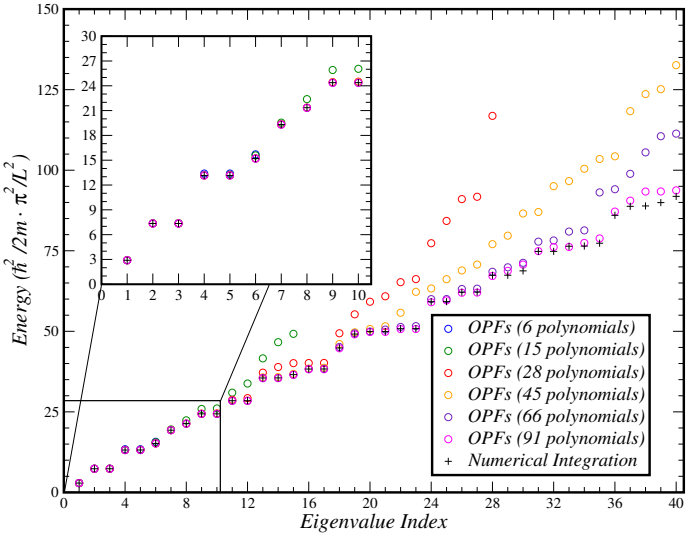

Figure 2.4.2.: Comparison of the energy levels of an hexagonal infinite potential well for different basis sizes with the solution from numerical integration.

As was visible in the case of the square enclosure, the lowest energy levels converge extremely quickly, even for very small basis size. This can be clearly seen in Figure 2.4.2, where the first 3 energy levels have converged to the numerical integration solution for a basis size of 6.

2.4.2. Orthogonal Plate Functions - Hexagonal Coordinates

Cartesian coordinates are not the most natural choice to describe an hexagonal enclosure. As such, we choose the two basis vectors

$$\mathbf{a}_1 = a\left(\frac{1}{2}, \frac{\sqrt{3}}{2}\right) \qquad \mathbf{a}_2 = a\left(-\frac{1}{2}, \frac{\sqrt{3}}{2}\right) \tag{2.4.4}$$

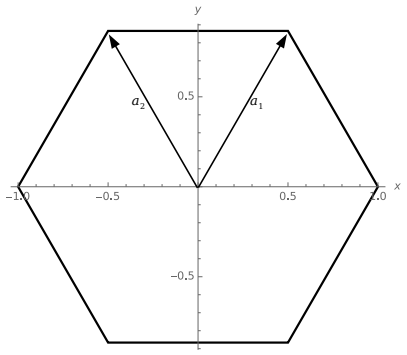

Figure 2.4.3.: New basis vectors.

We can describe any point as

$$\mathbf{r} = x^1\mathbf{a}_1 + x^2\mathbf{a}_2 = x^\mu\mathbf{a}_\mu \tag{2.4.5}$$

which means that both the inner domain and the boundary are easy to describe.

It is obvious that these coordinates are not orthogonal, but that is easily solvable. Taking the inner product, we get

$$\begin{aligned}\mathbf{r}\cdot\mathbf{r} &= a^2\left(x^1x^1 + x^2x^2 + 2x^1x^2\cos\left(\frac{\pi}{3}\right)\right)\\ &= g_{\mu\nu}x^\mu x^\nu\end{aligned} \tag{2.4.6}$$

which means that the metric is

$$\mathbf{g} = a^2\begin{bmatrix} 1 & 1/2 \\ 1/2 & 1 \end{bmatrix} \tag{2.4.7}$$

with inverse

$$\mathbf{g}^{-1} = a^{-2}\begin{bmatrix} 4/3 & -2/3 \\ -2/3 & 4/3 \end{bmatrix} \tag{2.4.8}$$

This means that the Laplacian is, by definition,

$$\nabla^2 = g^{\mu\nu}\partial_\mu\partial_\nu = \frac{4}{3a^2}\left(\partial_1^2 + \partial_2^2 - \partial_1\partial_2\right) \tag{2.4.9}$$

and the area element is

$$d^2\sigma = \sqrt{\det(\mathbf{g})}dx^1dx^2 = a^2\frac{\sqrt{3}}{2}dx^1dx^2 \tag{2.4.10}$$

Now let us look at the boundary. The six vertex coordinates are given by (starting at the $\mathbf{a}_1$ vertex and going around counter-clockwise)

$$\left(x^1, x^2\right) = \{(1,0),(0,1),(-1,1),(-1,0),(0,-1),(1,-1)\} \tag{2.4.11}$$

For simplicity, we will now go back to using the notation

$$\left(x^1, x^2\right) \to (x, y) \tag{2.4.12}$$

but we must remember that we are not working in Cartesian coordinates. The edge between $(1,-1)$ and $(1,0)$ is given by the equation

$$(x(\lambda), y(\lambda)) = (1,-1) + \lambda(0,1) \tag{2.4.13}$$

which reduces to

$$\begin{aligned} x &= 1\\ y &= \lambda - 1 \quad ,\lambda \in [0,1]\end{aligned} \tag{2.4.14}$$

Repeating this process for the other five edges, we get the equations for the six boundaries

$$x = \pm 1, \qquad y = \pm 1, \qquad x + y = \pm 1$$

as such, the inner region is defined by the conjugation of the three conditions

$$|x| < 1, \qquad |y| < 1, \qquad |x + y| < 1$$

Constructing the first polynomial that vanishes at the boundary in the same way as was done in the case of Cartesian coordinates, we get

$$\psi_1(x, y) = N_1 \left(L^2 - x^2\right) \left(L^2 - y^2\right) \left(L^2 - (x + y)^2\right) \tag{2.4.15}$$

The method for generating the higher order polynomials will be in the same way as before. The integrals over the region will now take the form

$$\int_{\sum} d^2\sigma \to a^2 \frac{\sqrt{3}}{2} \int_{-L}^{L} dx \int_{\max(-L,-L-x)}^{\min(L,L-x)} dy \tag{2.4.16}$$

As this region is invariant under a $\frac{\pi}{3}$ rotation, so should be the polynomials. In this coordinates, a $\pi/3$ rotation is

$$\mathbf{a}_1 \to \mathbf{a}_2 \qquad \mathbf{a}_2 \to \mathbf{a}_2 - \mathbf{a}_1$$

which means that, for a general $\mathbf{r}$

$$\mathbf{r} = x\mathbf{a}_1 + y\mathbf{a}_2 \to x\mathbf{a}_2 + y\left(\mathbf{a}_2 - \mathbf{a}_1\right) \tag{2.4.17}$$

With this, the rotation matrix is

$$\begin{bmatrix} x' \\ y' \end{bmatrix} = \begin{bmatrix} 0 & -1 \\ 1 & 1 \end{bmatrix} \begin{bmatrix} x \\ y \end{bmatrix} \tag{2.4.18}$$

and its inverse is

$$\begin{bmatrix} x \\ y \end{bmatrix} = \begin{bmatrix} 1 & 1 \\ -1 & 0 \end{bmatrix} \begin{bmatrix} x' \\ y' \end{bmatrix} \tag{2.4.19}$$

As such, the transformation of any function of x, y is

$$f(\mathbf{r}) \to g(\mathbf{r}) = f\left(\mathbf{R}^{-1} \cdot \mathbf{r}\right) = f(x + y, -x) \tag{2.4.20}$$

Applying this to our first polynomial, we get that $\psi_1(x, y)$ is invariant under a $\pi/3$ rotation, as expected:

$$\psi_1'(x, y) = \left(1 - (x + y)^2\right) \left(1 - (-x)^2\right) \left(1 - (x + y - x)^2\right) = \psi_1(x, y) \tag{2.4.21}$$

Either one of these choices of coordinates must (and will) give out the same values. Hexagonal coordinates are more natural, while Cartesian coordinates should be faster computationally. For comparison, we look at the energy levels for 9 polynomials in these two coordinates, as

well as the "exact" solution obtained by calculating the eigenvalues of the Laplacian operator in *Wolfram Mathematica*®

$$\begin{aligned} E_{\text{cartesian}} &= \{2.9084, 7.3717, 7.3718, 13.343, 13.389, 15.606, 20.888, 23.364, 32.450\} \\ E_{\text{hexagonal}} &= \{2.9082, 7.3706, 7.3727, 13.379, 13.389, 15.587, 22.593, 22.866, 33.623\} \\ E_{\text{PDE}} &= \{2.9001, 7.3493, 7.3493, 13.155, 13.156, 15.199, 19.314, 21.344, 24.376\} \end{aligned} \tag{2.4.22}$$

Finally, we compare the computational time for each other (separated between polynomial generation and integration of the energy functional)

$$\Delta T_{\text{cartesian}} \sim 1502.54 + 12243 \ \ (s) \qquad \Delta T_{\text{hexagonal}} \sim 1273.5 + 17418 \ \ (s) \tag{2.4.23}$$

It makes sense that the integration is faster in Cartesian coordinates, as in hexagonal coordinates we also need to calculate crossed derivatives in the Laplacian. It is important to note that these times were obtained without any optimizations from parallelization. The main issue that comes from using hexagonal coordinates is the drastically increased memory usage ($\sim$ 5000% more) during the calculations, primarily due to the extra term in the Laplacian (this extra term adds up for each order during the Gram-Schmidt orthogonalization, which very quickly increases the necessary memory). When we add the optimizations that come from the symmetry group to the generation of polynomials and the orthogonalization, the computational time will surely fall drastically. Visually, these eigenvalues translate to Figure 2.4.4.

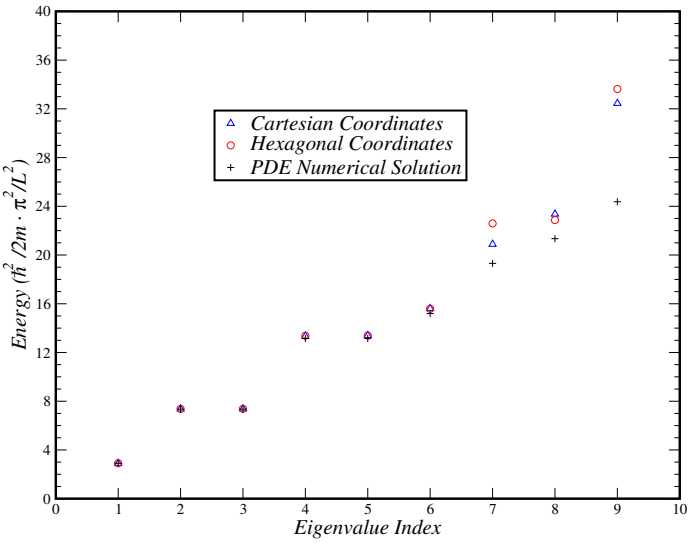

Figure 2.4.4.: Comparison of the energy levels for the hexagonal well obtained through both hexagonal and Cartesian coordinates, and from numerical integration of Schrödinger's equation.

2.4.3. Orthogonal Plate Functions with C_{6v} Group Symmetries

We will now repeat the group theory treatment to this problem, but now using the C_{6v} group [35]. This group has 12 elements, and its character table is reproduced in Table 2.4.5.

C_{6v} (6mm)	E	$2C_6$	$2C_3$	C_2	$3\sigma_v$	$3\sigma_d$		
A_1	1	1	1	1	1	1	z	x^2+y^2, z^2
A_2	1	1	1	1	−1	−1	R_z	
B_1	1	−1	1	−1	1	−1		
B_2	1	−1	1	−1	−1	1		
E_1	2	1	−1	−2	0	0	$(x, y)(R_x, R_y)$	(xz, yz)
E_2	2	−1	−1	2	0	0		$(x^2-y^2, 2xy)$

Figure 2.4.5.: Character table of C_{6v}.

Here, C_6 denotes rotations of $\pm\frac{\pi}{3}$, $C_3 = C_6^2$, $C_2 = C_6^4$; σ_v are the reflections on the three axis that pass through the vertices, and σ_d are the reflections on the three axis that pass through the faces. Defining the invariant polynomial (the lowest order one that is zero on all boundaries) as

$$\tilde{\phi}_0(x,y) = \left(\frac{3}{4} - y^2\right)\left(1 - \left(x - \frac{y}{\sqrt{3}}\right)^2\right)\left(1 - \left(x + \frac{y}{\sqrt{3}}\right)^2\right) \tag{2.4.24}$$

where the tilde ($\tilde{}$) identifies an un-normalized function. As previously, the higher order polynomials will be obtained by multiplication with a set of polynomials $f_{n,i}(x,y)$ that form irreducible representations of C_{6v}. As the treatment is entirely analogous to the one performed for the case of the square enclosure, we have moved it to Appendix A.4.

Up to sixth order, the polynomials are grouped as

$$\begin{aligned} f_0, f_{2,1}, f_{4,1}, f_{6,1} &\to A_1 \\ f_{3,3}, f_{5,3} &\to B_1 \\ f_{3,4}, f_{5,4} &\to B_2 \\ f_{1,1}, f_{1,2}, f_{3,1}, f_{3,2}, f_{5,1}, f_{5,2}, f_{5,5}, f_{5,6} &\to E_1 \\ f_{2,2}, f_{2,3}, f_{4,2}, f_{4,3}, f_{4,4}, f_{4,5}, f_{6,2}, f_{6,3}, f_{6,4}, f_{6,5}, f_{6,6}, f_{6,7} &\to E_2 \end{aligned} \tag{2.4.25}$$

These polynomials will need to be orthogonalized amongst the same irreducible representation between different orders, and then normalized. After that, we multiply each one by ϕ_0 to then insert into the energy functional and obtain the spectrum. This method significantly speeds up the calculations, as we only integrate (at most) a 12×12 matrix instead of a 28×28 one (considering the same total number of polynomials).

Comparing against both the results from numerical integration of Schrödinger's equation, as well as the results for the "brute-force" Orthogonal Plate Functions (considering the same number of polynomials), we can see (Figure 2.4.6) that taking into account the symmetries of the enclosure allows the eigenvalues to remain closer to the solution obtained by partial differential equation numerical integration up until a higher eigenvalue index.

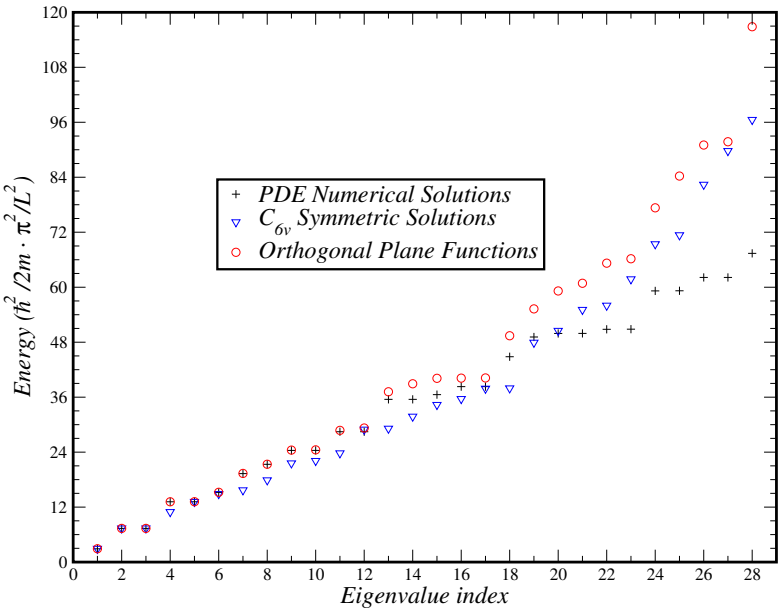

Figure 2.4.6.: Comparison of the energy levels for PDE numerical integration, C_{6v} symmetry analysis and "brute-force" orthogonal plate functions.

It makes sense why the C_{6v} spectrum is different from the standard OPF method, as the group symmetry approach goes in crescent order of multiplying polynomial, which is a different ordering procedure than the one used by Liew and Lam [28]. We plot the different irreducible representations separately in Figure 2.4.7 so that we can better understand the number of polynomials used in each point of the figure.

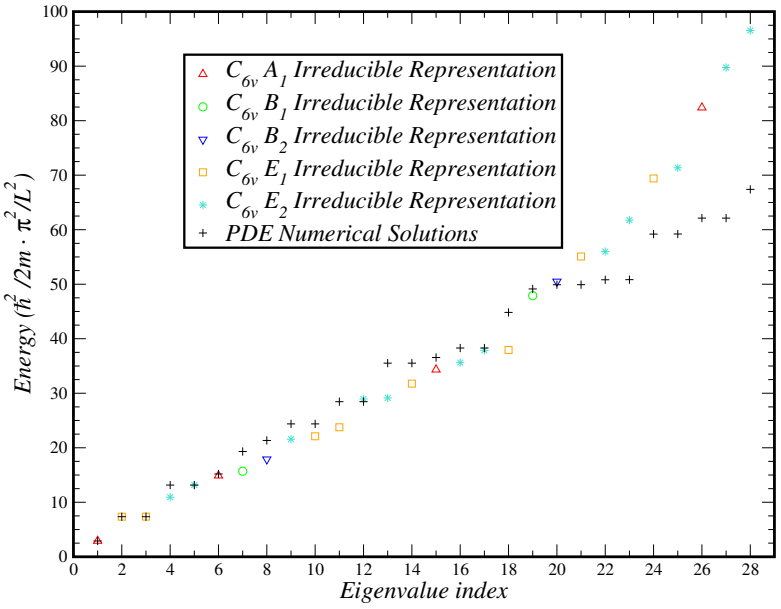

Figure 2.4.7.: Energy levels C_{6v} block diagonalization separated by irreducible representation.

2.5. Increasing the Number of Sides

As a final analysis of the Schrödinger problem, one interesting point is the comparison of the spectra of these enclosures while keeping the area constant. Starting by the triangle, where we have an analytical solution by both Li and Blinder [36], and Gaddah [27], we increase the number of sides to the square, then the hexagon and finally the circle, as it is equivalent to the limit of the number of sides going to infinity. The polynomial treatment for the triangle is analogous to the previous examples, so we will not include it.

As we define the integration region as a function of the length of a side, it is useful to write the area as a function of this same length. For a regular n-sided polygon, the area is given by

$$A_n = \frac{L^2}{4} \times \frac{n}{\tan\left(\frac{\pi}{n}\right)} \tag{2.5.1}$$

Fixing $A = 1$, we obtain (expanding in Taylor series for large n)

$$L^2 = 4 \times \frac{\tan\left(\frac{\pi}{n}\right)}{n} \approx 4\frac{\pi}{n^2} + \frac{4}{3}\frac{\pi^3}{n^4} + ... \tag{2.5.2}$$

We now have all that we need to analyze the evolution of the spectrum as we increase the number of sides while keeping the area constant. Considering a basis size of 91 for the three polygons (truncating at the 45^{th} eigenvalue so that we only compare values that have almost converged), we obtain Figure 2.5.1.

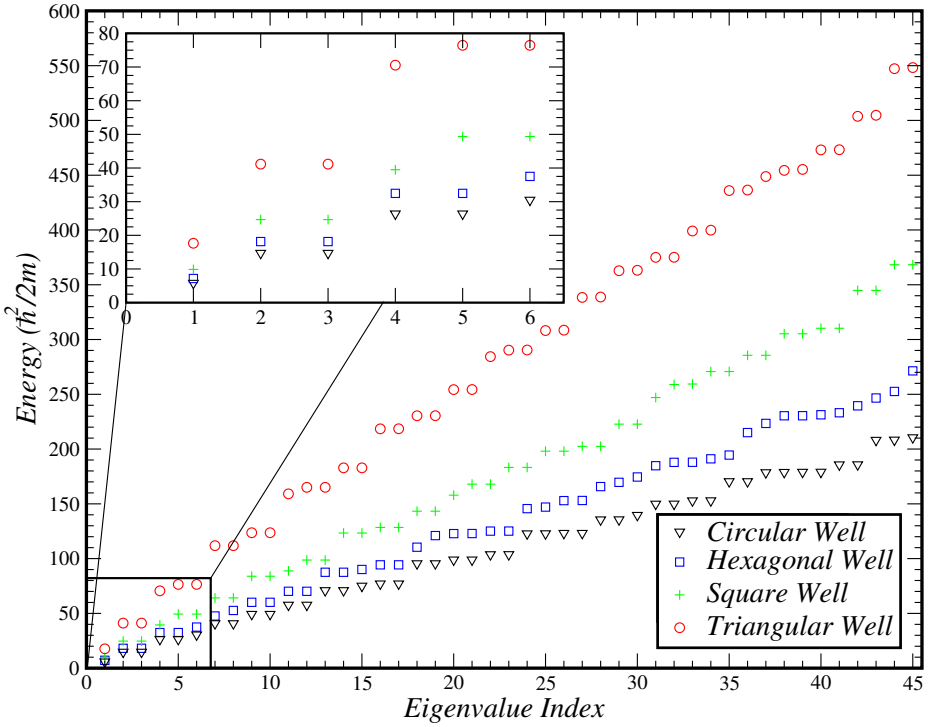

Figure 2.5.1.: Comparison of the energy levels for different numbers of sides (with constant area).

As we can see, the energy eigenvalue decrease with the number of sides of the polygon. This makes sense, as we are converging towards the result for the circle. Plotting the evolution of the first three different eigenvalues as a function of $\frac{1}{n}$, we obtain Figure 2.5.2.

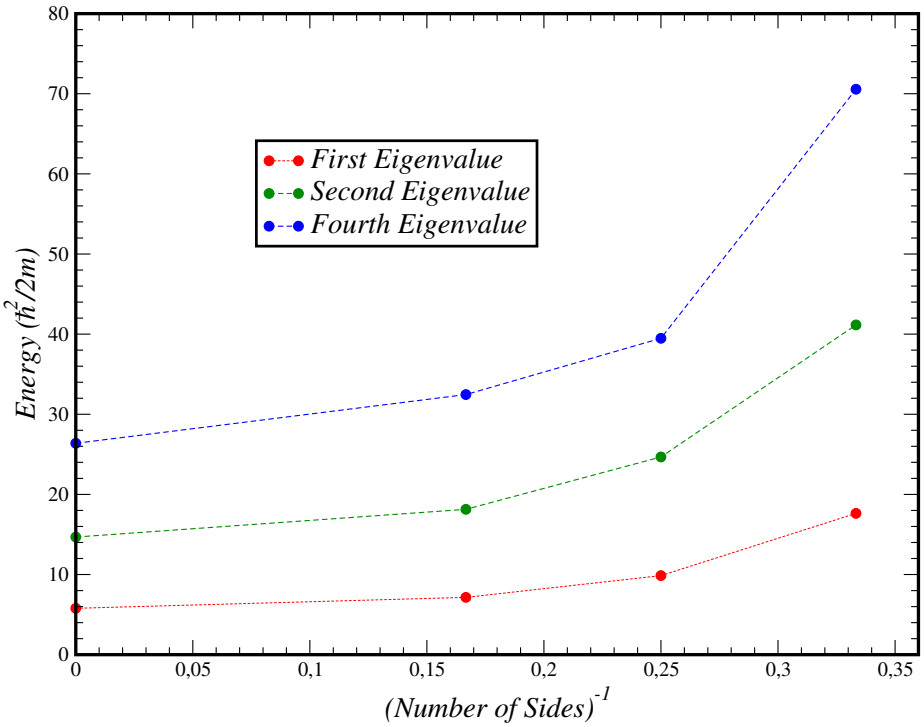

Figure 2.5.2.: Comparison of the first three different energy levels as a function of the inverse of the number of sides of the polygon.

2.6. Final Considerations

As we have seen in these previous chapters, this method works extremely well, and has reasonably fast convergence. We have been able to replicate the exact solution for both the case of the square well as well as the 1D well with great accuracy. After verifying the validity of this method with those well-known cases, we obtained the low-energy eigenvalues for the hexagonal well, which match closely with the ones obtained by numerical integration of the Laplacian operator. We have also verified the possibility of pre-diagonalizing the Hamiltonian matrix by taking into account the different irreducible representations of the point-group that represents the intrinsic symmetries of the spacial enclosure in question.

We analyzed the behaviour of the spectra as the number of sides was increased, obtaining the quick convergence towards the eigenvalues of the circular well problem (i.e., the zeros of the Bessel functions).

Having closed this part, the fundamental question now is "Can we apply the Orthogonal Plate Function method to a problem that has an intrinsic spinorial behaviour?"

3. Relativistic Regime: the Dirac-Weyl Equation

Having solved the classical problem, we now want to jump to electron in graphene, where they are governed by the Dirac-Weyl equation. As such, we must find a way to generalize this polynomial method to generalize this method for spinorial particles.

First, we will discuss boundary conditions, extending the orthogonal plate function method to Dirac billiards, and we will solve some illustrative examples of 1D billiards with different boundary conditions.

Next, we will review the treatment performed by Gaddah [30] of the triangular billiard by means of the C_{3v} symmetry, which we replicate using the Helmholtz equation and our polynomial method.

Finally, we will study the Dirac-Weyl equation in polar coordinates, where we will look at the necessary conditions for the existence of confined states in a circular enclosure and the spectrum of such an enclosure.

3.0.1. Dirac-Weyl Equation in Graphene – General Hamiltonian

In graphene, electrons behave as ultra-relativistic massless particles near the Dirac points $\mathcal{K}$ and $\mathcal{K}'$ [2]. The low-energy effective Hamiltonian near these points is given by

$$\mathcal{H} = \begin{pmatrix} \mathcal{H}_{\mathcal{K}} & 0 \\ 0 & \mathcal{H}_{\mathcal{K}'} \end{pmatrix} \tag{3.0.1}$$

where

$$\begin{aligned} \mathcal{H}_{\mathcal{K}} &= \hbar v_F \sigma \cdot \mathbf{p} \\ \mathcal{H}_{\mathcal{K}'} &= \hbar v_F \sigma^* \cdot \mathbf{p} \end{aligned} \tag{3.0.2}$$

and σ represents the Pauli matrices [37]

$$\sigma = (\sigma_x, \sigma_y) = \left(\begin{pmatrix} 0 & 1 \\ 1 & 0 \end{pmatrix}, \begin{pmatrix} 0 & -i \\ i & 0 \end{pmatrix} \right) \tag{3.0.3}$$

which means that the Hamiltonian can be written as

$$\mathcal{H} = -i\hbar v_F \begin{pmatrix} 0 & \prod_- & 0 & 0 \\ \prod_+ & 0 & 0 & 0 \\ 0 & 0 & 0 & \prod_+ \\ 0 & 0 & \prod_- & 0 \end{pmatrix} \tag{3.0.4}$$

where

$$\prod_{\pm} = \partial_x \pm i\partial_y \tag{3.0.5}$$

These operators act on the Dirac spinor

$$\Psi = \begin{bmatrix} \varphi_A \\ \varphi_B \\ \varphi_{A'} \\ \varphi_{B'} \end{bmatrix} \tag{3.0.6}$$

where the A, B indexes are referring to the sub-lattices, and the prime denotes the Dirac point ($\mathcal{K}$ or $\mathcal{K}'$).

In the following chapters we will perform the treatment of the equation always considering only the $\mathcal{K}$ valley.

3.1. Extension of Orthogonal Plate Functions to Dirac Billiards

To replicate the procedure used for the case of Schrödinger's equation, we now want to create a polynomial method of obtaining the eigenstates and the energy levels of polygonal enclosures using Dirac's equation. As such, we first start by obtaining the exact solution for the 1D billiards [38], which we use to check the validity of the polynomial results. After that, we generalize the boundary conditions by comparison with the work from Berry and Mondragan [39] and discuss important aspects of this polynomial method. Finally, we use it to obtain the spectrum of square billiards with uniform boundaries, as well as hexagonal billiards with zigzag-like boundaries.

3.1.1. One-Dimensional Billiards

3.1.1.1. Boundary at $y = 0$

We are considering the Dirac-Weyl equation

$$\hbar v_F \boldsymbol{\sigma} \cdot \left(\frac{\nabla}{i} \right) \Psi = E\Psi, \tag{3.1.1}$$

with a confining boundary at $y = 0$, and assuming the solution is confined to $y > 0$.

Figure 3.1.1.: Confining to $y > 0$ at a straight boundary.

The probability current operator is given by

$$\mathbf{j} = v_F \Psi^\dagger \boldsymbol{\sigma} \Psi = v_F \langle \boldsymbol{\sigma} \rangle. \tag{3.1.2}$$

For us to have confined states, we must require that no current cross the boundary, or

$$\langle \sigma^y \rangle_{\text{boundary}} = 0. \tag{3.1.3}$$

This means that the spinor at the boundary must be an eigenstate of some component $\sigma_u = \boldsymbol{\sigma} \cdot \mathbf{u}$, where $\mathbf{u} = \cos\theta \mathbf{e}_z + \sin\theta \mathbf{e}_x$

$$\begin{bmatrix} \cos\theta & \sin\theta \\ \sin\theta & -\cos\theta \end{bmatrix} \begin{bmatrix} \phi_A \\ \phi_B \end{bmatrix} = \eta \begin{bmatrix} \phi_A \\ \phi_B \end{bmatrix} \qquad \eta = \pm 1, \tag{3.1.4}$$

or

$$\begin{aligned} \cos\theta\phi_A + \sin\theta\phi_B &= \eta\phi_A \\ \frac{\phi_B}{\phi_A} &= \frac{\eta - \cos\theta}{\sin\theta}. \end{aligned} \tag{3.1.5}$$

Simple trigonometric identities lead to

$$\frac{\phi_B}{\phi_A} = \frac{2\sin^2(\theta/2)}{2\sin(\theta/2)\cos(\theta/2)} = \tan\left(\frac{\theta}{2}\right) \qquad \eta = 1, \tag{3.1.6}$$

or

$$\frac{\phi_B}{\phi_A} = -\frac{2\cos^2(\theta/2)}{2\sin(\theta/2)\cos(\theta/2)} = -\frac{1}{\tan\left(\frac{\theta}{2}\right)} \qquad \eta = -1. \tag{3.1.7}$$

Denoting $t = \tan(\theta/2)$,

$$\begin{bmatrix} \phi_A \\ \phi_B \end{bmatrix} = \frac{1}{\sqrt{1+t^2}} \begin{bmatrix} 1 \\ t \end{bmatrix} \qquad \eta = 1 \tag{3.1.8}$$

$$\begin{bmatrix} \phi_A \\ \phi_B \end{bmatrix} = \frac{1}{\sqrt{1+t^2}} \begin{bmatrix} -t \\ 1 \end{bmatrix} \qquad \eta = -1 \tag{3.1.9}$$

give the form of the spinor at the boundary, $y = 0$. The parameter t is real and can vary from $t \in [-\infty, +\infty]$. The second case is obtained by the replacement $t \to -1/t$ in the first, or by changing $\theta \to \pi - \theta$. So it is not a different solution and we can keep only

$$\begin{bmatrix} \phi_A \\ \phi_B \end{bmatrix} = \frac{1}{\sqrt{1+t^2}} \begin{bmatrix} 1 \\ t \end{bmatrix} \tag{3.1.10}$$

Specific boundary conditions (BCs) are:

- $t = 0$ or $t \to \infty$

$$\begin{cases} t = 0, & \phi_B = 0 \quad \langle\sigma^z\rangle = 1 \text{(zigzag-like)} \\ t \to \infty, & \phi_A = 0 \quad \langle\sigma^z\rangle = -1 \text{(zigzag-like)} \end{cases} \tag{3.1.11}$$

  In this case the spin is along z at the boundary.

- $t = \pm 1$

$$\phi_A = \pm\phi_B \tag{3.1.12}$$

  In this case the spin points along x.

Berry and Mondragan [39] show that latter case corresponds to infinite mass confinement. In other words, they claim that Equation 3.1.12 is obtained from

$$\left(\hbar v_F \boldsymbol{\sigma} \cdot \frac{\nabla}{i} + m(\mathbf{r})\sigma^z\right)\Psi = E\Psi \tag{3.1.13}$$

with $m = 0$ in the confined region and $m \to \pm\infty$ outside.

The boundary condition is basically a condition of continuity of the spinor at the boundary. When $m \to \infty$, the two spinor states $\sigma^z = \pm 1$ have energies $\pm\infty$. We may reason that, at the

boundary, a finite energy requires a mean $\langle\sigma^z\rangle = 0$; also $\langle\sigma^y\rangle = 0$ (no current). This requires the spinor to be an eigenstate of σ^x, the eigenvalues being ± 1.

These heuristic consideration notwithstanding, the essential point is that confinement of finite energy states requires a gap, which, for hard boundaries, should be infinite. We can therefore ask if we can obtain other types of BCs.

Suppose that the Hamiltonian also has a scalar potential with the same mass scale:

$$\hbar v_F \boldsymbol{\sigma} \cdot \left(\frac{\nabla}{i}\right) \Psi + m(\mathbf{r}) \left(\sigma^z - \cos\theta\right) \Psi = E\Psi \tag{3.1.14}$$

with $m(\mathbf{r}) = 0$ in the confining region and $m(\mathbf{r}) \to \infty$ outside. Choosing y coordinate normal to interface in the forbidden region, and trying $\Psi(x, y) = \exp(ik_x x)\Phi(y)$

$$\left(-i\hbar v_F \sigma^y \partial_y + \hbar v_F k_x \sigma^x\right) \Phi = \left[E - m\left(\sigma^z - \cos\theta\right)\right] \Phi. \tag{3.1.15}$$

In spinor components,

$$\partial_y \phi_B - k_x \phi_B = -\frac{\left[E - m\left(1 - \cos\theta\right)\right]}{\hbar v_F} \phi_A \tag{3.1.16}$$

$$\partial_y \phi_A + k_x \phi_A = \frac{\left[E + m\left(1 + \cos\theta\right)\right]}{\hbar v_F} \phi_B. \tag{3.1.17}$$

A confined state requires

$$\phi_B(y) = Be^{\kappa y} \tag{3.1.18}$$

$$\phi_A(y) = Ae^{\kappa y} \tag{3.1.19}$$

with $\kappa > 0$. Therefore,

$$\left(\kappa - k_x\right) B = -\frac{\left[E - m\left(1 - \cos\theta\right)\right]}{\hbar v_F} A \tag{3.1.20}$$

$$\left(\kappa + k_x\right) A = \frac{\left[E + m\left(1 + \cos\theta\right)\right]}{\hbar v_F} B. \tag{3.1.21}$$

As $m \to \infty$, we can drop E compared to m, and k_x compared to κ,

$$\left(\frac{B}{A}\right)^2 = \frac{m\left(1 - \cos\theta\right)}{m\left(1 + \cos\theta\right)} = \frac{\sin^2(\theta/2)}{\cos^2(\theta/2)} \tag{3.1.22}$$

The boundary condition becomes

$$\frac{B}{A} = \pm \tan\left(\frac{\theta}{2}\right) = \eta t \qquad \eta = \pm 1 \tag{3.1.23}$$

But

$$\kappa B = \frac{m\left(1 - \cos\theta\right)}{\hbar v_F} A \tag{3.1.24}$$

which means that η is the sign of m.

In summary, the boundary condition has the form

$$\phi_B = t\phi_A \tag{3.1.25}$$

where $t \in [-\infty, +\infty]$ and the ket at the boundary has the form of Equation 3.1.10. Note that Equation 3.1.26 fixes the normal current to the edge at zero.

$$\begin{aligned} \Psi^\dagger \sigma^x \Psi &= \frac{2t}{1+t^2} \\ \Psi^\dagger \sigma^y \Psi &= 0 \\ \Psi^\dagger \sigma^z \Psi &= \frac{1-t^2}{1+t^2} \end{aligned} \tag{3.1.26}$$

3.1.1.2. Gaddah and $t = 0$

For Gaddah's [30] situation ($t = 0$), we must be careful when applying Equation 3.1.21. Dropping (again) k_x when compared to κ, and E when compared to m, we have

$$\kappa \frac{A}{B} = \frac{m\,(1+\cos\theta)}{\hbar v_F}$$

Simplifying, this reduces to

$$\kappa = \frac{m\,(1+\cos\theta)}{\hbar v_F} t, \tag{3.1.27}$$

which means that, if we take the $t \to 0$ limit first, we obtain simply

$$\kappa = 0. \tag{3.1.28}$$

This means that the states are not confined, which is not acceptable. As such, the order of the limits is fundamental, and will separate physical from non-physical solutions.

3.1.1.3. General Boundary

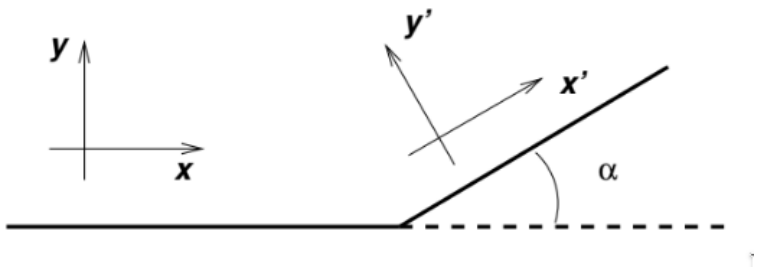

Figure 3.1.2.: Arbitrary boundary.

For a boundary with a more general orientation, we can still use as x', y' the coordinates along the boundary and orthogonal to it. Our spinor at the boundary should still have in these

coordinates

$$\Psi^\dagger \sigma^{x'} \Psi = \frac{2t}{1+t^2} \tag{3.1.29}$$

$$\Psi^\dagger \sigma^{y'} \Psi = 0 \tag{3.1.30}$$

$$\Psi^\dagger \sigma^{z} \Psi = \frac{1-t^2}{1+t^2} \tag{3.1.31}$$

meaning it should be rotated from the one in Equation 3.1.26,

$$\Psi = e^{-i\alpha\sigma_z/2} \frac{1}{\sqrt{1+t^2}} \begin{bmatrix} 1 \\ t \end{bmatrix} = \frac{1}{\sqrt{1+t^2}} \begin{bmatrix} e^{-i\alpha/2} \\ e^{i\alpha/2} t \end{bmatrix}$$

leading to a boundary condition

$$\frac{\phi_B}{\phi_A} = e^{i\alpha} t \tag{3.1.32}$$

For a boundary along $y = 0$ with y' pointing inwards we $\alpha = \pi/2$ so the boundary condition would be

$$\frac{\phi_B}{\phi_A} = it \tag{3.1.33}$$

Suppose we have a square. The boundary conditions would read

$$\frac{\phi_B}{\phi_A} = t \qquad \text{South} \tag{3.1.34}$$

$$\frac{\phi_B}{\phi_A} = it \qquad \text{East} \tag{3.1.35}$$

$$\frac{\phi_B}{\phi_A} = -t \qquad \text{North} \tag{3.1.36}$$

$$\frac{\phi_B}{\phi_A} = -it \qquad \text{West} \tag{3.1.37}$$

This naturally assumes the same confining environment around the square domain ($m(\mathbf{r}) = m, \theta$ fixed). One can always consider the more general case where t is different at different boundaries, where these equations would still hold.

3.1.2. One-Dimensional Examples

To illustrate the polynomial method, we consider two straight boundaries at $y = \pm L/2$ and write Dirac's equation for the spinor $\Psi(y)$ in the region inside ($m = 0$)

$$-i\hbar v_F \sigma_y \partial_y \Psi = E\Psi \tag{3.1.38}$$

or

$$-\hbar v_F \partial_y \psi_B = E\psi_A \tag{3.1.39}$$

$$\hbar v_F \partial_y \psi_A = E\psi_B \tag{3.1.40}$$

To simplify the dimensionality of this problem, we will work in units of $\hbar v_F$. This means that our equations now read

$$-\partial_y \psi_B = \epsilon \psi_A \tag{3.1.41}$$
$$\partial_y \psi_A = \epsilon \psi_B \tag{3.1.42}$$

Clearly

$$-\partial_y^2 \psi_{B(A)} = \epsilon^2 \psi_{B(A)} \tag{3.1.43}$$

and the solutions are

$$\psi_B = Ae^{iqy} + Be^{-iqy} \tag{3.1.44}$$
$$\psi_A = Ce^{iqy} + De^{-iqy} \tag{3.1.45}$$

Without loss of generality, we can take $q > 0$ and $\epsilon = sq$ with $s = \pm 1$. To determine the constants A to D, we require that this forms a solution of Dirac's equation and satisfies the boundary conditions

$$\frac{\psi_B}{\psi_A} = t \qquad y = -L/2 \tag{3.1.46}$$
$$\frac{\psi_B}{\psi_A} = -t \qquad y = L/2 \tag{3.1.47}$$

Dirac's equation implies

$$-iq\left(Ae^{iqy} - Be^{-iqy}\right) = sq\left(Ce^{iqy} + De^{-iqy}\right) \tag{3.1.48}$$

or

$$D = isB \qquad\qquad C = -isA \tag{3.1.49}$$

The boundary conditions are

$$e^{iqL/2}\left(A + Be^{-iqL}\right) = -te^{iqL/2}\left(C + De^{-iqL}\right) \tag{3.1.50}$$
$$e^{-iqL/2}\left(A + Be^{+iqL}\right) = te^{-iqL/2}\left(C + De^{+iqL}\right) \tag{3.1.51}$$

or

$$(A + tC) + (B + tD)\, e^{-iqL} = 0 \tag{3.1.52}$$
$$(A - tC) + (B - tD)\, e^{iqL} = 0. \tag{3.1.53}$$

Using Equations 3.1.49, this becomes a 2×2 homogeneous system for A and B.

$$(1 - ist)\, A + (1 + ist) Be^{-iqL} = 0 \tag{3.1.54}$$
$$(1 + ist)\, A + (1 - ist) Be^{iqL} = 0 \tag{3.1.55}$$

A non-zero solution requires

$$\det \begin{bmatrix} (1-ist) & (1+ist)e^{-iqL} \\ (1+ist) & (1-ist)e^{iqL} \end{bmatrix} = 0 \tag{3.1.56}$$

which means that

$$(1-ist)^2 e^{iqL} - (1+ist)^2 e^{-iqL} = 0 \tag{3.1.57}$$

or simply

$$\tan(qL) = \frac{2st}{(1-t^2)} \tag{3.1.58}$$

For the limit case of $t = 1$

$$\cos(qL) = 0 \Longrightarrow qL = (2n+1)\frac{\pi}{2} \tag{3.1.59}$$

When $t = 0$ ($\psi_B = 0$ in both edges)

$$\sin(qL) = 0 \Longrightarrow qL = n\pi \tag{3.1.60}$$

3.1.2.1. Solution for $t = 1$

The energies are

$$\epsilon_n = s(2n+1)\frac{\pi}{2L} = s\frac{\pi}{2L}, s\frac{3\pi}{2L}, s\frac{5\pi}{2L}, \ldots \tag{3.1.61}$$

and the solutions are

$$A = -\frac{(1+is)}{(1-is)} B e^{-iqL} \tag{3.1.62}$$

$$\frac{A}{B} = -e^{is\pi/2} e^{-i(2n+1)\pi/2} = (-1)^{n+1} i^{s-1} \tag{3.1.63}$$

For $s = 1$

$$\frac{A}{B} = (-1)^{n+1} \tag{3.1.64}$$

For $s = -1$

$$\frac{A}{B} = (-1)^{n} \tag{3.1.65}$$

If we consider the states of the conduction band ($s = 1$), we get

$$\phi_B^{(0)} = A \sin\left(\frac{\pi}{2L} y\right) \tag{3.1.66}$$

$$\phi_A^{(0)} = -\frac{1}{\epsilon}\partial_y \psi_B = -A \cos\left(\frac{\pi}{2L} y\right) \tag{3.1.67}$$

These functions obey the imposed boundary conditions, as one can see

$$\frac{\phi_B^{(0)}\left(-L/2\right)}{\phi_A^{(0)}\left(-L/2\right)} = \frac{-A\sin\left(\pi/4\right)}{-A\cos\left(\pi/4\right)} = 1 \tag{3.1.68}$$

$$\frac{\phi_B^{(0)}\left(L/2\right)}{\phi_A^{(0)}\left(L/2\right)} = \frac{A\sin\left(\pi/4\right)}{-A\cos\left(\pi/4\right)} = -1 \tag{3.1.69}$$

and the first excited state will be given by, according to the the obtained relation,

$$\phi_B^{(1)} = A\cos\left(\frac{3\pi}{2L}y\right) \tag{3.1.70}$$

$$\phi_A^{(1)} = -\frac{1}{\epsilon}\partial_y\psi_B = A\sin\left(\frac{3\pi}{2L}y\right) \tag{3.1.71}$$

3.1.3. The Polynomial Method

3.1.3.1. Uniform Boundary Conditions $t = 1$

Let us now use this exact solution as a guide to a polynomial approximation. Imposing the boundary condition $t = 1$, the parities of ϕ_A and ϕ_B will be opposite. Because of this, we choose

$$\psi_B = -\frac{y}{L/2}A \tag{3.1.72}$$

$$\psi_A = A \tag{3.1.73}$$

as the simplest way to satisfy BCs. For the valence band we would swap A and B. We normalize the spinor

$$\int_{-L/2}^{L/2} dy \Psi^\dagger \Psi = |A|^2 \int_{-L/2}^{L/2} dy \begin{bmatrix} 1, & -\frac{2y}{L} \end{bmatrix} \begin{bmatrix} 1 \\ -\frac{2y}{L} \end{bmatrix} = 1$$

which gives us

$$\Psi = \sqrt{\frac{3}{4L}} \begin{bmatrix} 1 \\ -\frac{2y}{L} \end{bmatrix} \tag{3.1.74}$$

The average energy is

$$\begin{aligned} \langle \epsilon \rangle = -i\frac{3}{4L} \int_{-L/2}^{L/2} dy \Psi^\dagger \sigma^y \partial_y \Psi &= -\frac{3}{4L} \int_{-L/2}^{L/2} dy \left(\frac{-2}{L} \right) \\ &= \frac{3}{2L} \end{aligned} \tag{3.1.75}$$

This is already close to the exact value

$$\epsilon_0 = \frac{\pi}{2L} \tag{3.1.76}$$

In Figure 3.1.3 we show a comparison between the exact solution and this variational estimate.

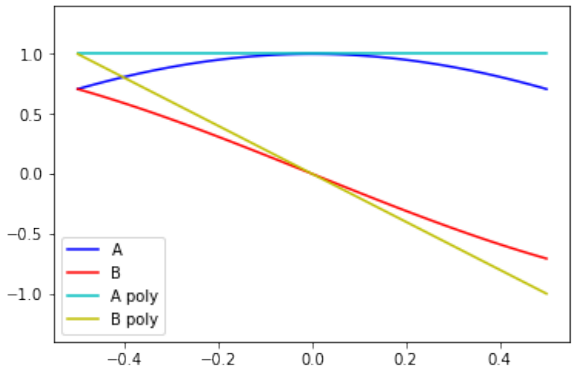

Figure 3.1.3.: Comparison between exact solution and first order polynomial approximation.

To generate higher order polynomials, we take

$$\Psi_0 = A \begin{bmatrix} 1 \\ -\frac{2y}{L} \end{bmatrix} \tag{3.1.77}$$

and multiply by a polynomial in y

$$\Psi = A \begin{bmatrix} 1 \\ -\frac{2y}{L} \end{bmatrix} \mathcal{P}(y)$$

Because the factor Ψ_0 always remains, the boundary conditions will still be satisfied.

As an example, choose $\mathcal{P}(y) = y$. The resulting spinors are

$$\Psi_0 = A \begin{bmatrix} 1 \\ -\frac{2y}{L} \end{bmatrix}$$
$$\Psi_1 = B \begin{bmatrix} y \\ -\frac{2y^2}{L} \end{bmatrix}$$

and we have that

$$\langle \Psi_0 | \Psi_1 \rangle = 0$$

Now, we can write a 2×2 matrix

$$\langle \Psi_i | \hat{H} | \Psi_j \rangle \qquad i, j = 0, 1$$

which we diagonalize to refine the obtained energy value. In this case, however, parity implies

$$\langle \Psi_1 | \hat{H} | \Psi_0 \rangle = B^* A(-i\hbar v_F) \int_{-L/2}^{L/2} dy y \left(-\frac{2}{L} \right) = 0$$

But in the next order

$$\Psi_2 = C \begin{bmatrix} y^2 \\ -\frac{2y^3}{L} \end{bmatrix}$$

the only necessary Gram-Schmidt orthogonalization is between Ψ_2 and Ψ_0, and the matrix full matrix becomes

$$\langle \Psi_i | \hat{H} | \Psi_j \rangle = \begin{pmatrix} 1.5 & 0 & 0.381881 \\ 0 & 4.16667 & 0 \\ 0.381881 & 0 & 6.41667 \end{pmatrix}$$

It is important to note that, so that we obtain sensible energies when we increase the basis size, we must also consider the negative-energy (valence band) states both when generating the basis through Gram-Schmidt orthogonalization and when integrating the Hamiltonian matrix.

These can be obtained, for the situation of the uniform boundary conditions, by

$$\Phi_n = \sigma_x \Psi_n = \begin{pmatrix} \psi_B \\ \psi_A \end{pmatrix} \tag{3.1.78}$$

This can be seen by explicitly applying σ_x to the Hamiltonian (as they anti-commute, and $(\sigma_x)^2$ is just the identity matrix):

$$\begin{aligned} \sigma_x \mathcal{H} \sigma_x \left(\sigma_x \Psi\right) &= E \left(\sigma_x \Psi\right) \\ -\mathcal{H} \sigma_x \sigma_x \left(\sigma_x \Psi\right) &= E \left(\sigma_x \Psi\right) \\ -\mathcal{H} \left(\sigma_x \Psi\right) &= E \left(\sigma_x \Psi\right) \\ \mathcal{H} \left(\sigma_x \Psi\right) &= -E \left(\sigma_x \Psi\right) \end{aligned} \tag{3.1.79}$$

With this, we can clearly see that the boundary conditions remain the same:

$$\frac{\psi_B}{\psi_A} = \pm 1 \implies \frac{\psi_A}{\psi_B} = \frac{1}{\pm 1} = \pm 1$$

Considering a basis size of 16 (8 positive- and 8 negative-energy states), we obtain a spectrum (Figure 3.1.4) which is in good agreement with the exact solution.

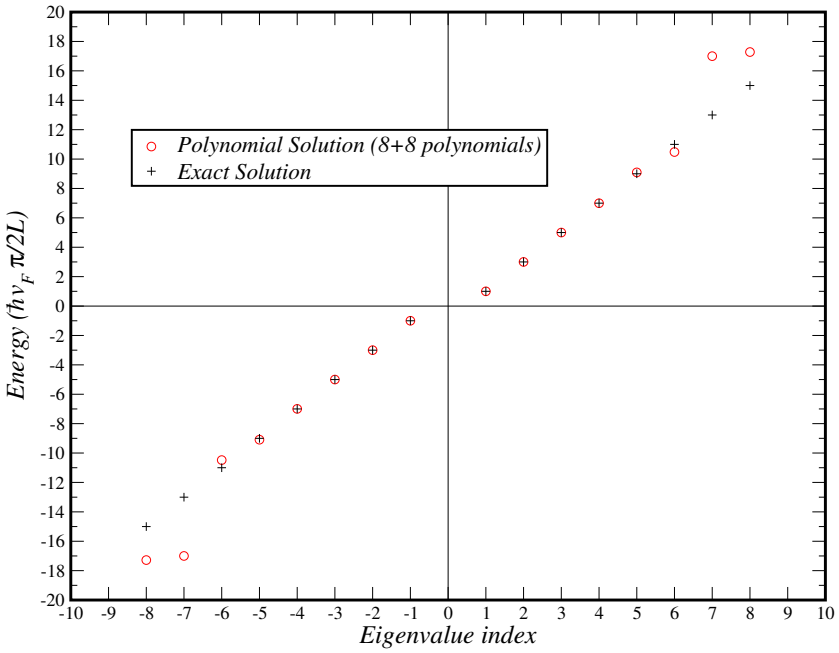

Figure 3.1.4.: Comparison between the exact solution and the polynomial eigenvalues for the uniform boundary condition.

We also analyze the convergence of the first three energy levels as the basis size increases (Figure 3.1.5).

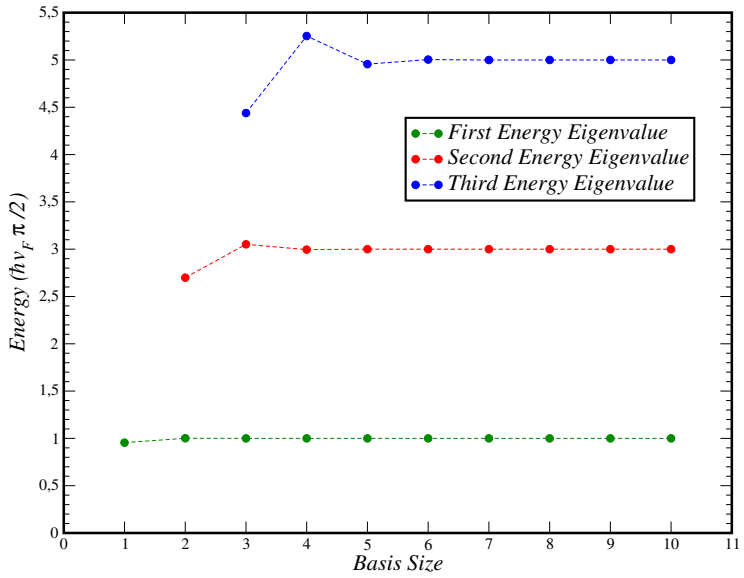

Figure 3.1.5.: Convergence of the three lowest energy eigenvalues.

Comparing now the wave-function of the lowest-energy mode with the exact solution (Figure 3.1.6), we see that the convergence of this state is extremely fast, with it precisely matching the exact solution (as expected by the energy eigenvalue).

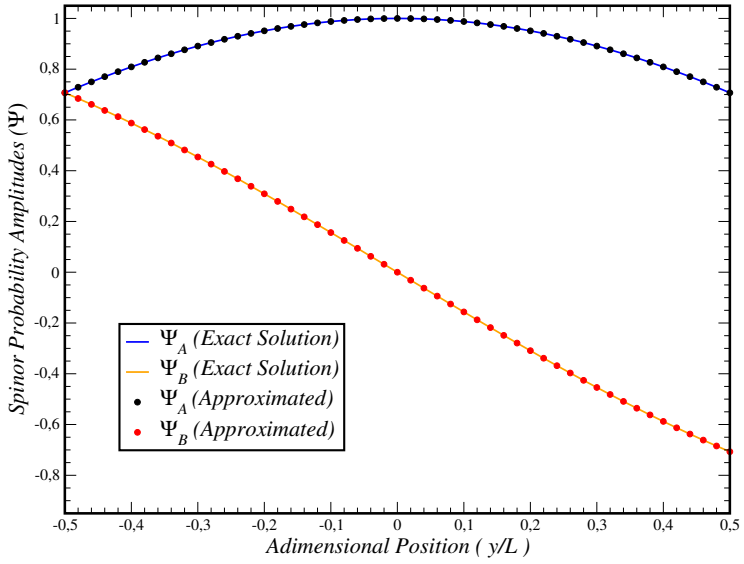

Figure 3.1.6.: Comparison between the exact solution (full lines) and the lowest-energy polynomial eigenfunction (dots) for 16 polynomials.

3.1.3.2. Non-Uniform Boundary Conditions

The previous considerations assume the the medium confining the fermions is uniform. In other words, t is constant. But we can envisage situations in which it varies from boundary to boundary. For instance we could have $t = 0$ at $y = L/2$ ($\phi_B = 0$) and $t = +\infty$ at $y = -L/2$ ($\phi_A = 0$), the BCs corresponding to zigzag edges [40]. A ket that satisfies the imposed boundary conditions is

$$\Psi_0 = A \begin{bmatrix} L/2 + y \\ L/2 - y \end{bmatrix} \tag{3.1.80}$$

It is important to note that, due to the change of BCs relatively to the uniform situation, the negative-energy state will no longer be obtained by applying σ_x to this ket, as it would switch the boundary conditions for their inverse. Instead, we obtain it by applying σ_z as only switches $\phi_B \to -\phi_B$ and does not affect the boundary conditions ($-1 \cdot 0 = 0$). Explicitly, because $\sigma_z^2 = \mathrm{Id}$ and

$$\sigma_z \mathcal{H} \sigma_z = -\mathcal{H} \tag{3.1.81}$$

$$\begin{aligned} \sigma_z \mathcal{H} \sigma_z \left(\sigma_z \Psi\right) &= E \left(\sigma_z \Psi\right) \\ -\mathcal{H} \left(\sigma_z \Psi\right) &= E \left(\sigma_z \Psi\right) \\ \mathcal{H} \left(\sigma_z \Psi\right) &= -E \left(\sigma_z \Psi\right) \end{aligned} \tag{3.1.82}$$

As such, the negative-energy state will be

$$\Phi_0 = \sigma_z \Psi_0 = A \begin{bmatrix} L/2 + y \\ -\left(L/2 - y\right) \end{bmatrix} \tag{3.1.83}$$

The exact solutions are easily guessed

$$\begin{aligned} \phi_A &= A \sin\left(q(y + L/2)\right) \\ \phi_B &= \frac{1}{sq} \partial_y \phi_A = sA \cos\left(q(y + L/2)\right) \end{aligned} \tag{3.1.84}$$

Imposing the boundary condition $\phi_B(L/2) = 0$, we require that

$$\cos\left(qL\right) = 0 \Longrightarrow q_n L = \left(2n + 1\right) \frac{\pi}{2}$$

Remarkably, this is the same spectrum as we obtained for $t = 1$.

In Figure 3.1.7 we compare the exact solution and the lowest order polynomial approximation.

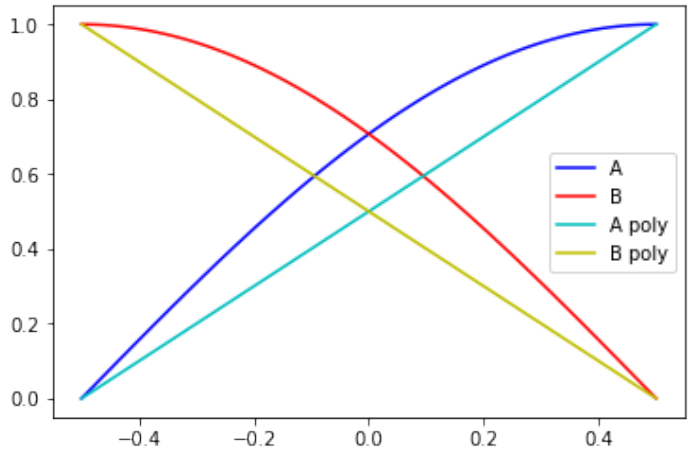

Figure 3.1.7.: Comparison between exact solution and first order polynomial approximation.

As seen previously, the spectrum is the same as the one for the uniform solution, visible here in Figure 3.1.8.

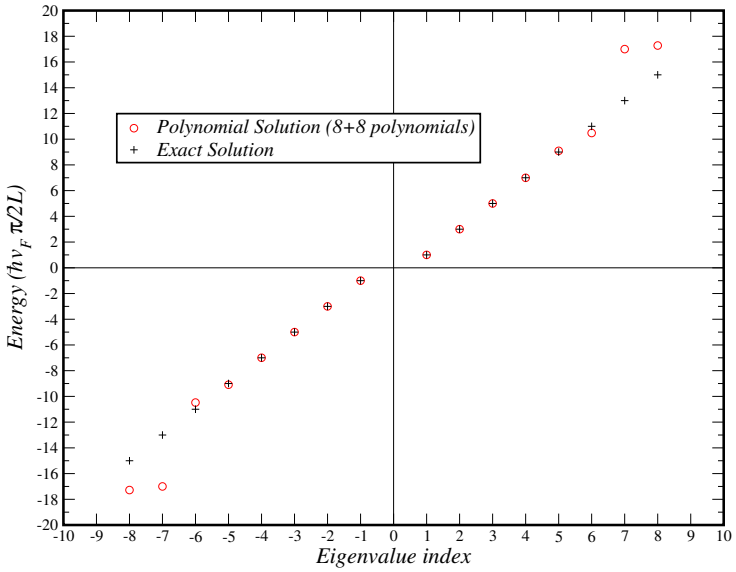

Figure 3.1.8.: Comparison between the exact solution and the polynomial eigenvalues for the non-uniform boundary condition.

Comparing now the wave-function of the lowest-energy mode with the exact solution (Figure 3.1.9), we see that the convergence of this state is extremely fast, with it precisely matching the exact solution (as expected by the energy eigenvalue).

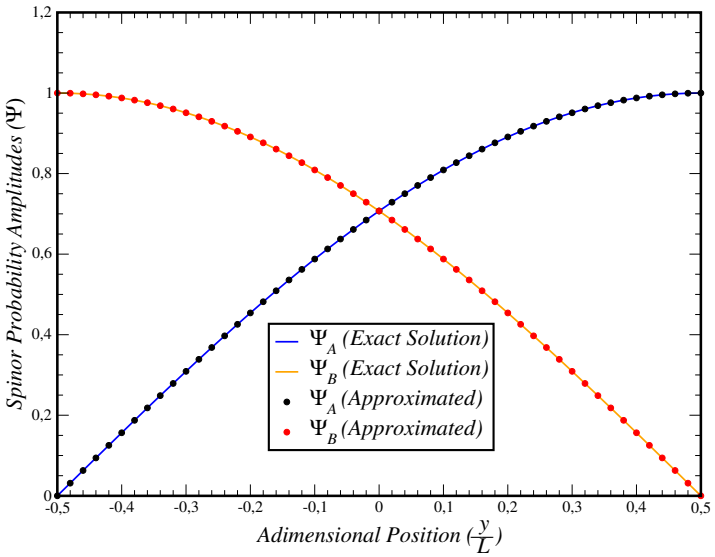

Figure 3.1.9.: Comparison between the exact solution (full lines) and the lowest-energy polynomial eigenfunction (dots) for 16 polynomials.

3.1.3.3. Uniform Boundary Condition with $t = 0$

The problem for $t = 0$ in both boundaries has a different spectrum (Equation 3.1.60). In particular, this one has an exactly zero-energy state that is easily written as

$$\Psi_0(y) = \begin{bmatrix} 1 \\ 0 \end{bmatrix} \tag{3.1.85}$$

It is important to note that the polynomial approximation will not generate this state. Dirac's equation implies that the parity of the two components is opposite, for $E \neq 0$. The simplest choice of non-zero function for ψ_B that satisfies the required boundary conditions is

$$\psi_B(y) = \left(\frac{L}{2} - y\right)\left(\frac{L}{2} + y\right) = \frac{L^2}{4} - y^2 \tag{3.1.86}$$

As such, a simple choice for the starting state in our polynomial method would be (non-normalized)

$$\Psi_{1\,c}(y) = \begin{bmatrix} y \\ \frac{L^2}{4} - y^2 \end{bmatrix} \qquad \Psi_{1\,v}(y) = \sigma_z \cdot \begin{bmatrix} y \\ \frac{L^2}{4} - y^2 \end{bmatrix} \tag{3.1.87}$$

Higher order states would then be generated as before,

$$\Psi_{i\,c,v} = y^{i-1}\Psi_{1\,c,v} \tag{3.1.88}$$

with the necessary Gram-Schmidt orthogonalization afterwards.

The obtained spectrum, including the single-zero energy state, is visible in Figure 3.1.10.

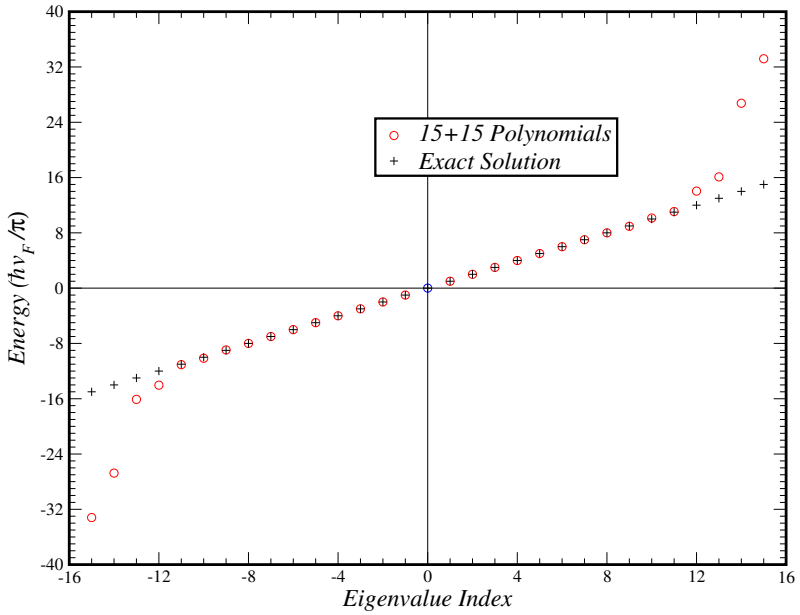

Figure 3.1.10.: Spectrum for the 1D $t = 0$ problem with $15+15$ polynomials compared against the exact solution.

Looking at the two eigenfunctions with lowest (positive) energy with their respective eigenvalues, we have Figure 3.1.11. These are compared against the exact solution of Equation 3.1.60.

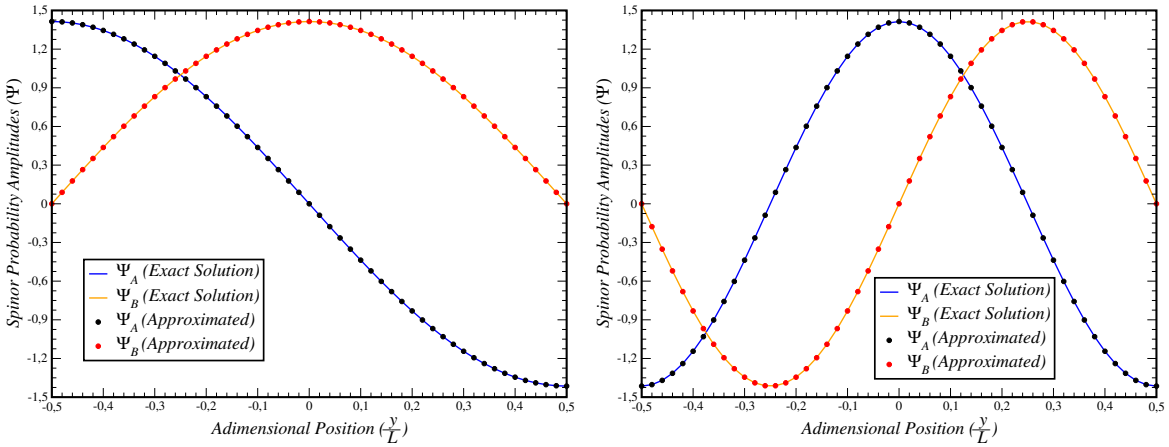

Figure 3.1.11.: Plots of (left to right) $\Psi_{1\,c}$, $\Psi_{2\,c}$

3.2. Exact Solution of the Triangular Enclosure Using C_{3v} Symmetry

In this section, we will be reviewing the treatment used by Gaddah [30] so that we can compare his solutions against our polynomial method. In his paper, the author wants to find analytical solutions to the Dirac equation in a triangular enclosure using the boundary condition equivalent to the discrete zigzag boundary. This boundary condition fixed the spinor element relative to the termination sub-lattice (in this case ψ_A) as zero in the boundary. With our polynomial method, this is equivalent to setting $t = \infty$. As the system is triangular, the edges will have the same sub-lattice termination, which implies that the boundary conditions will be the same.

The author discusses the necessary conditions for the hermiticity of the Dirac Hamiltonian, followed by treating the problem with the system's C_{3v} innate symmetries. Doing this, both the spectrum and the electron probability density are obtained analytically. As we only want to compare the author's results against the ones from our method, we will skip the formal treatment of the problem, and only focus on the results.

The billiard system is defined as Figure 3.2.1.

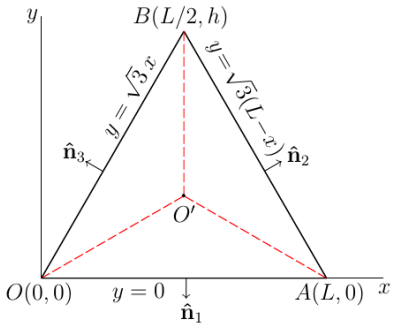

Figure 3.2.1.: Equilateral triangular billiard of side L and height $h = \frac{\sqrt{3}}{2}L$, $\mathbf{n}_1$, $\mathbf{n}_2$, $\mathbf{n}_3$ are the unit vectors normal to the sides of the triangle.

The obtained spinor is given by (ignoring any multiplicative constants)

$$\Psi^{(\pm,j)}_{n_1,n_2}\left(\overrightarrow{r}\right) = \begin{pmatrix} 1 \\ 0 \end{pmatrix} \phi^{(j)}_{n_1,n_2}\left(\overrightarrow{r}\right) + \begin{pmatrix} 0 \\ 1 \end{pmatrix} \frac{\hbar c}{E_{n_1,n_2}} \left(\partial_y - i\partial_x\right) \phi^{(j)}_{n_1,n_2}\left(\overrightarrow{r}\right) \tag{3.2.1}$$

where $\phi^{(j)}_{n_1,n_2}\left(\overrightarrow{r}\right)$ is given by

$$\phi^{(j)}_{n_1,n_2}(x,y) = \begin{cases} \mathcal{C}_1 \left\{ -\sin\left[q\left(n_2+2n_1\right)x\right] \sin\left[\sqrt{3}qn_2y\right] + \sin\left[q\left(n_1+2n_2\right)x\right] \sin\left[\sqrt{3}qn_1y\right] + \right. \\ \qquad \left. + \sin\left[q\left(n_1-n_2\right)x\right] \sin\left[\sqrt{3}q\left(n_2+n_1\right)y\right] \right\}, & j = 1 \\ \mathcal{C}_2 \left\{ -\cos\left[q\left(n_2+2n_1\right)x\right] \sin\left[\sqrt{3}qn_2y\right] - \cos\left[q\left(n_1+2n_2\right)x\right] \sin\left[\sqrt{3}qn_1y\right] + \right. \\ \qquad \left. + \cos\left[q\left(n_1-n_2\right)x\right] \sin\left[\sqrt{3}q\left(n_2+n_1\right)y\right] \right\}, & j = 2 \end{cases} \tag{3.2.2}$$

After this, we want to analyze the spectrum of this equation, as well as obtaining some visualizations of the wave functions (for clarity, we will use density plots).

The spectrum will be given by

$$E^{(\pm)}_{n_1,n_2} = \pm\frac{4\pi}{3L}\hbar c\sqrt{\left(n_1^2+n_2^2+n_1n_2\right)} \tag{3.2.3}$$

where $n_{1,2}$ have to satisfy

$$\begin{aligned} n_2 > n_1 > 0, \;\; j=1 \\ n_2 \geq n_1 > 0, \;\; j=2 \end{aligned}$$

Due to this relation, every state with $n_1 \neq n_2$ will be, at least, $2\times$ degenerate.

To visualize the probability density of the wave functions, we need to first write the full Dirac spinor:

$$\Psi^{(\pm,j)}_{n_1,n_2}\left(\overrightarrow{r}\right) = N^{(\pm)}_{n_1,n_2}\left[\phi^{(j)}_{n_1,n_2}\left(\overrightarrow{r}\right)|\uparrow\rangle + \chi^{(\pm,j)}_{n_1,n_2}\left(\overrightarrow{r}\right)|\downarrow\rangle\right], \quad \forall j=1,2 \tag{3.2.4}$$

where $|\uparrow\rangle$ and $|\downarrow\rangle$ are the usual eigenvectors of the Pauli spin operator

$$|\uparrow\rangle = \begin{pmatrix} 1 \\ 0 \end{pmatrix} \qquad\qquad |\downarrow\rangle = \begin{pmatrix} 0 \\ 1 \end{pmatrix} \tag{3.2.5}$$

$$\mathbf{S} = \frac{\hbar}{2}\begin{pmatrix} 1 & 0 \\ 0 & -1 \end{pmatrix} \tag{3.2.6}$$

For $n_2 > n_1 > 0$, there are two Dirac spinors $\Psi^{(\pm,1)}_{n_1,n_2}$ and $\Psi^{(\pm,2)}_{n_1,n_2}$ with the same energy eigenvalue. For the case where $n_2 = n_1$, the only allowed spinor is $\Psi^{(\pm,2)}_{n_1,n_2}$ $\left(\Psi^{(\pm,1)}_{n_1,n_2}\right.$ would be zero). $N^{(\pm)}_{n_1,n_2}$ is the normalization constant given by

$$N^{(\pm)}_{n_1,n_2} = \frac{1}{\sqrt{2}}$$

As before, $\chi^{(\pm,j)}_{n_1,n_2}$ is given by

$$\chi^{(\pm,j)}_{n_1,n_2} = \eta^{(\pm)}_{n_1,n_2}\left(\partial_y - i\partial_x\right)\phi^{(j)}_{n_1,n_2} \tag{3.2.7}$$

with

$$\eta^{(\pm)}_{n_1,n_2} = \frac{1}{\pm\frac{4\pi}{3L}\sqrt{\left(n_1^2+n_2^2+n_1n_2\right)}}$$

By substitution on Ψ, we obtain the general solution

$$\Psi^{(\pm,j)}_{n_1,n_2}\left(\overrightarrow{r}\right) = \frac{1}{\sqrt{2}}\left[\phi^{(j)}_{n_1,n_2}\left(\overrightarrow{r}\right)|\uparrow\rangle \pm \frac{3L}{4\pi\sqrt{\left(n_1^2+n_2^2+n_1n_2\right)}}\left(\partial_y - i\partial_x\right)\phi^{(j)}_{n_1,n_2}\left(\overrightarrow{r}\right)|\downarrow\rangle\right], \quad \forall j=1,2 \tag{3.2.8}$$

The relativistic probability density $\rho^{(\pm,j)}_{n_1,n_2}$ can be written from $\phi^{(j)}_{n_1,n_2}$ by simple substitution, which gives

$$\rho^{(\pm,j)}_{n_1,n_2}(x,y) = \Psi^{(\pm,j)\dagger}_{n_1,n_2}\Psi^{(\pm,j)}_{n_1,n_2} = \left(N^{(\pm)}_{n_1,n_2}\right)^2\left[\left(\phi^{(j)}_{n_1,n_2}(x,y)\right)^2 + \left(\eta^{(\pm)}_{n_1,n_2}\nabla\phi^{(j)}_{n_1,n_2}(x,y)\right)^2\right] \tag{3.2.9}$$

By construction of the wave functions, each of these probability densities will have the symmetries of the triangle.

In Figure 3.2.2 we visualize the obtained spectrum.

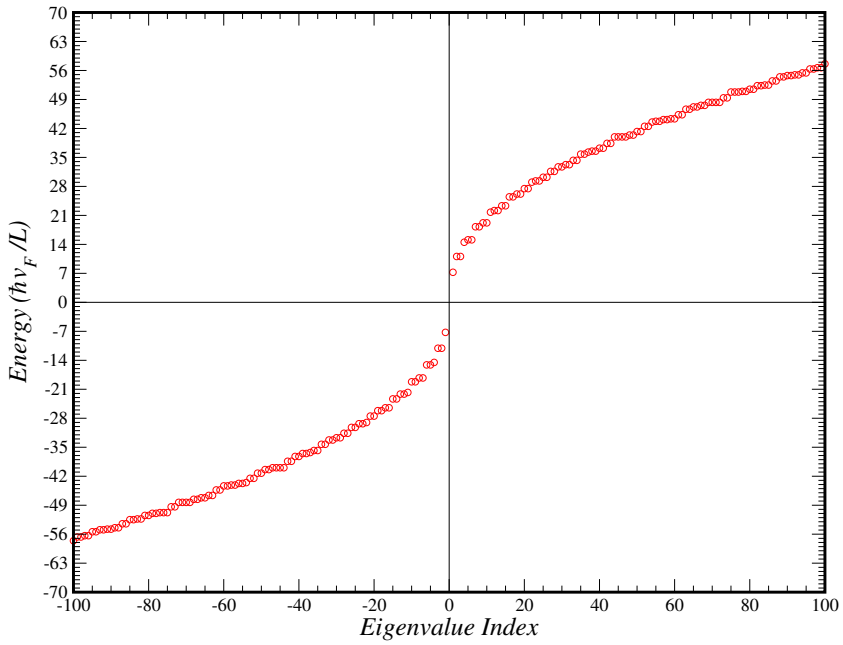

Figure 3.2.2.: Energy levels obtained by Gaddah for the zigzag-like triangular billiards.

This symmetry-inspired method presents a gap between $-\frac{4\pi}{3L}\hbar v_F\sqrt{3}$ and $\frac{4\pi}{3L}\hbar v_F\sqrt{3}$. The density plots for the normalized relativistic probability densities were done in *Wolfram Mathematica*® and can be seen in Appendix B.2.

3.3. Triangular Enclosure With the Polynomial Method

The solution that Gaddah presented [30] is essentially the one for Schrödinger's equation: Gaddah imposes the Dirichlet boundary condition in one of the sub-lattices, and then solves the Helmholtz equation for that same spinor element, taking the square root of the energy eigenvalues in the end. As the eigenvalues are known, the missing spinor element can be obtained directly by applying the Dirac operator and dividing by the specific eigenvalue. This means that we can apply our polynomial method exactly as was done in the case of Schrödinger's equation, with the only difference being that we are now solving for E^2.

We will first redefine the enclosure as centered at the origin, as seen in Figure 3.3.1.

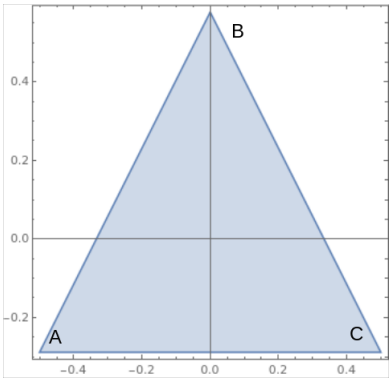

Figure 3.3.1.: Triangular billiard of side $L = 1$.

Writing the vertex coordinates for a general L, as well as the equations for the edges, we have that

$$A = \frac{L}{2}\left(-1, -\frac{1}{\sqrt{3}}\right) \qquad B = \frac{L}{2}\left(0, \frac{2}{\sqrt{3}}\right) \qquad C = \frac{L}{2}\left(1, -\frac{1}{\sqrt{3}}\right)$$
$$y_{\mathrm{AB}} = \sqrt{3}\left(\frac{L}{3} + x\right) \qquad y_{\mathrm{BC}} = \sqrt{3}\left(\frac{L}{3} - x\right) \qquad y_{\mathrm{CA}} = -\frac{L}{2\sqrt{3}}$$

and that the integration region is given by

$$\iint_A dxdy \to \int_{-\frac{L}{2\sqrt{3}}}^{\frac{L}{\sqrt{3}}} dy \int_{-\frac{L}{3}+\frac{y}{\sqrt{3}}}^{\frac{L}{3}-\frac{y}{\sqrt{3}}} dx$$

As we chose zigzag-like BCs, we have that the sub-lattice termination is the same in all three edges. As such, we have the Dirichlet boundary condition

$$\phi_A = 0 \tag{3.3.1}$$

Because of this boundary condition, this is a Helmholtz problem for ϕ_A with Dirichlet boundary conditions, and the solution for ϕ_B will be obtained by simply applying the Dirac operator

(and dividing by the energy eigenvalue)

$$\phi_B(x,y) = -i\frac{\hbar v_F}{E}\left(\partial_x + i\partial_y\right)\phi_A(x,y) \tag{3.3.2}$$

As such, a function written as (including a normalization constant N_0)

$$\phi_A(x,y) = N_0\left[\frac{L}{\sqrt{3}} + \left(\sqrt{3}x - y\right)\right]\left[\frac{L}{\sqrt{3}} - \left(\sqrt{3}x + y\right)\right]\left[\frac{L}{2\sqrt{3}} + y\right] \tag{3.3.3}$$

satisfies the imposed boundary conditions.

Therefore, the partial differential equation whose eigenvalues we are now looking for is

$$-\nabla^2\psi_A(x,y) = \epsilon^2\psi_A(x,y) \tag{3.3.4}$$

which should give us the same spectrum as Equation 3.2.3.

Performing the density plots of the $\phi_{A,B}$ terms of this spinor, we obtain Figures 3.3.2. Considering that these are simply the first polynomial approximation to the wavefunctions, these density plots are already extremely similar (after swapping the sub-lattices) to the ones obtained by Gaddah [30] visible in Appendix B.2 (the top-middle and top-right density plots visible in the first page of the appendix in question).

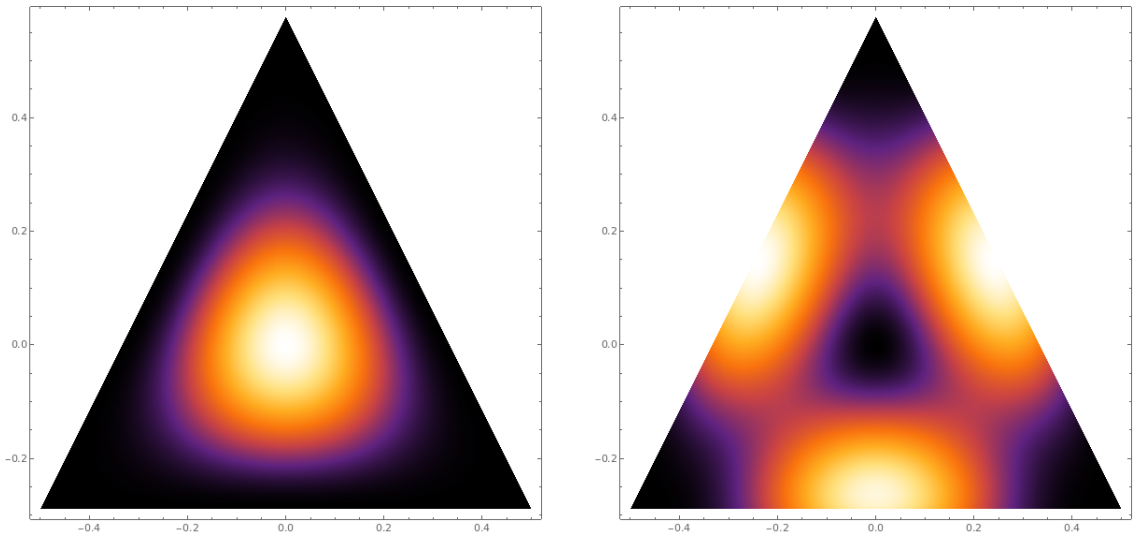

Figure 3.3.2.: Density plot of $|\phi_A|^2$ (left) and $|\phi_B|^2$ (right) for the triangular enclosure with zigzag-like boundary conditions.

Taking the eigenvectors of the Hamiltonian (with a basis size of 10 polynomials) and multiplying them by the basis, we obtain the ϕ_A eigenfunctions of the system. Applying the Dirac operator (Equation 3.3.2), we immediately get the $\phi_B(x,y)$ eigenfunctions. We can then plot the modulus of the second, third and fourth eigenfunctions for each spinor element, obtaining Figure 3.3.3.

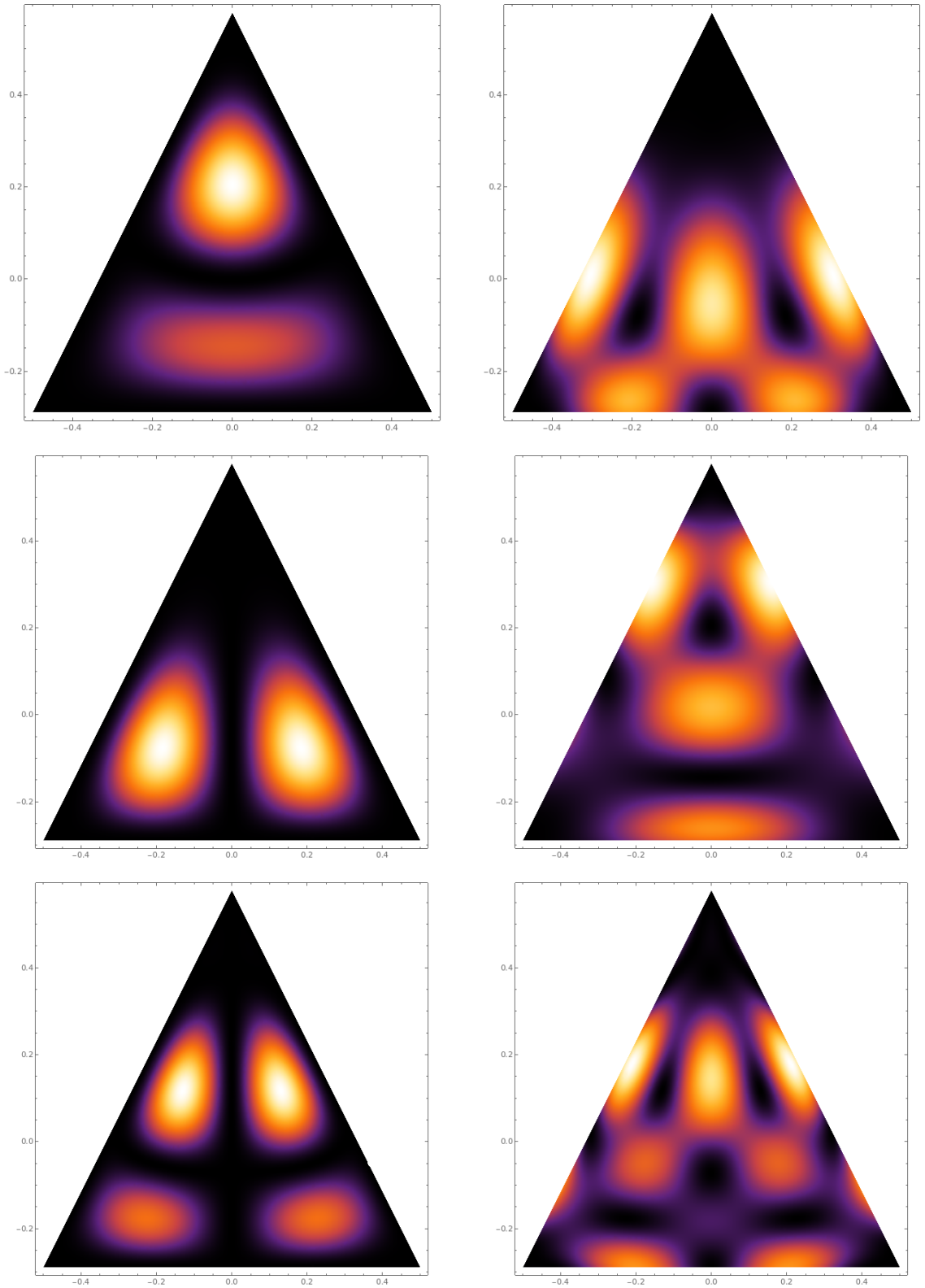

Figure 3.3.3.: Density plots of (left to right, top to bottom) $|\phi_{A1}|^2$, $|\phi_{B1}|^2$, $|\phi_{A2}|^2$ and $|\phi_{B2}|^2$ for the triangular enclosure with zigzag-like boundary conditions.

These density plots (obtained for 15 polynomials) are already almost identical to the ones Gaddah presents (Section B.2). We diagonalize the Hamiltonian matrix for a basis of 120 polynomials and compare the obtained spectrum with the previously mentioned exact result. In Figure 3.3.4 we plot the positive non-diverging part of the spectrum for comparison.

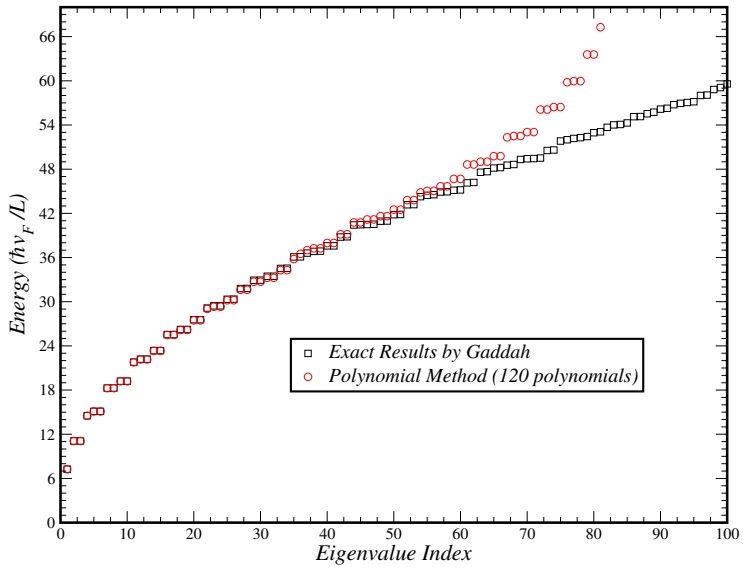

Figure 3.3.4.: Spectrum of the zigzag-like-BCs triangular graphene dot with 120 polynomials compared against Gaddah's exact solution.

The plot in Figure 3.3.4 shows us that our polynomial method is able to replicate the exact solution found by Gaddah. The apparent deviation for higher eigenvalue indexes is due to the truncation of the basis, which does not invalidate our results. We find the gap to be approximately

$$\Delta \approx 2 \times 7.26 \, \frac{\hbar v_F}{L}$$

which matches almost exactly with Gaddah's gap of

$$\Delta_{\text{exact}} = 2 \times \frac{4\pi}{3} \frac{\hbar v_F}{L} \sqrt{3} \tag{3.3.5}$$

A few extra density plots of the eigenfunctions for the A sub-lattice are available in Appendix B.3. As the basis was truncated at 10 polynomials, the higher order eigenfunctions have not yet converged to their expected behaviour.

3.3.1. Analysis of this problem

As we have observed, this problem adds nothing new to our understanding of Dirac's equation in finite enclosures. Due to the Dirichlet boundary conditions, it reduced to Schrödinger's equation, for which our polynomial method already works.

One question remains: we can write solutions to the Dirac-Weyl equation that have an exactly-zero eigenvalue. In this case, as we are fixing

$$\begin{aligned} \phi_A &= 0 \\ (\partial_x - i\partial_y)\,\phi_B &= 0 \end{aligned} \tag{3.3.6}$$

in the edges, we can define a new coordinate system

$$\begin{aligned} z &= x + iy \\ \bar{z} &= x - iy \end{aligned} \tag{3.3.7}$$

which means that Equation 3.3.6 changes to

$$\begin{aligned} \phi_A &= 0 \\ \partial_z \phi_B &= 0 \end{aligned} \tag{3.3.8}$$

This lets us write a solution that respects both of as any function (normalized by N) of the form

$$\Psi\left(\bar{z}\right) = N \begin{bmatrix} 0 \\ f\left(\bar{z}\right) \end{bmatrix}. \tag{3.3.9}$$

This gives us an uncountable number of zero-energy states, which raise a question: what is the meaning of these states? This is a question that remains unanswered.

We will now solve the Dirac equation in polar coordinates with infinite-mass boundary conditions ($t = 1$) as a stepping stone towards applying our polynomial method to polygonal enclosures.

3.4. Dirac-Weyl Equation in Polar Coordinates

As the geometry of the problem in question favours polar coordinates, we need to re-write the Dirac-Weyl equation. Starting from its general form [23] in one of the Dirac points ($\mathcal{K}$), we have

$$\hbar v_F \left(\sigma \cdot \frac{\nabla}{i} \right) \psi = \epsilon \psi \tag{3.4.1}$$

Rearranging the terms, we have

$$\left(\sigma \cdot \frac{\nabla}{i} \right) \psi = s q_\epsilon \psi \tag{3.4.2}$$

where

$$q_\epsilon = \frac{|\epsilon|}{\hbar v_F} \tag{3.4.3}$$

and $s = \pm 1$ is the band index (i.e., the sign of ϵ).

In polar coordinates, the gradient operator is

$$\nabla = \mathbf{e}_r \frac{\partial}{\partial r} + \mathbf{e}_\theta \frac{1}{r} \frac{\partial}{\partial \theta} \tag{3.4.4}$$

and the unit vectors are

$$\begin{aligned} \mathbf{e}_r &= (\cos\theta, \sin\theta) \\ \mathbf{e}_\theta &= (-\sin\theta, \cos\theta) \end{aligned} \tag{3.4.5}$$

Using this, we get

$$\left(\sigma \cdot \frac{\nabla}{i} \right) = -i \left[\sigma_r \frac{\partial}{\partial r} + \sigma_\theta \frac{1}{r} \frac{\partial}{\partial \theta} \right] \tag{3.4.6}$$

where

$$\sigma_r = \begin{bmatrix} 0 & e^{-i\theta} \\ e^{i\theta} & 0 \end{bmatrix}$$

and

$$\sigma_\theta = \begin{bmatrix} 0 & -ie^{-i\theta} \\ ie^{i\theta} & 0 \end{bmatrix} \tag{3.4.7}$$

Applying this equation to the general 2-spinor

$$\psi = \begin{pmatrix} \psi_A \\ \psi_B \end{pmatrix} \tag{3.4.8}$$

we get

$$\begin{aligned} e^{-i\theta} \frac{\partial}{\partial r} \psi_B - ie^{-i\theta} \frac{1}{r} \frac{\partial}{\partial \theta} \psi_B &= isq_\epsilon \psi_A \\ e^{i\theta} \frac{\partial}{\partial r} \psi_A + ie^{i\theta} \frac{1}{r} \frac{\partial}{\partial \theta} \psi_A &= isq_\epsilon \psi_B \end{aligned} \tag{3.4.9}$$

Let us define the solutions to this equation in the form

$$\begin{aligned}\psi_A &= e^{im\theta} f_A(r)\\ \psi_B &= e^{i(m+1)\theta} f_B(r)\end{aligned} \tag{3.4.10}$$

By direct substitution, we get

$$\begin{aligned}e^{im\theta}\frac{\partial}{\partial r} f_B - ie^{im\theta}\frac{1}{r} i(m+1) f_B &= isq_\epsilon e^{im\theta} f_A\\ e^{i(m+1)\theta}\frac{\partial}{\partial r} f_A + ie^{i(m+1)\theta}\frac{1}{r} imf_A &= isq_\epsilon e^{i(m+1)\theta} f_B\end{aligned} \tag{3.4.11}$$

which simplifies (by factorization of the exponentials) to

$$\begin{aligned}\frac{\partial}{\partial r} f_B + \frac{1}{r}(m+1) f_B &= isq_\epsilon f_A\\ \frac{\partial}{\partial r} f_A - \frac{1}{r} mf_A &= isq_\epsilon f_B\end{aligned} \tag{3.4.12}$$

Defining the new variable $u = q_\epsilon r$, we have

$$\begin{aligned}\frac{\partial}{\partial u} f_B + \frac{(m+1)}{u} f_B &= isf_A\\ \frac{\partial}{\partial u} f_A - \frac{m}{u} f_A &= isf_B\end{aligned} \tag{3.4.13}$$

These equations are quite familiar. From the definition of the recursion relations for the Bessel functions, we have

$$\begin{aligned}\frac{d}{dz}\mathcal{J}_\nu(z) + \frac{\nu}{z}\mathcal{J}_\nu(z) &= \mathcal{J}_{\nu-1}(z)\\ \frac{d}{dz}\mathcal{J}_\nu(z) - \frac{\nu}{z}\mathcal{J}_\nu(z) &= -\mathcal{J}_{\nu+1}(z)\end{aligned} \tag{3.4.14}$$

As $s^2 = 1$, we can multiply the first relation by is and redefine $\nu \to \nu + 1$, as well as multiply the right-hand side of the second equation by s^2 and factorize $-1 = i^2$, and we get

$$\begin{aligned}\frac{d}{dz}\left[is\mathcal{J}_{\nu+1}(z)\right] + \frac{\nu+1}{z}\left[is\mathcal{J}_{\nu+1}(z)\right] &= is\mathcal{J}_\nu(z)\\ \frac{d}{dz}\mathcal{J}_\nu(z) - \frac{\nu}{z}\mathcal{J}_\nu(z) &= is\left[is\mathcal{J}_{\nu+1}(z)\right]\end{aligned} \tag{3.4.15}$$

which gives us the solutions for Equation 3.4.13:

$$\begin{aligned}f_A(r) &= \mathcal{J}_m(q_\epsilon r)\\ f_B(r) &= is\mathcal{J}_{m+1}(q_\epsilon r)\end{aligned} \tag{3.4.16}$$

With this, we get the 2-spinor

$$\psi_\epsilon(r,\theta) = \begin{bmatrix} e^{im\theta}\mathcal{J}_m(q_\epsilon r) \\ ise^{i(m+1)\theta}\mathcal{J}_{m+1}(q_\epsilon r) \end{bmatrix} \tag{3.4.17}$$

The current operator is defined as

$$\mathbf{j} = v_F\psi^\dagger\sigma\psi \tag{3.4.18}$$

In polar coordinates, we have (by direct application of σ_r and σ_θ) the components

$$j_r = v_F\psi^\dagger \begin{bmatrix} 0 & e^{-i\theta} \\ e^{i\theta} & 0 \end{bmatrix}\psi \tag{3.4.19}$$

and

$$j_\theta = v_F\psi^\dagger \begin{bmatrix} 0 & -ie^{-i\theta} \\ ie^{i\theta} & 0 \end{bmatrix}\psi \tag{3.4.20}$$

To have a confined state at $r = R$, we must have zero radial current, i.e. no electrons cross to the outside of the boundary. Expanding j_r, we get

$$\begin{aligned} j_r &= e^{-i\theta}\psi_A^*\psi_B + e^{i\theta}\psi_B^*\psi_A \\ &= 0 \end{aligned} \tag{3.4.21}$$

which implies that, seeing as the second element of the right-hand side is just the complex conjugate of the first element,

$$e^{-i\theta}\psi_A^*\psi_B + \left(e^{-i\theta}\psi_A^*\psi_B\right)^* = 0 \tag{3.4.22}$$

which simplifies to

$$\mathfrak{Re}\left[e^{-i\theta}\psi_A^*\psi_B\right] = 0 \tag{3.4.23}$$

This requires that either

$$\psi_B = Ce^{i\frac{\pi}{2}}e^{i\theta}\psi_A, \;\; C \in \mathbb{R} \tag{3.4.24}$$

or

$$\psi_A = 0 \tag{3.4.25}$$

Infinite mass confinement implies (as we will see further ahead in Equation 3.1.12) that $C = 1$ [39, 41], which in turn simplifies to

$$\psi_B = ie^{i\theta}\psi_A \tag{3.4.26}$$

Replacing the eigenstates found in Equation 3.4.17, we get that either

$$\psi_A = 0 \Leftrightarrow \psi_B = 0 \tag{3.4.27}$$

or that

$$is\mathcal{J}_{m+1}(q_\epsilon R) = i\mathcal{J}_m(q_\epsilon R) \tag{3.4.28}$$

which (rearranging the terms) means that the valid energy levels will be the ones given by

$$\epsilon = q_\epsilon \hbar v_F \tag{3.4.29}$$

where q_ϵ obeys the condition for the absence of normal current to the edge given by Equation 3.4.30

$$\frac{\mathcal{J}_{m+1}\left(q_\epsilon R\right)}{\mathcal{J}_m\left(q_\epsilon R\right)} = s \tag{3.4.30}$$

This is the same condition that we found for the infinite mass confinement with our polynomial ($t = 1$).

3.4.1. Circular Boundary

From what we obtained in the previous section, we now need to find the energy values for which the condition Equation 3.4.30 is satisfied. According Bourget's hypothesis [42] (proved in 1929 by Siegel [43] for m up to 4), for any two integers $n \geq 0$ and $m \geq 1$, the functions $\mathcal{J}_n\left(x\right)$ and $\mathcal{J}_{n+m}\left(x\right)$ have no common zeros other than the one at $x = 0$, which prevents any $\frac{0}{0}$ situations. Because of this, the condition from Equation 3.4.27 can be ignored.

As we are dealing with a circular boundary, the radius is just a constant R and we have Equation 3.4.30

$$\frac{\mathcal{J}_{m+1}\left[q_\epsilon R\right]}{\mathcal{J}_m\left[q_\epsilon R\right]} = s \tag{3.4.31}$$

As an example, for $m = 0$ we have the left side of Figure 3.4.1.

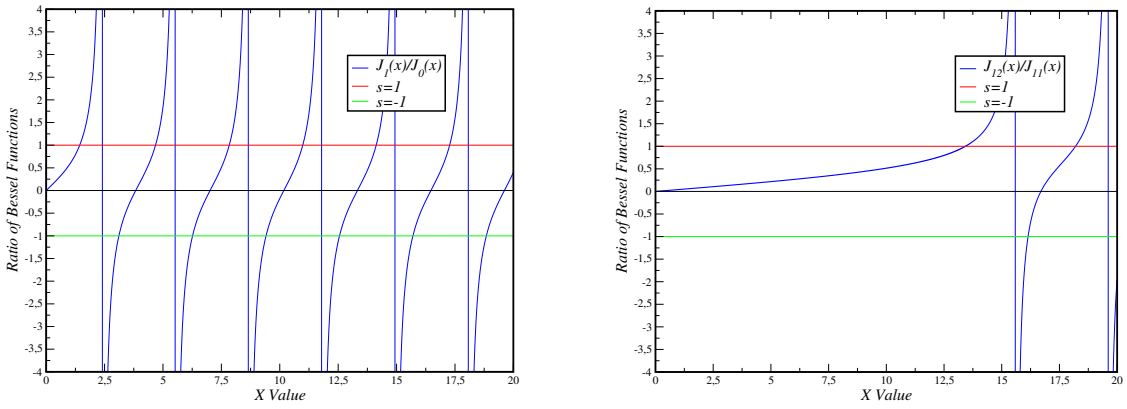

Figure 3.4.1.: Comparison between $\frac{\mathcal{J}_1(x)}{\mathcal{J}_0(x)}$ and $\frac{\mathcal{J}_{12}(x)}{\mathcal{J}_{11}(x)}$.

The allowed energy levels will be the ones where the ratio crosses the red or green lines. As Bourget's hypothesis also states that the zeros of $\mathcal{J}_m$ are situated between the zeros of $\mathcal{J}_{m+1}$. Because of this, when we consider more and more orders of Bessel functions (increasing m), the first values of $q_\epsilon R$ where the ratios cross ± 1 will be further ahead, i.e., at higher and higher energies. As such, the contributions from higher order Bessel functions will not disrupt the lower energy levels. For clarity, we compare between $m = 0$ (left side) and $m = 11$ (right side) in Figure 3.4.1.

The plots for each ratio are displayed in Section B.1.

3.5. Finishing Remarks

In this chapter, we begin by working on generalizing the boundary conditions for Dirac's equation. This generalization was easily verifiable as correct for the 1-dimensional well, as we were able to find exact analytical solutions to use as a comparison. After knowing these boundary conditions and their relation with lattice terminations, we redefined the polynomial method for use in these kinds of systems. This required a reworking of the way we created the conduction- and valence-band states, and both their relation with each other and with the boundary conditions.

After this, we reproduced the results from Gaddah [30] for the exact solution for the triangular billiards. We compared these results against the spectrum obtained from the Helmholtz equation, finding the same features in both curves.

Finally, we solved the Dirac-Weyl equation for the circular flake with infinite-mass boundary conditions with the assistance of Bessel functions.

The final chapters of this thesis will be our attempt to generalize this method for two-dimensional systems that cannot be reduced to a Schrödinger problem, as well as the application of the generalized method to the hexagonal flake with zigzag-like boundary conditions.

4. Two-Dimensional Generalization of our Polynomial Method

In this final chapter, we will apply the polynomial method to both a square with uniform boundaries and an hexagon with zigzag-like boundaries so that we obtain their spectra. We analyze the results we obtain, as well as their origin and validity.

After that, we utilize the Helmholtz equation to study the spectrum of each of these enclosures, and discuss the obtained eigenvalues and eigenfunctions.

Finally, we discuss the validity of the continuum results by Zarenia *et al* [25] and the reason why the exactly zero-energy states appear in these systems.

4.1. The Uniform-Boundary Square

How can we extend the previous considerations to a square domain where we impose $t = 1$ boundaries (i.e., the equivalent to infinite-mass confinement [39])? For a strip along y limited at $x = \pm L/2$ we would have a state

$$\Psi_0(x,y) = \sqrt{\frac{4}{3L}} \begin{bmatrix} 1 \\ \frac{2ix}{L} \end{bmatrix}$$

Therefore, a state that satisfies boundary conditions at all edges can be written as

$$\Psi_0(x,y) = N_0 \left[\left(\frac{L^2}{4} - x^2 \right) \begin{pmatrix} 1 \\ -\frac{2y}{L} \end{pmatrix} + \left(\frac{L^2}{4} - y^2 \right) \begin{pmatrix} 1 \\ \frac{2ix}{L} \end{pmatrix} \right] \tag{4.1.1}$$

States of the form

$$\Psi_0 \mathcal{P}(x,y) \tag{4.1.2}$$

are, by construction, states that satisfy BC.

We need to be careful when treating this enclosure. While the part of the spinor that satisfies the BCs on the $y = \pm\frac{L}{2}$ edges can be acted upon by σ_x to obtain the negative-energy state, the $x = \pm\frac{L}{2}$ part is not quite so simple. If we simply act on it with σ_x, we will be switching the two edges (because if $\frac{\phi_B}{\phi_A} = \pm i$, then $\frac{\phi_A}{\phi_B} = \mp i$). As such, we must generate the corresponding state by also taking the complex conjugate of the initial state, which will not affect the BCs in the y-axis and will fix this issue in the x-axis.

$$\sigma_x \Psi^* \tag{4.1.3}$$

This transformation will leave the boundary conditions intact, and will change $\epsilon \to -\epsilon$ (as seen in Equation 3.1.79). As such, the orthogonalization process will be performed in a cycle given by Equations 4.1.4-4.1.5 (ignoring the normalization step for each of the functions, which

will be done in between each orthogonalization step). Using this sorting method, the Ψ_is with even i will be the positive energy functions, and the odd is will be the negative energy ones. The $\mathcal{P}_i$s are defined as in the Equation 2.2.19, with the only difference of each element of the list appearing twice.

$$\Psi_i = \mathcal{P}_i\Psi_0 - \sum_{j=0}^{i-1}\langle\mathcal{P}_i\Psi_0|\Psi_j\rangle\Psi_j \tag{4.1.4}$$

$$\Psi_{i+1} = \mathcal{P}_{i+1}\left(\sigma_x\Psi_0^*\right) - \sum_{j=0}^{i}\langle\mathcal{P}_{i+1}\left(\sigma_x\Psi_0^*\right)|\Psi_j\rangle\Psi_j \tag{4.1.5}$$

Knowing this, we can obtain the spectrum for different numbers of polynomials, which we display in Figure 4.1.1.

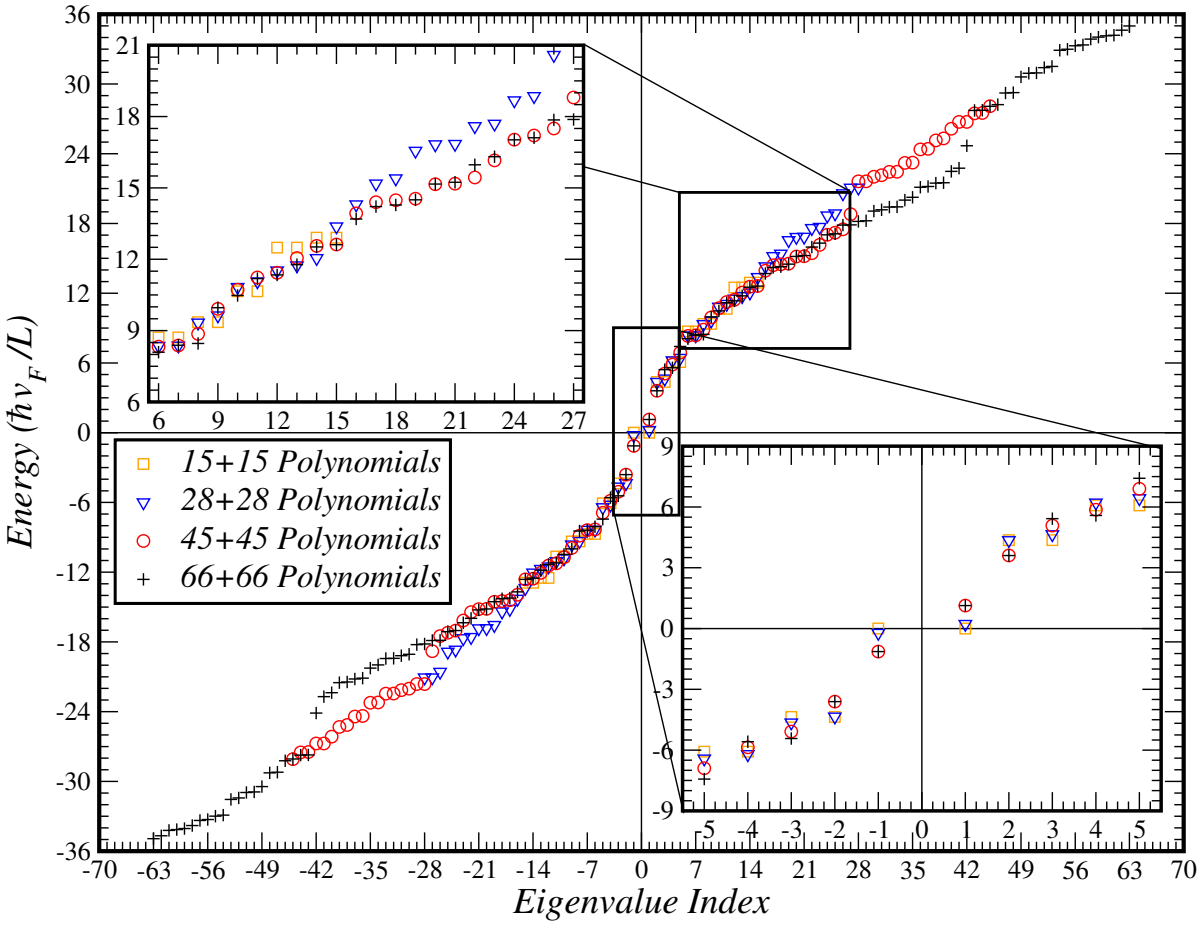

Figure 4.1.1.: Comparison of the spectrum of the uniform-BCs square billiard with increasing number of polynomials.

We will now attempt to treat this problem with the Helmholtz equation, which should be reasonably faster computationally.

4.1.1. Polynomial Method with Helmholtz Equation

As an attempt to accelerate convergence, we will now treat this problem using the Helmholtz equation. Applying the Dirac operator to itself, we obtain the matricial equation

$$\begin{aligned} H^\dagger H\Psi &= -\hbar^2 v_F^2 \left(\overrightarrow{\sigma}\cdot\overrightarrow{p}\right)^\dagger \cdot \left(\overrightarrow{\sigma}\cdot\overrightarrow{p}\right)\Psi \\ &= -\hbar^2 v_F^2 \begin{pmatrix} \partial_x^2+\partial_y^2 & 0 \\ 0 & \partial_x^2+\partial_y^2 \end{pmatrix}\Psi \end{aligned} \tag{4.1.6}$$

As this operator is diagonal, the expected value of the energy (squared) for a state shall be given by the sum of the expected values for both spinor components. I.e.,

$$\langle\Psi_i|\, H^\dagger H\,|\Psi_j\rangle = \langle\psi_{i,A}|\left(-\hbar^2 v_F^2\nabla^2\right)|\psi_{j,A}\rangle + \langle\psi_{i,B}|\left(-\hbar^2 v_F^2\nabla^2\right)|\psi_{j,B}\rangle \tag{4.1.7}$$

Doing this instead of working only with the Dirac Hamiltonian should allow us to increase the basis size further.

The initial polynomials are defined as before (Equation 4.1.1), and we want to study the eigenvalues of $H^\dagger H$ in this basis, which will be positive by definition. Taking the square root of the obtained eigenvalues, we compare these for different numbers of polynomials in Figure 4.1.2.

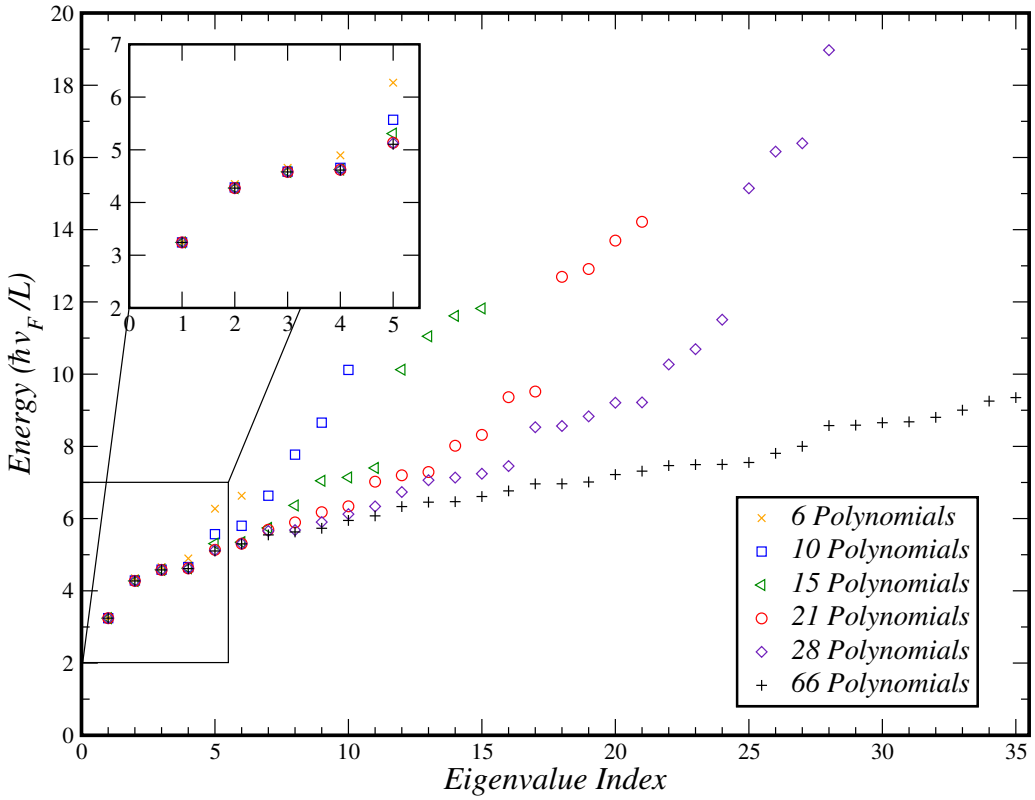

Figure 4.1.2.: Comparison of the square root of the spectrum of the uniform-BCs square billiard with increasing number of polynomials.

The density plots of first three eigenfunctions (left to right, $|\Psi(x,y)|^2 = |\psi_A(x,y)|^2 + |\psi_B(x,y)|^2$, $|\psi_A(x,y)|^2$ and $|\psi_B(x,y)|^2$) of this system are visible in Figure 4.1.3.

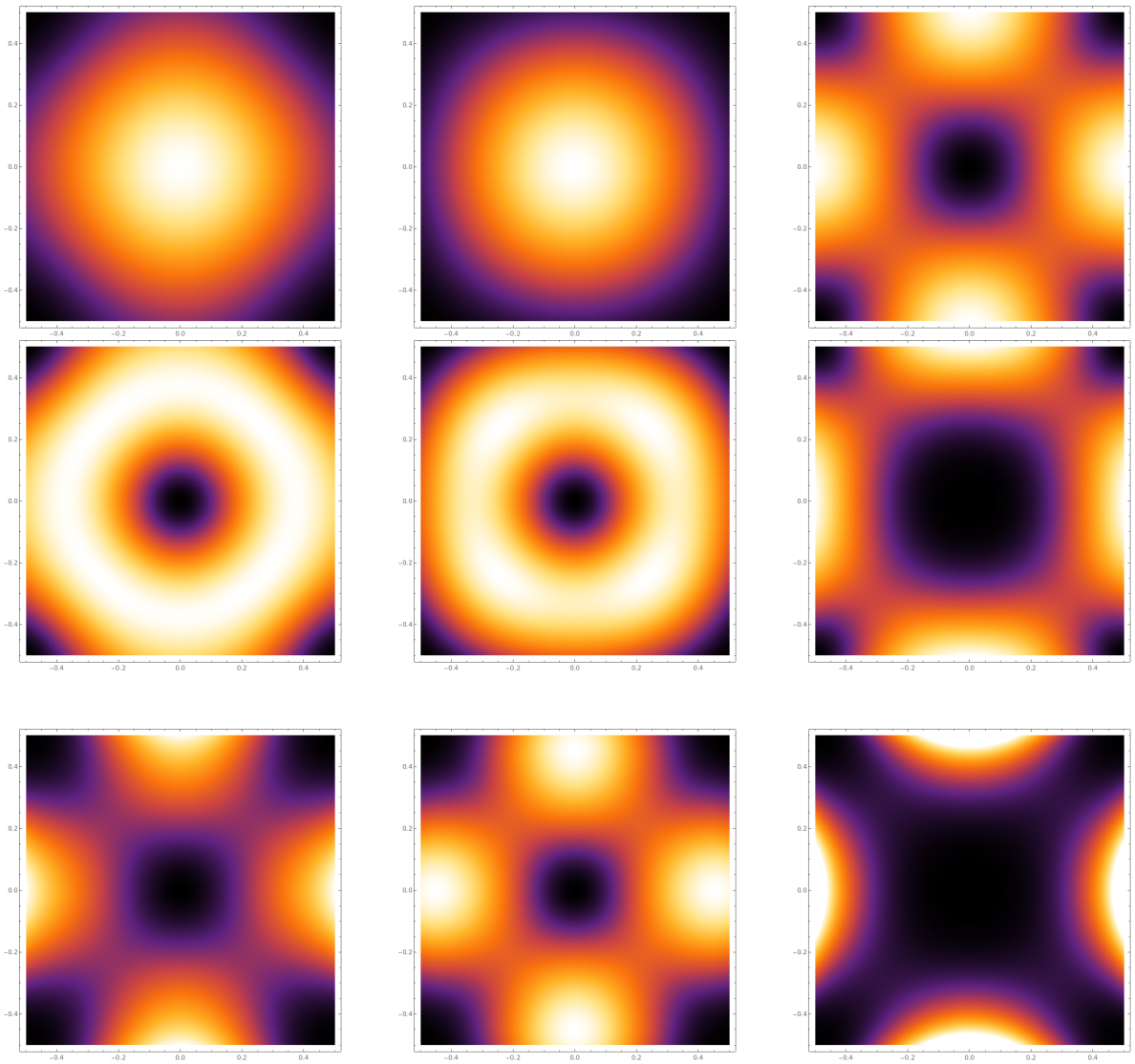

Figure 4.1.3.: Density plots of $|\Psi(x,y)|^2$, $|\psi_A(x,y)|^2$ and $|\psi_B(x,y)|^2$ for the first three energy levels of the infinite-mass confined square.

Additional plots for $|\Psi(x,y)|^2$, $|\psi_A(x,y)|^2$ and $|\psi_B(x,y)|^2$ are available in Appendix B.4.

4.2. Zero-Energy States in 2D

The question remains: are there zero-energy states for the Dirac equation in a polygonal enclosure?

States with exact zero energy are solutions of

$$\begin{aligned} -i\left(\partial_x - i\partial_y\right)\psi_B &= 0 \\ -i\left(\partial_x + i\partial_y\right)\psi_A &= 0 \end{aligned} \tag{4.2.1}$$

These equation can be solved by a change of variables

$$z = x + iy \qquad\qquad \bar{z} = x - iy$$

which means that

$$\begin{aligned} \partial_x &= \frac{\partial z}{\partial x}\partial_z + \frac{\partial \bar{z}}{\partial x}\partial_{\bar{z}} = \partial_z + \partial_{\bar{z}} \\ \partial_y &= \frac{\partial z}{\partial y}\partial_z + \frac{\partial \bar{z}}{\partial y}\partial_{\bar{z}} = i\left(\partial_z - \partial_{\bar{z}}\right) \end{aligned}$$

Adding and subtracting the two together, we obtain

$$\begin{aligned} \left(\partial_x - i\partial_y\right) &= 2\partial_z \\ \left(\partial_x + i\partial_y\right) &= 2\partial_{\bar{z}} \end{aligned} \tag{4.2.2}$$

In these coordinates, the zero energy condition becomes

$$\begin{aligned} \partial_z \psi_B &= 0 \\ \partial_{\bar{z}} \psi_A &= 0 \end{aligned} \tag{4.2.3}$$

The general solution to these equations is simply

$$\begin{aligned} \psi_B &= f\left(\bar{z}\right) = f\left(x - iy\right) \\ \psi_A &= g\left(z\right) = g\left(x + iy\right) \end{aligned} \tag{4.2.4}$$

So the general solution for zero-energy states is

$$\Psi\left(x, y\right) = \begin{bmatrix} g\left(x + iy\right) \\ f\left(x - iy\right) \end{bmatrix} \tag{4.2.5}$$

As one cannot define a non-trivial function of only z (or $\bar{z}$) that is zero along a straight line, it appears that boundary conditions can almost never be satisfied with this choice of ket. Consequently, no zero-energy states are possible using the Dirac-Weyl equation in a polygonal enclosure, except in a very specific case. This situation was discussed in Section 3.3.1, and is specific of the problem where $t = 0$ (or $t = \infty$) in all the boundaries.

A more specific example of impossibility of finding these states with different boundary conditions will be presented in the next subsection.

4.2.1. Zero-Energy States in a Square with Uniform Boundary Conditions $t = 1$

As seen previously, a zero-energy state has the form

$$\Psi(x,y) = \begin{bmatrix} g(x+iy) \\ f(x-iy) \end{bmatrix} \tag{4.2.6}$$

Assuming that f, g have no singularities in the desired domain, one can expand them in a polynomial series

$$\begin{aligned} f(x-iy) &= \sum_n f_n (x-iy)^n \\ g(x+iy) &= \sum_n g_n (x+iy)^n \end{aligned} \tag{4.2.7}$$

Re-defining (for simplicity) the square as having sides $y \in [0,1]$, $x \in [0,1]$, we first consider the side with $y = 0$. The imposed boundary condition ($t = 1$) will require

$$f(x) = g(x)$$

or, considering the expansion of f, g,

$$\sum_n f_n x^n = \sum_n g_n x^n \tag{4.2.8}$$

As we are dealing with a finite range of x, this implies

$$f_n = g_n \tag{4.2.9}$$

Therefore,

$$\frac{\psi_B}{\psi_A} = \frac{f(x-iy)}{f(x+iy)} \tag{4.2.10}$$

On the west side ($x = 0$, $y \in [0,1]$) the imposed boundary condition will be

$$\frac{\psi_B}{\psi_A} = -i$$

Therefore,

$$\sum_n f_n (-iy)^n = -i \sum_n f_n (iy)^n \tag{4.2.11}$$

Rearranging the terms,

$$\sum_n \left[(-i)^n + i^{n+1}\right] f_n y^n = 0$$

Multiplying by i^n, we obtain

$$\sum_n \left[1 + i^{2n+1}\right] f_n y^n = \sum_n \left[1 + i(-1)^n\right] f_n y^n = 0 \tag{4.2.12}$$

This is only possible if $f_n = 0$. The only zero-energy state is the state with zero wave-function.

5. Hexagonal Graphene Flake with Zigzag-like Boundaries

In this final chapter, we begin by numerically integrating the Helmholtz equation with the specific boundary conditions in question. After that, we discuss the origin of exactly-zero energy states in tight-binding, as well as the size-dependence of the spectrum in a continuum model. We compare these results against the ones found by Zarenia *et al* [25], and discuss the validity of the authors' results.

Finally, we attempt to apply our method to the continuum-analogous of an hexagonal graphene flake with zigzag boundary conditions. We utilize both the Dirac and the Helmholtz equation, obtaining the spectrum and the lowest-energy eigenfunctions. We finally compare the obtained spectrum and eigenfunctions to those from both the exact and polynomial approximation of the triangular enclosure, observing an apparent equivalence between the two.

5.1. Eigenvalue Calculation through Partial Differential Equation Numerical Integration

Starting from the Dirac-Weyl equation, we manipulate it to obtain (again)

$$-\left(\partial_x^2+\partial_y^2\right)\varphi_A=\epsilon^2\varphi_A \qquad\qquad -\left(\partial_x^2+\partial_y^2\right)\varphi_B=\epsilon^2\varphi_B \tag{5.1.1}$$

As we know the boundary conditions for this kind of quantum dot, we can work on finding the energy levels.

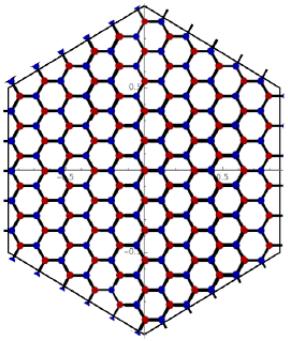

Figure 5.1.1.: Hexagonal graphene flake with zigzag boundary conditions.

From Figure 5.1.1, and defining the red/blue dots as the A/B sub-lattices, respectively, we can insert the eigenvalue problem into a numerical integrator (*Wolfram Mathematica*®, for example). It is important to note that, in each boundary, not only are the termination wave-

functions zero, but also the derivatives of the other sub-lattice points' wave functions, i.e., in one of the A-terminated edges, we have the boundary conditions

$$\varphi_A = 0 \qquad\qquad -i\left[\partial_{x'} - i\partial_{y'}\right]\varphi_B = 0 \tag{5.1.2}$$

Plotting the first 256 energy eigenvalues, we obtain Figure 5.1.2, where negative eigenvalue indexes are used to represent the states of negative energy.

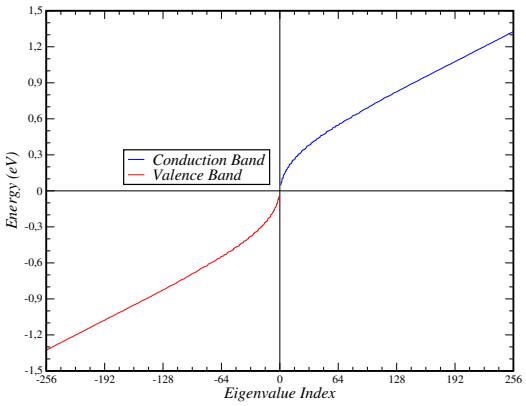

Figure 5.1.2.: First 256 energy levels.

We now want to compare these energy levels against the ones obtained from a tight-binding model. Building an hexagonal graphene dot with Pybinding [44] is quite simple, taking only 5-6 lines of codes. After that, we use exact diagonalization of the Hamiltonian to calculate the energy levels. To increase the number of graphene lattices and, consequently, the accuracy of the energy eigenvalues, we use a very large hexagonal enclosure ($\sim$ 1000 graphene lattices). Plotting the two together, we obtain Figure 5.1.3.

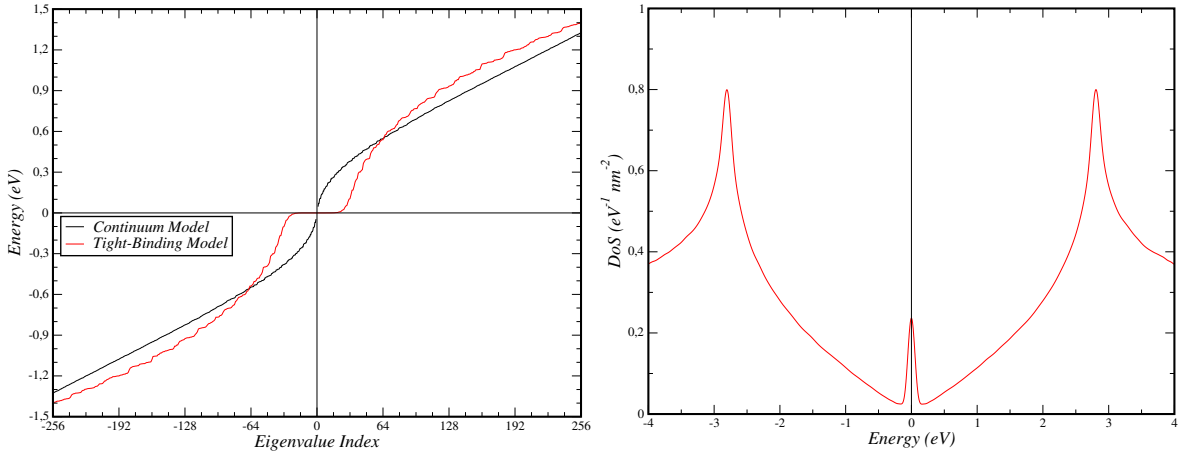

Figure 5.1.3.: (Left) Energies of an hexagonal graphene dot with zigzag-like boundaries. (Right) Tight-binding density of states.

As we can see, there is a clear difference between the two, as we do not obtain the flat region at zero-energy for the continuum Hamiltonian. For the energies obtained from the tight-binding Hamiltonian, we obtain the density of states in the right-hand side using KPM [45]. This density of states is the one we expected, with the Dirac peak formed due to the flat spectrum.

We will now attempt to use our polynomial method to treat this problem by taking into account the treatment for the boundary conditions developed in Section 3.1.3.2.

5.1.1. Exactly-Zero Energy States in Tight-Binding

In tight-binding there are states of exactly zero energy. This is due to an asymmetry in the sub-lattices, created when one cuts the graphene sheet into the desired polygonal flake. The asymmetry created translates into a difference in the number of A and B sub-lattices. This is more clearly seen in the edges of Figure 5.1.4. There is a total of 3×6 red sites in the boundary, while the blue sites in the edge only sum to 3×5. The exact amount of sites in each sub-lattice will depend linearly on the boundary length (i.e., on the size of the polygon). How does this create states of exactly zero energy?

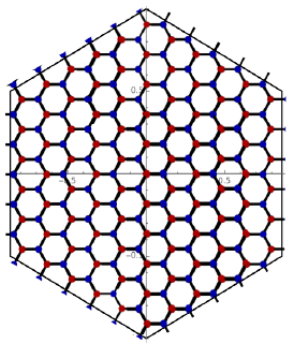

Figure 5.1.4.: Hexagonal graphene flake with zigzag boundary conditions.

The wave functions of each sub-lattice form a basis of linearly-independent vectors, where the number of elements of this basis is the number of sites for the particular sub-lattice in question. The Hamiltonian is a linear operator that transforms states of the A sub-lattice into states of the B sub-lattice, which means that it must transform each of the basis vectors of one of the basis into a vector of the other. This is where the zero energy states come from: if a linear operator applied on m linearly independent vectors transforms them into n linearly independent vectors, with $n < m$, then the difference of dimensions must be the same as the kernel of the transformation. This is clearly observable in the article by Potasz *et al* [46], where the authors find 4 states of exactly zero energy and the difference in sub-lattices is also exactly 4. As the authors claim, one can control the amount of zero energy states by changing the system size.

When one takes the continuum limit to obtain the Dirac-Weyl equation for the movement of electrons in graphene, the only remaining length scale will be the $\frac{1}{L}$ dependence in the value of each energy levels. This is a mere re-scaling of the energy units, which does not change the overall shape of the curves. The number of states will not change with the system size,

by contrast with tight-binding where the number of states is completely determined by the system size. The spectrum in a continuum model will behave as

$$E = f\left(n_1, n_2, ...\right) \frac{\hbar v_F}{L} \tag{5.1.3}$$

where $n_1, n_2, ...$ are the quantum numbers that govern the system (exactly what Gaddah found in Equation 3.2.3).

5.1.2. Zarenia's Results – a Critique

Knowing this, why do the features of the curves for the continuum model obtained by Zarenia *et al* [25] (Figure 5.1.5) change when the system size is increased?

The authors observe a scaling of the number of energy levels with N_s, which is defined as being the number of atoms in each side of the dot, and is using to obtain the length L of the sides of the dot (Equation 5.1.4).

$$L = \sqrt{3}\left(N_s + 1\right) a \tag{5.1.4}$$

where a is the lattice parameter of graphene. As we discussed previously, the number of states in continuum model is fixed, and therefore does not depend on the system size. Zarenia, however, finds two unexpected phenomena: firstly, the authors find states of exactly-zero energy; secondly, the number of states increases with N_s and, therefore, with L. Neither of these behaviors should happen, as observed in our numerical integration (Figure 5.1.2).

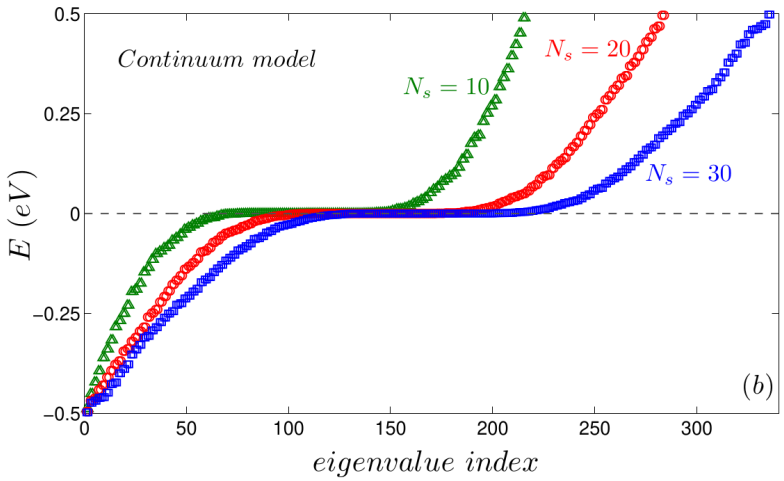

Figure 5.1.5.: Continuum spectrum of a zigzag-like hexagonal graphene flake as obtained by Zarenia *et al* [25].

As their numerical calculations were performed with *COMSOL*® by discretizing the region through a mesh to perform integration by finite-elements, a new length scale was introduced into the problem: the ratio between the mesh and the system size. This mesh acted as a pseudo-lattice, with a number of sites (and therefore states) increasing as the system size increased. This what introduced the size dependence on the number of states obtained.

5.2. Applying the Polynomial Method

For us to employ the polynomial method discussed in Section 3.1, we must first discuss the boundary conditions necessary to take into account when building the first polynomial.

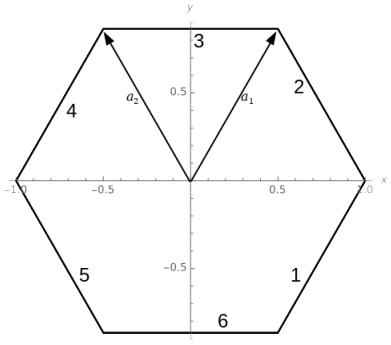

Figure 5.2.1.: Basis vectors and identification of the edges.

Employing the formula (Equation 3.1.32) for the rotated edge j (still in Cartesian coordinates)

$$\left(\frac{\phi_B}{\phi_A}\right)_j = te^{i\alpha_j} \tag{5.2.1}$$

we have to apply it to the three edges

$$y = \sqrt{3}x \pm \sqrt{3}L \qquad y = \pm\frac{\sqrt{3}}{2}L \qquad y = -\sqrt{3}x \pm \sqrt{3}L \tag{5.2.2}$$

It is important to note that the pairs of opposing edges are not equivalent: in one, $t = 0$; in the other, $t = \infty$. In Cartesian coordinates, therefore, the first polynomial will be given by

$$\Psi_0(x,y) = N_0 \left\{ \begin{bmatrix} \frac{\sqrt{3}L}{2} + y \\ \frac{\sqrt{3}L}{2} - y \end{bmatrix} \begin{bmatrix} L + \left(x - \frac{y}{\sqrt{3}}\right) \\ L - \left(x - \frac{y}{\sqrt{3}}\right) \end{bmatrix} \begin{bmatrix} L - \left(x + \frac{y}{\sqrt{3}}\right) \\ L + \left(x + \frac{y}{\sqrt{3}}\right) \end{bmatrix} \right\} \tag{5.2.3}$$

and the integration region will be

$$\iint_A dxdy \to \int_{-\frac{\sqrt{3}L}{2}}^{\frac{\sqrt{3}L}{2}} dy \int_{-L+\frac{|y|}{\sqrt{3}}}^{L-\frac{|y|}{\sqrt{3}}} dx$$

Knowing this, we can obtain an approximation to the low-energy spectrum by taking the eigenvalues of the Hamiltonian matrix

$$H_{ij} = -i \int_{-\frac{\sqrt{3}L}{2}}^{\frac{\sqrt{3}L}{2}} dy \int_{-L+\frac{|y|}{\sqrt{3}}}^{L-\frac{|y|}{\sqrt{3}}} dx \Psi_i^\dagger \left(\sigma^x \partial_x + \sigma^y \partial_y\right) \Psi_j \tag{5.2.4}$$

The negative-energy polynomials will be obtained as was in the case in the 1D non-uniform BCs (Equation 3.1.83). We can finally create the set of basis function that we will use through

Gram-Schmidt Orthogonalization by taking two cycles according to Equations 5.2.5-5.2.6

$$\Psi_i = \mathcal{P}_i\Psi_0 - \sum_{j=0}^{i-1}\langle\mathcal{P}_i\Psi_0|\Psi_j\rangle\Psi_j \tag{5.2.5}$$

$$\Psi_{i+1} = \mathcal{P}_{i+1}\left(\sigma_z\Psi_0\right) - \sum_{j=0}^{i}\langle\mathcal{P}_{i+1}\left(\sigma_z\Psi_0\right)|\Psi_j\rangle\Psi_j \tag{5.2.6}$$

where $\mathcal{P}_i$ is defined in the same way as in the Schrödinger problem (Equation 2.2.19), with the only difference of each element of the list appearing twice (exactly the same as in the Dirac square-billiards problem).

Afterwards, we diagonalize the Hamiltonian matrix and obtain the spectrum of this regime for several different numbers of polynomials, visible in Figure 5.2.2.

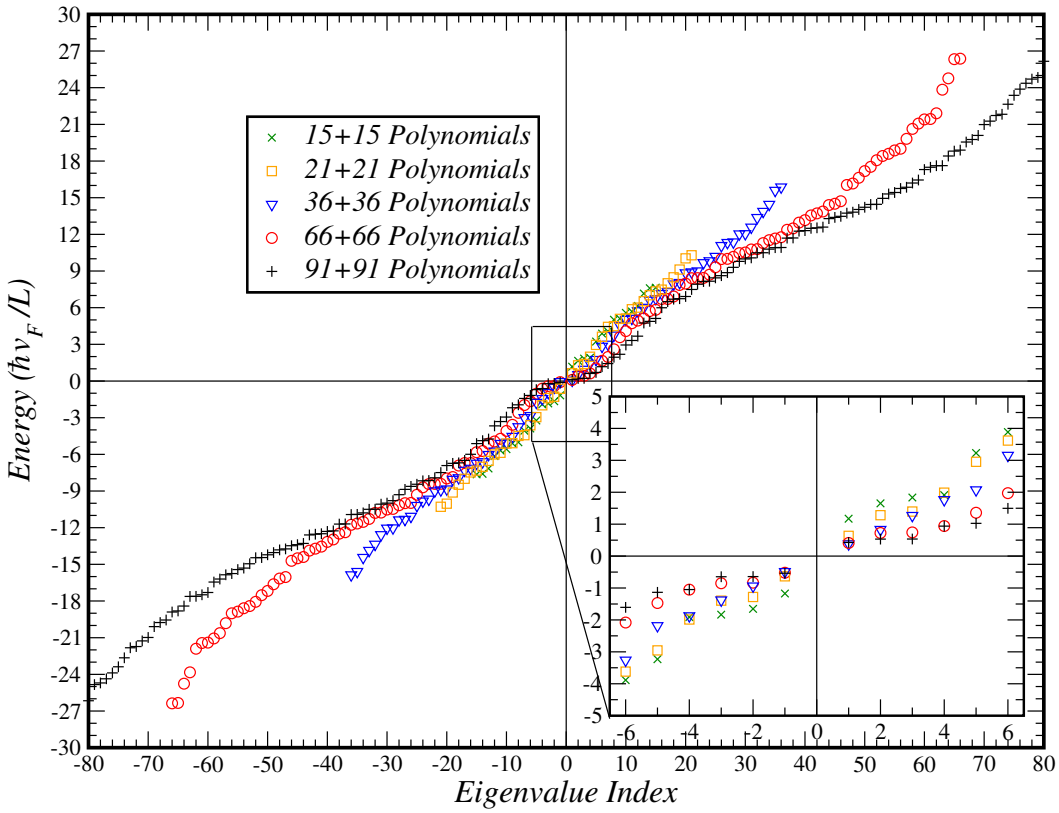

Figure 5.2.2.: Evolution of the spectrum of the zigzag-like-BCs hexagonal graphene dot with different numbers of polynomials.

These curves appear to be converging, although very slowly. This is observable in the behaviour of the 36×2, 66×2, and 91×2 curves, where the lowest eigenvalue appears to already have converged. The two next eigenvalues also appear to be following this trend (66×2 and 91×2 spectra), although an increase in polynomial number would be required to analyze this further. As such, we will now attempt to treat this problem as an Helmholtz problem.

5.3. Polynomial Method with Helmholtz Equation for the Hexagonal Graphene Flake

In this section, the treatment performed in Section 4.1.1 will be replicated for the case of the hexagonal graphene flake with zigzag-like edges, as an attempt to use a larger number of polynomials. In principle, the obtained solution will be the same as the one we arrived at for the case of the triangular enclosure. This is because the imposed boundary conditions are equivalent to Dirichlet boundary conditions in two larger triangles for each spinor element.

As an example, ψ_A will be zero in the three edges of the hexagon defined by

$$y = -\frac{\sqrt{3}L}{2}, \qquad y = \sqrt{3}\,(x + L)\,, \qquad y = \sqrt{3}\,(-x + L)$$

which means that it will also be zero in the larger triangle defined by these same edges. Visually this translates to Figure 5.3.1, where the dashed edges of the hexagon are those where ψ_A is "free". An identical behaviour for ψ_B is visible in this same figure, which results in the same larger triangle but now inverted in the y-axis. As such, the convergence of the eigenvalues of

$$E_{A\,i,j} = \langle \psi_{i,A} | \left(-\hbar^2 v_F^2 \nabla^2\right) | \psi_{j,A} \rangle \qquad E_{B\,i,j} = \langle \psi_{i,B} | \left(-\hbar^2 v_F^2 \nabla^2\right) | \psi_{j,B} \rangle \tag{5.3.1}$$

will be immediate.

It is important to note that we will need to scale the energies according to the areas of the two polygons, as the triangle will have 1.5 times the area of the original hexagon.

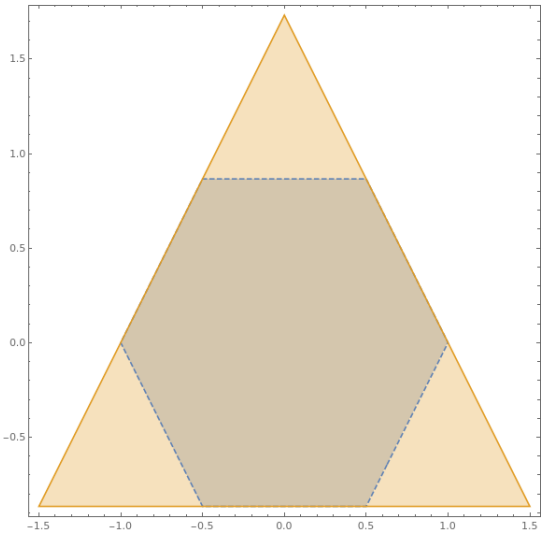

Figure 5.3.1.: Boundary conditions for ψ_A will be equivalent between the hexagon and the larger triangle.

The procedure will be exactly the same as in Section 4.1.1. Defining the initial polynomial as before (Equation 5.2.3), we want to study the eigenvalues of $H^\dagger H$ in this basis, which will be positive by definition. Taking the square root of the obtained eigenvalues, we compare these for different numbers of polynomials in Figure 5.3.2, as well as against the numerical

eigenvalues obtained in Section 5.1. Comparing the non-diverging eigenvalues (with a scaling factor of $\sqrt{\frac{A_{\text{hex}}}{A_{\text{triang}}}}$ due to the different system sizes) against the results obtained for the triangle using Helmholtz equation (Section 3.3), we obtain Figure 5.3.3.

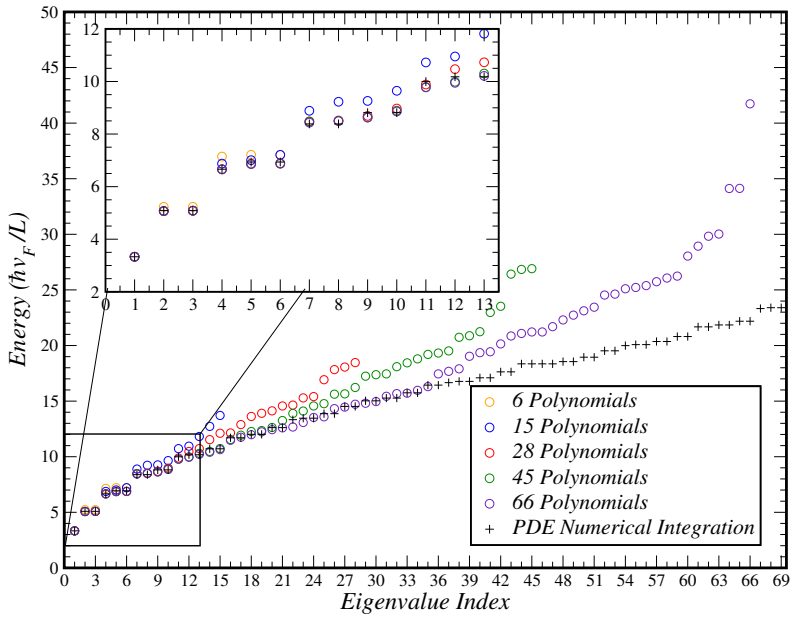

Figure 5.3.2.: Comparison of the spectrum of the zigzag-like BCs hexagonal billiard with increasing number of polynomials.

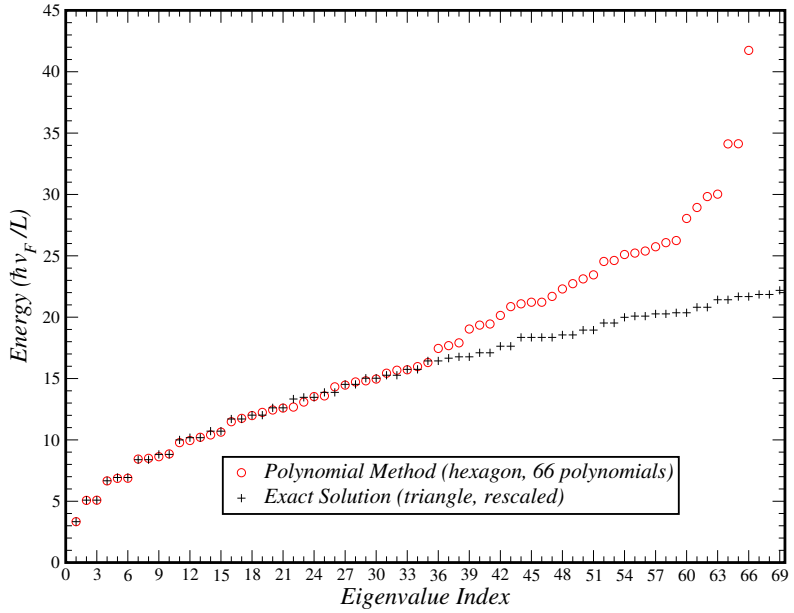

Figure 5.3.3.: Comparison of the spectrum of the zigzag-like-BCs hexagonal billiard against the exact solution for the triangle.

As a final note, we compare (Figure 5.3.4) the density plots of first three positive energy eigenfunctions (only the ψ_A component, as the ψ_B is simply an inversion) of the hexagon with the ones obtained previously for the triangle (Section 3.3), highlighting the corresponding region. Additional plots for $|\Psi(x,y)|^2$, $|\psi_A(x,y)|^2$ and $|\psi_B(x,y)|^2$ are available in Appendix B.5.

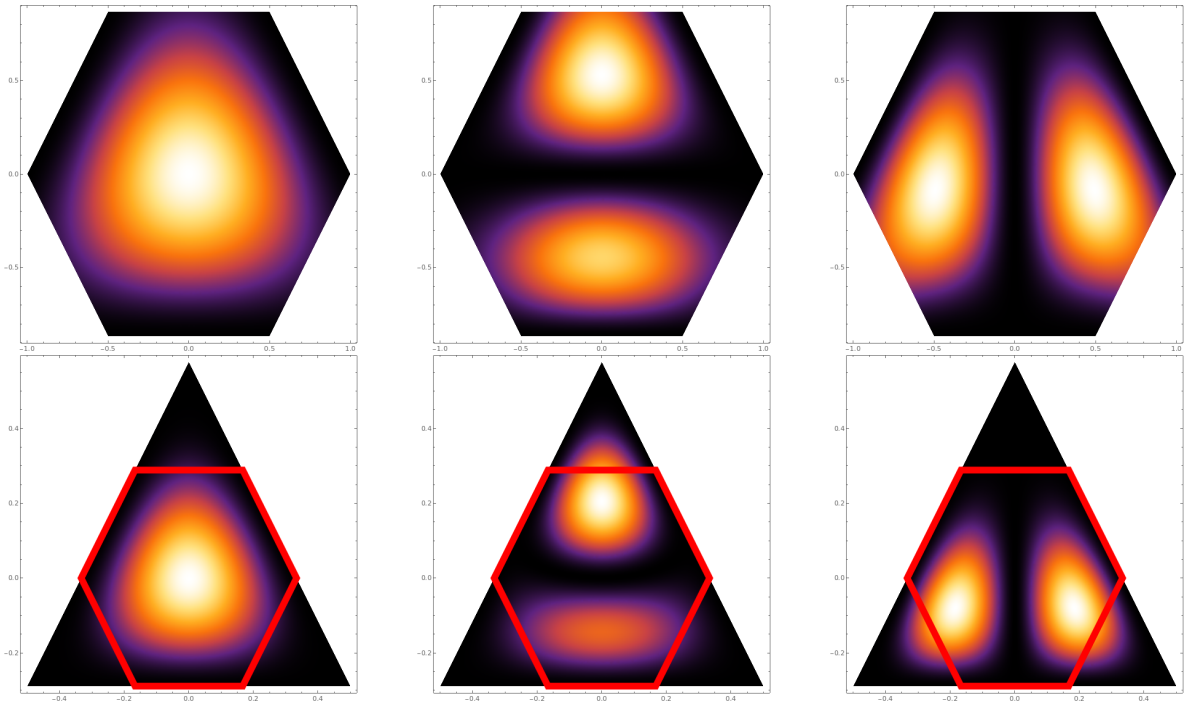

Figure 5.3.4.: $|\psi_{A,j}|^2$ for the hexagon (top) and for the triangle (bottom) $j \in \{1,2,3\}$.

Further analysis of this hexagon-triangle symmetry will be necessary to check if it is possible to use a modified version of the exact solutions for the triangle to write the exact solutions for the zigzag-like hexagon.

6. Conclusions and Future Work

Throughout this thesis, we worked on the generalization of a polynomial method so that we were able to study the spectrum of hexagonal regions of twisted bilayer using a continuum model. This polynomial method reproduced with remarkable precision the exact and numerical results for the Schrödinger problems.

When it came to the generalization for the case of Dirac's equation, we hit a roadblock regarding the imposing of boundary conditions. As such, the study of relativistic systems was delayed and, ultimately, we were unable to apply this method to bilayer graphene systems. After generalizing the polynomial method, we replicated two exact solutions for 1-dimensional systems, as well as studying a third 1D problem which presented an easily-obtainable zero-energy solution.

The straightforward generalization of this method to bidimensional problems worked. We were able to study a square with infinite-mass confinement boundary conditions, as well as a triangle and an hexagon with zigzag-like boundaries. The obtained solutions for the hexagon presented an apparent equivalence with the ones for the triangle, for which an analytical solution existed in the literature.

The agreement with the known solutions from the existing literature was very satisfactory, but we would like to find a way to optimize this process. The computation time of both the Gram-Schmidt process and the Hamiltonian matrix elements grew quite rapidly, which stopped us from increasing the basis size past a certain amount.

A solution to the ever-increasing computation time could be to re-write the code utilized into a more low-level programming language, such as Python or C/C++, instead of utilizing *Wolfram Mathematica*® to perform numerical calculations.

For the future, we hope to further generalize this approach, first to AA- and AB-stacked bilayer graphene systems, and then finally for twisted bilayer graphene. To do this, we will need to study the necessary boundary conditions for confined states in these systems. Another point that will require further study will be the zero-energy states, and their meaning in this continuum approach.

Additionally, there is no *a priori* reason that prevents us from studying different properties of the systems we utilized. For example, optical response or the effects of a magnetic field.

A. Appendix

A.1. Plots of $\psi_i(x, y)$ with $i \in [1, 8]$ for the Square Enclosure

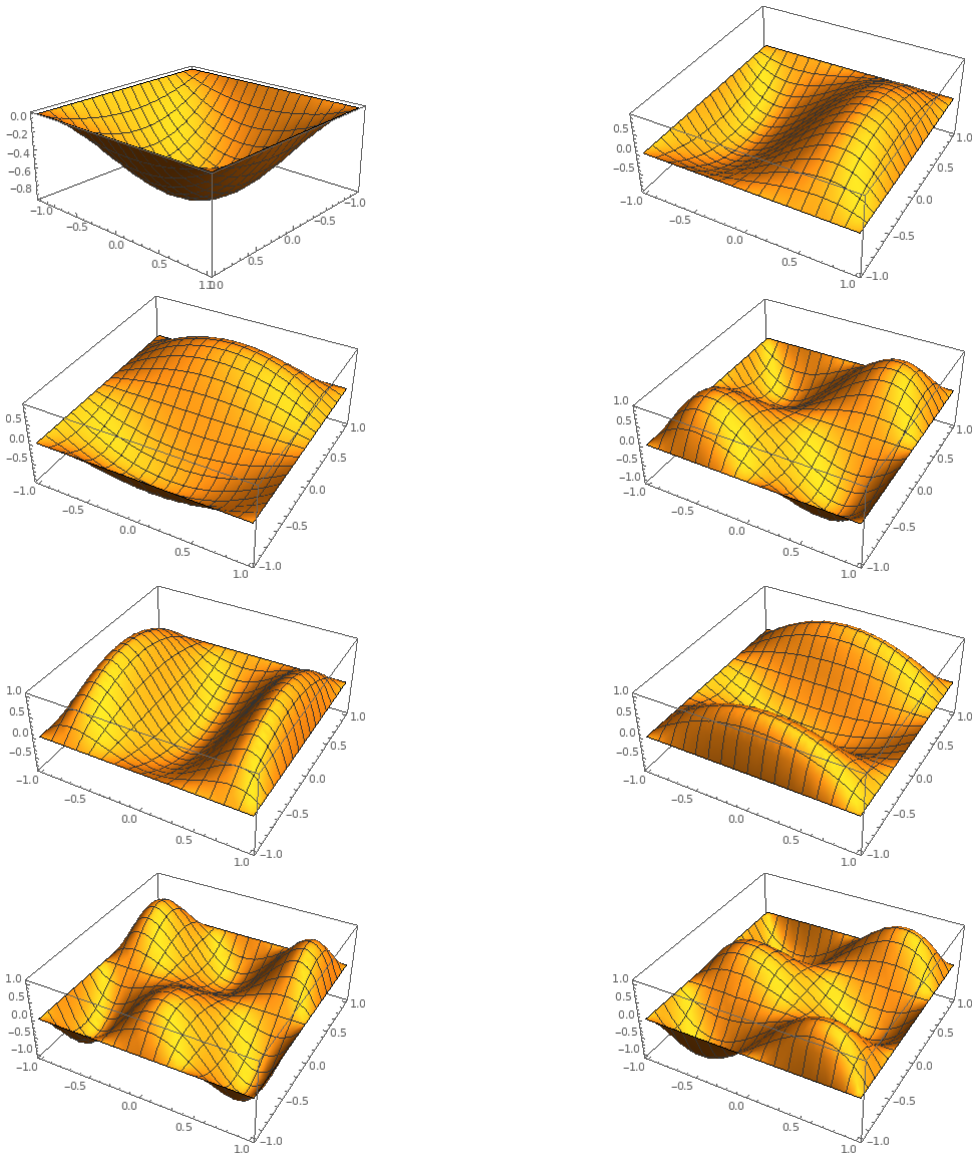

Figure A.1.1.: Left to right, top to bottom: $\psi_i(x, y)$ with $i \in [1, 8]$.

A.2. Block Diagonalization of the Hamiltonian Matrix

For a system governed by the Schrödinger equation, the symmetries of the Hamiltonian will be obtained from the symmetries of the specific potential profile. In the problems we consider, this profile will define specific regular polygons, which will redirect us to the point-group that characterizes this polygon.

Therefore, the most obvious and sensible way for us to generate higher-order polynomials in by taking into account the different irreducible representations of the point-group in question. What we want to demonstrate is the orthogonality between functions belonging to different irreducible representations. This orthogonality will ensure that the Hamiltonian matrix will be diagonal in blocks, which significantly reduces the computation time. This section heavily relies on the group theory book by Dresselhaus *et al*[47].

As the product of two different irreducible representations is, by definition, zero, what we need to show is that both the Laplacian and the initial polynomial belong to the identity representation (usually denominated A_1). The Laplacian will affect only the calculation of the Hamiltonian matrix elements, while the starting polynomial ψ_0 will enter in both the Hamiltonian matrix elements and the Gram-Schmidt process.

The Laplacian is a scalar operator invariant under any rotation or reflection, and therefore invariant under any operation of the point group in question. Therefore, it transforms according to the A_1 representation.

For the initial polynomial ψ_0, we only need to note that it is zero in all the edges (i.e., obeys the imposed Dirichlet boundary conditions). Because of this, and as the action of each of the elements of the group can be seen as an exchange of boundaries, we know that ψ_0 must belong to the identity representation. As an example for clarity, for the square infinite potential well,

$$\begin{aligned}\psi_0(x,y) &= \left(L^2-x^2\right)\left(L^2-y^2\right)\\ &= L^4 - L^2\left(x^2+y^2\right)+x^2y^2\\ &= -L^2\left(x^2+y^2\right)+x^2y^2+\text{const}\end{aligned} \tag{A.2.1}$$

The first term in Equation A.2.1 is the distance element, which immediately belongs to the identity representation. The second term is invariant under any $\pm\frac{\pi}{2}$ rotation, as well as under any $x \to -x$, $y \to -y$ or $x, y \to \pm y, x$ reflection, which means that it also belongs to the identity representation. This was shown for the case of the square enclosure, but is easily extended to any regular polygonal enclosure.

By direct application of Schur's Lemma[48], we know that the scalar product of functions belonging to irreducible representations F, G will only be non-zero if $F \otimes G$ contains the identity representation, which only happens if $F = G$.

As such, and by direct application of each of these facts, we know that a function generated by the product of a polynomial belonging to any of the irreducible representations (generically denoted as R) will only have non-zero projections upon functions that belong to that same representation (i.e., the Gram-Schmidt process will not mix functions of different irreducible representations). Applying this same fact to the different matrix entries of the Hamiltonian,

$$H_{ij} = -\iint_{\Omega} dxdy\, \psi_i \nabla^2 \psi_j \tag{A.2.2}$$

we can see that, denoting F, G as the irreducible representations containing $\psi_{i,j}$, respectively, (in the following, $\sim$ means "belongs to")

$$\begin{aligned} \psi_i \nabla^2 \psi_j &\sim F \otimes A_1 \otimes G \\ &\sim F \otimes G \end{aligned} \tag{A.2.3}$$

From this, we know that $\psi_i \nabla^2 \psi_j \sim F \otimes G$ only contains the A_1 irreducible representation if (and only if) $F = G$. This means that the integral in Equation A.2.2 will only be non-zero when $F = G$ (again, by Schur's Lemma). As such, this guarantees that the Hamiltonian matrix will be diagonal by blocks, which is exactly what we wanted to show. ■

A.3. Plots of $\psi_i(x, y)$ with $i \in [1, 8]$ for the Hexagonal Enclosure

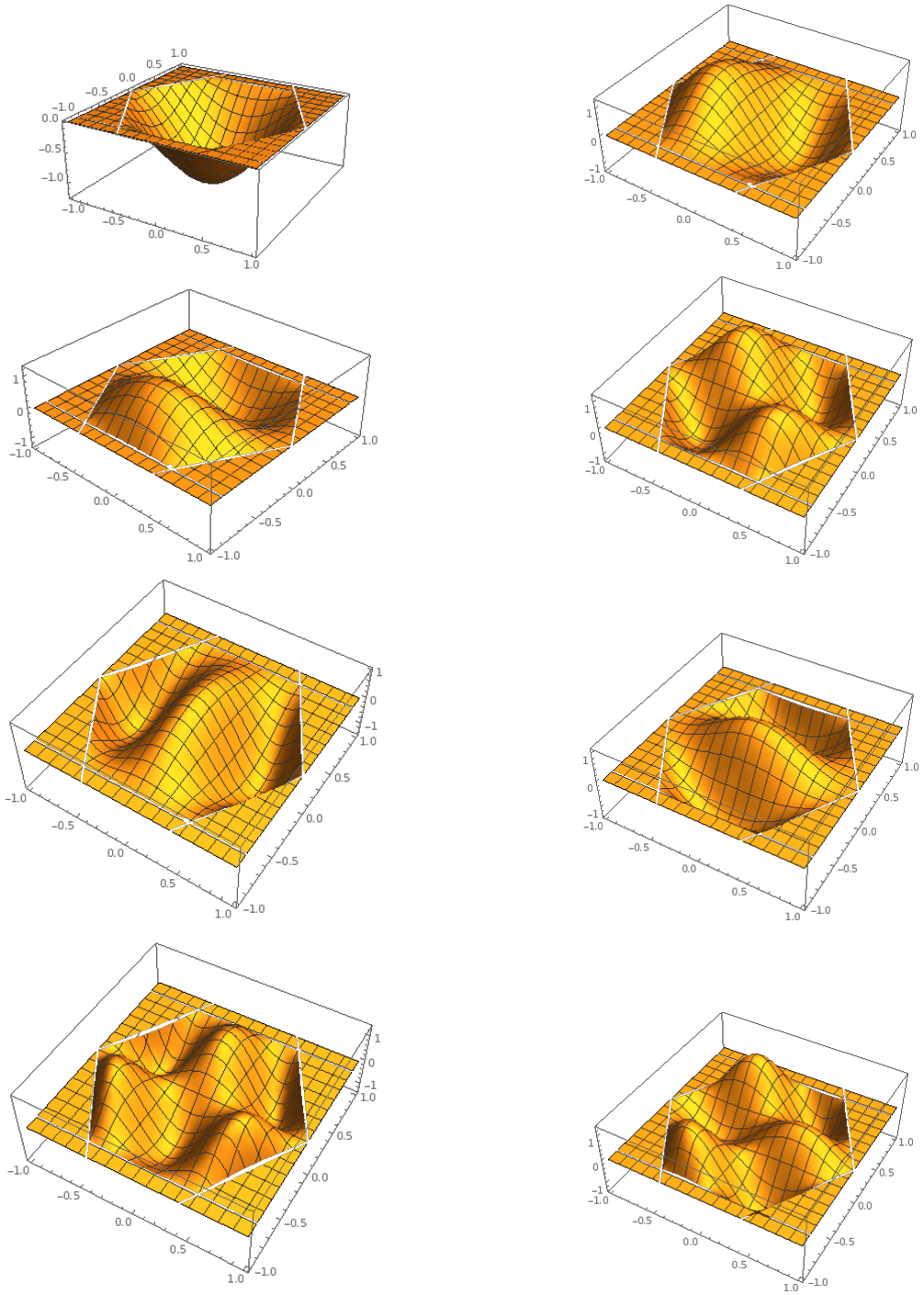

Figure A.3.1.: Left to right, top to bottom: $\psi_i(x, y)$ with $i \in [1, 8]$.

A.4. C_{6v} Group Symmetry Treatment of the Hexagonal Enclosure

The C_{6v} group has 12 elements, and its character table is reproduced in Table A.4.1.

C_{6v} (6mm)	E	$2C_6$	$2C_3$	C_2	$3\sigma_v$	$3\sigma_d$		
A_1	1	1	1	1	1	1	z	x^2+y^2, z^2
A_2	1	1	1	1	−1	−1	R_z	
B_1	1	−1	1	−1	1	−1		
B_2	1	−1	1	−1	−1	1		
E_1	2	1	−1	−2	0	0	$(x, y)(R_x, R_y)$	(xz, yz)
E_2	2	−1	−1	2	0	0		$(x^2-y^2, 2xy)$

Figure A.4.1.: Character table of C_{6v}.

Here, C_6 denotes rotations of $\pm\frac{\pi}{3}$, $C_3 = C_6^2$, $C_2 = C_6^4$; σ_v are the reflections on the three axis that pass through the vertices, and σ_d are the reflections on the three axis that pass through the faces. Defining the lowest order polynomial (that is zero on all boundaries) as

$$\tilde{\phi}_0(x,y) = \left(\frac{3}{4} - y^2\right)\left(1 - \left(x - \frac{y}{\sqrt{3}}\right)^2\right)\left(1 - \left(x + \frac{y}{\sqrt{3}}\right)^2\right) \tag{A.4.1}$$

where the tilde ($\tilde{}$) identifies an un-normalized function, we know that it belongs to the A_1 representation (shown in Equation 2.4.21). As such, the product of a function f belonging to the irreducible representation X with this polynomial will also belong to the irreducible representation X.

Analogously to the treatment for the C_{4v} point-group, the higher order polynomials will be obtained by multiplication with a set of polynomials $f_{n,i}(x,y)$ that form irreducible representations of C_{6v}.

Trivially, for $n = 0$ the only possible f is

$$f_0 = 1 \tag{A.4.2}$$

which belongs to A_1.

For $n = 1$, there are only 2 possible first-degree polynomials. As we want them to be orthogonal, we write

$$\begin{aligned} f_{1,1} &= x + y \\ f_{1,2} &= x - y \end{aligned} \tag{A.4.3}$$

which are elements of the irreducible representation E_1. From this point on, we will require the direct product table for this symmetry group (Table A.4.2).

	A_1	A_2	B_1	B_2	E_1	E_2
A_1	A_1	A_2	B_1	B_2	E_1	E_2
A_2		A_1	B_2	B_1	E_1	E_2
B_1			A_1	A_2	E_2	E_1
B_2				A_1	E_2	E_1
E_1					$A_1 + [A_2] + E_2$	$B_1 + B_2 + E_1$
E_2						$A_1 + [A_2] + E_2$

Figure A.4.2.: Direct product table for C_{6v}.

For $n = 2$, we have to be more careful than in the case of the C_{4v} group. Taking the direct product, we get

$$E_1 \otimes E_1 = A_1 \oplus A_2 \oplus E_2 \tag{A.4.4}$$

and we will have three polynomials. As the E_2 irreducible representation is bi-dimensional and the A_is are one-dimensional, one of the elements must be ignored due to the symmetries of the shape in question. By direct product of the $f_{1,i}$s, we have three polynomials

$$\begin{aligned} f_{1,1} \times f_{1,1} &= x^2 + y^2 + 2xy \\ f_{1,1} \times f_{1,2} = f_{1,2} \times f_{1,1} &= x^2 - y^2 \\ f_{1,2} \times f_{1,2} &= x^2 + y^2 - 2xy \end{aligned} \tag{A.4.5}$$

Reorganizing these equations so that they are invariant under the action of each of the irreducible representations, we have

$$\begin{aligned} f_{2,1} &= x^2 + y^2 + xy \\ f_{2,2} &= x^2 + y^2 + 4xy \\ f_{2,3} &= x^2 - y^2 \end{aligned} \tag{A.4.6}$$

again, these expressions were not yet normalized, but they are already orthogonal amongst themselves. In what irreducible representation do each of them fall into? Obviously, $f_{2,1}$ must be in A_1 since it is the invariant distance in this space. We now need to classify $f_{2,2}$ and $f_{2,3}$. They must belong to E_2, as it is the only bi-dimensional irreducible representation we have in this order. Also, they are neither symmetric nor anti-symmetric under σ_v or σ_d, so they must belong to this group.

In $n = 3$, we will have four polynomials. Applying the direct product between E_1 and $A_1 \oplus E_2$, we get

$$E_1 \otimes (A_1 \oplus E_2) = E_1 \oplus (E_1 \oplus B_1 \oplus B_2) \tag{A.4.7}$$

Since A_1 is invariant,

$$\begin{aligned} f_{3,1} &= (x + y)\left(x^2 + y^2 + xy\right) \\ f_{3,2} &= (x - y)\left(x^2 + y^2 + xy\right) \end{aligned} \tag{A.4.8}$$

belong to E_1. Let us define two 3^{rd} order polynomials that are orthogonal between each other

$$x^2y + xy^2$$
$$x^2y - xy^2$$

Orthogonalizing these with $f_{3,1}$ and $f_{3,2}$, we get

$$\begin{aligned} f_{3,3} &= x^2y + xy^2 \\ f_{3,4} &= \frac{2}{3}x^3 + x^2y - xy^2 - \frac{2}{3}y^3 \end{aligned} \tag{A.4.9}$$

Do these functions belong to E_1, or do they belong to B_1 and B_2? Taking their scalar product with $f_{1,1}$ and $f_{1,2}$ we get the matrix

$$\begin{bmatrix} \langle f_{3,3}|f_{1,1}\rangle & \langle f_{3,4}|f_{1,1}\rangle \\ \langle f_{3,3}|f_{1,2}\rangle & \langle f_{3,4}|f_{1,2}\rangle \end{bmatrix} = \begin{bmatrix} 0 & 0 \\ 0 & 0 \end{bmatrix} \tag{A.4.10}$$

This shows that these polynomials cannot be in E_1, because $E_1 \otimes E_1$ contains an identity representation, and the integral over the volume of the identity cannot be zero. As $f_{3,3}$ is even under the reflection that swaps $(x, y) \to (y, x)$ and $f_{3,4}$ is odd under this same reflection, $f_{3,3}$ must belong in B_1 and $f_{3,4}$ in B_2.

Let us now look into $n = 4$, where we will have five polynomials. From the direct product table, we know that

$$\begin{aligned} E_1 \otimes E_1 &= A_1 \oplus E_2 \\ E_1 \otimes B_1 &= E_2 \\ E_1 \otimes B_2 &= E_2 \end{aligned} \tag{A.4.11}$$

The A_1 polynomial will be, as in the case of the C_{4v} group, the distance element square

$$f_{4,1} = \left(x^2 + y^2 + xy\right)^2 \tag{A.4.12}$$

As such, the four remaining ones must be in an E_2 irreducible representation. Two of them will come from linear combinations of products of $f_{1,1}$ and $f_{1,2}$ with $f_{3,1}$ and $f_{3,2}$:

$$\begin{aligned} f_{4,2} &= f_{1,1} \times f_{3,1} - f_{1,2} \times f_{3,2} \\ f_{4,3} &= f_{1,1} \times f_{3,2} + f_{1,2} \times f_{3,1} \end{aligned} \tag{A.4.13}$$

For the last two, we take the product of $f_{1,1}$ and $f_{1,2}$ with $f_{3,3}$, and then orthogonalize both of them against $f_{4,2}$ and $f_{4,3}$. From this process, we arrive at (ignoring the normalization factors)

$$\begin{aligned} f_{4,2} &= \left(x^2 + y^2 + xy\right)\left(x^2 + y^2 + 4xy\right) \\ f_{4,3} &= \left(x^4 + x^3y - xy^3 - y^4\right) \\ f_{4,4} &= \left(27x^4 + 143x^3y - 143xy^3 - 27y^4\right) \\ f_{4,5} &= \left(9x^4 - 71x^3y - 178x^2y^2 - 71xy^3 + 9y^4\right) \end{aligned} \tag{A.4.14}$$

For $n = 5$, we know we will have six polynomials. Taking again direct products of E_1 with

the irreducible representation of the polynomials of $n = 4$, we get

$$\begin{aligned} E_1 \otimes A_1 &= E_1 \\ E_1 \otimes E_2 &= B_1 \oplus B_2 \oplus E_1 \end{aligned} \tag{A.4.15}$$

From this decomposition, and as we know that E_1 is bi-dimensional, we will have 4 polynomials coming from both E_1s, and 1 coming from each of B_1 and B_2. The first two are quite simple, as they come from applying the two elements of E_1 to the square of the metric:

$$\begin{aligned} f_{5,1} &= (x+y)\left(x^2+y^2+xy\right)^2 \\ f_{5,2} &= (x-y)\left(x^2+y^2+xy\right)^2 \end{aligned} \tag{A.4.16}$$

Now regarding the other four: one will have to be symmetric under σ_v, one will be anti-symmetric under the same reflection, and the last two will not be either. Calculating them the same way as was done before, we get

$$\begin{aligned} f_{5,3} &= xy\,(x+y)\left(x^2+y^2+xy\right) \\ f_{5,4} &= (x-y)\left(x^2+y^2+xy\right)\left(2x^2+2y^2+5xy\right) \end{aligned} \tag{A.4.17}$$

From observation of the form of these last two polynomials, we know that $f_{5,3}$ must belong to the B_1 irreducible representation, and $f_{5,4}$ must belong to B_2. For the last two, we repeat the same process that we used for the 4^{th} order, obtaining the two final polynomials for this order, which belong to E_1.

$$\begin{aligned} f_{5,5} &= xy\,(x+y)^3 \\ f_{5,6} &= xy\,(x-y)\,(x+y)^2 \end{aligned} \tag{A.4.18}$$

Finally, let us obtain the $n = 6$ polynomials. There are seven of them, and we can obtain them in multiple ways. For simplicity, we will act with $n = 3$ in itself. The group products are the same as before, as we want to calculate

$$(E_1 \oplus B_1 \oplus B_2) \otimes (E_1 \oplus B_1 \oplus B_2) = (A_1 \oplus E_2) \oplus (A_1 \oplus E_2) \oplus (A_1 \oplus E_2) \oplus A_2 \tag{A.4.19}$$

Due to the symmetries of the problem, we will not have an anti-symmetric polynomial. Therefore, due to the dimensions of the irreducible representations, we will have one polynomial from A_1 and 6 (2+2+2) from E_2. The term that belongs in A_1 is again the distance in our coordinate system

$$f_{6,1} = \left(x^2+y^2+xy\right)^3 \tag{A.4.20}$$

Now, using the exact same procedure as before with $f_{3,1}$ and $f_{3,2}$, we get

$$\begin{aligned} f_{6,2} &= xy\left(x^2+y^2+xy\right)^2 \\ f_{6,3} &= \left(x^2-y^2\right)\left(x^2+y^2+xy\right)^2 \end{aligned} \tag{A.4.21}$$

The final four polynomials that all belong, by construction, to the irreducible representation

E_2, are given by

$$\begin{aligned} f_{6,4} &= xy\,(x+y)^2\left(x^2+y^2+xy\right) \\ f_{6,5} &= xy\left(x^2-y^2\right)\left(x^2+y^2+xy\right) \end{aligned}$$

$$\begin{aligned} f_{6,6} &= x^2y^2\,(x+y)^2 \\ f_{6,7} &= (x-y)^2\,(2x+y)^2\,(x+2y)^2 \end{aligned} \tag{A.4.22}$$

We can repeat this process up to any order, and the functions will always be (by construction) orthogonal. By definition of the irreducible representations, and as the Laplacian operator belongs also to the A_1 representation, the Hamiltonian matrix will be diagonal by blocks, with each block belonging to one irreducible representation, which significantly shortens the calculation time.

Up to sixth order, the polynomials are grouped as

$$\begin{aligned} f_0, f_{2,1}, f_{4,1}, f_{6,1} &\to A_1 \\ f_{3,3}, f_{5,3} &\to B_1 \\ f_{3,4}, f_{5,4} &\to B_2 \\ f_{1,1}, f_{1,2}, f_{3,1}, f_{3,2}, f_{5,1}, f_{5,2}, f_{5,5}, f_{5,6} &\to E_1 \\ f_{2,2}, f_{2,3}, f_{4,2}, f_{4,3}, f_{4,4}, f_{4,5}, f_{6,2}, f_{6,3}, f_{6,4}, f_{6,5}, f_{6,6}, f_{6,7} &\to E_2 \end{aligned} \tag{A.4.23}$$

B. Appendix

B.1. Behaviour of $\frac{\mathcal{J}_{m+1}[q_\epsilon R]}{\mathcal{J}_m[q_\epsilon R]} = s$ for $m \in [0, 5]$

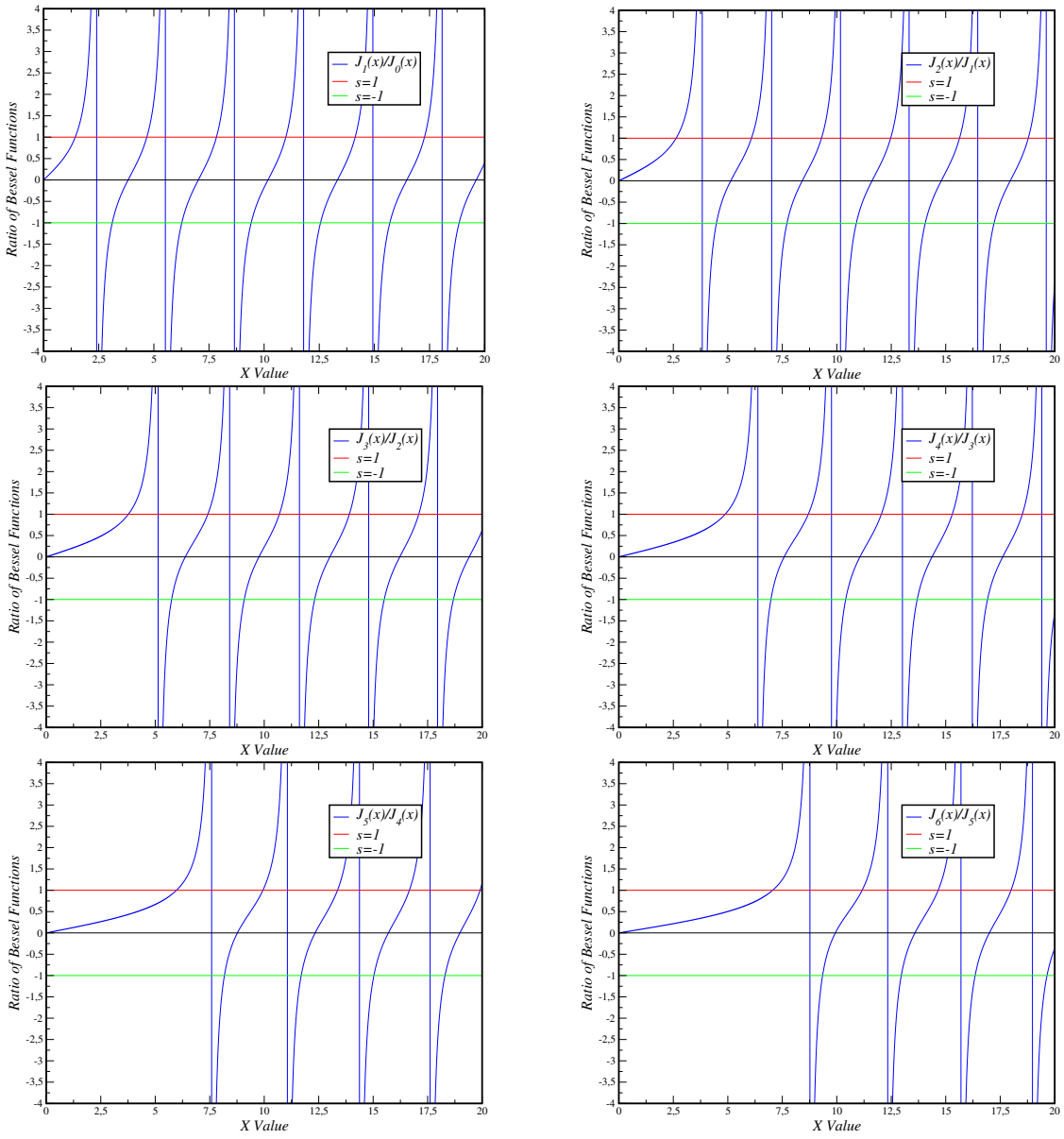

Figure B.1.1.: $\frac{\mathcal{J}_{m+1}[q_\epsilon R]}{\mathcal{J}_m[q_\epsilon R]} = \pm 1$ for $m \in [0, 5]$.

B.2. Density Plots of $\left|\rho^{(+,j)}_{n_1,n_2}(x,y)\right|^2$, $\left|\phi^{(j)}_{n_1,n_2}\right|^2$, and $\left|\chi^{(+,j)}_{n_1,n_2}\right|^2$ for the Triangular Billiard

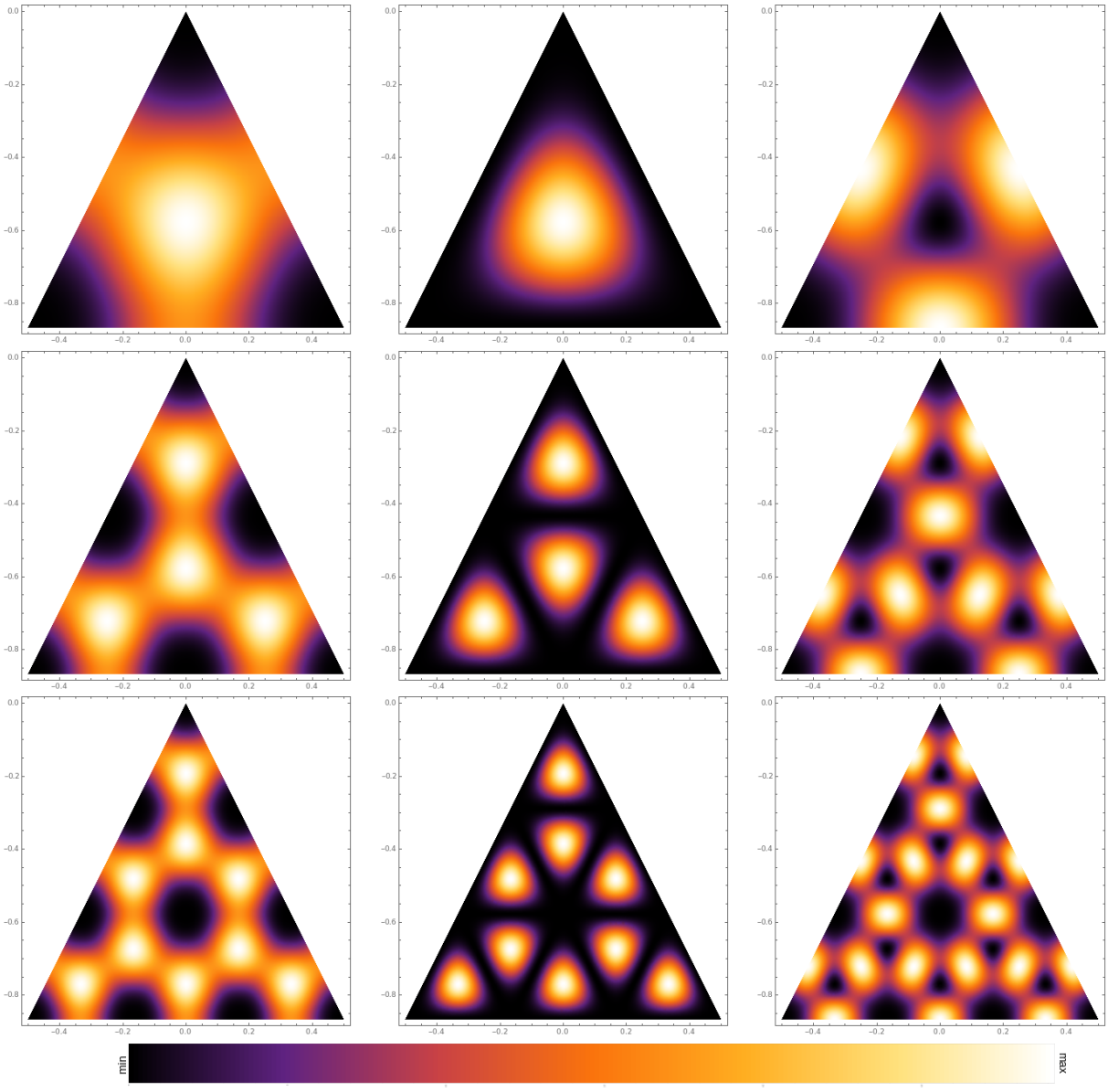

Figure B.2.1.: Left to right, top to bottom: $\left|\rho^{(+,2)}_{n_1,n_1}\right|^2$, $\left|\phi^{(2)}_{n_1,n_1}\right|^2$, $\left|\chi^{(+,2)}_{n_1,n_1}\right|^2$ with $n_1 \in \{1,2,3\}$.

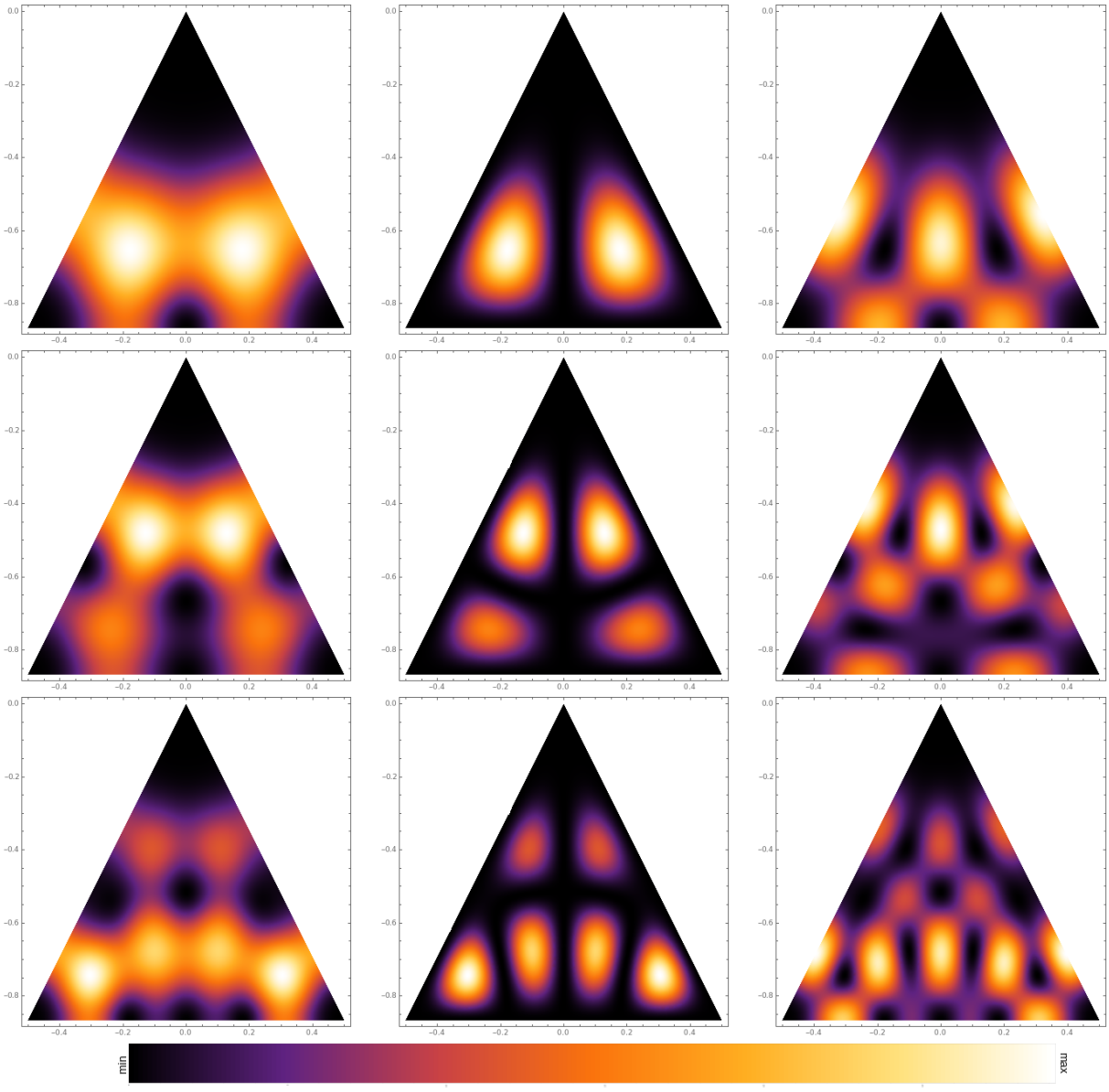

Figure B.2.2.: Left to right: $\left|\rho^{(+,1)}_{n_1,n_2}\right|^2$, $\left|\phi^{(1)}_{n_1,n_2}\right|^2$, $\left|\chi^{(+,1)}_{n_1,n_2}\right|^2$ with $(n_1,n_2)=\{(1,2),(1,3),(2,3)\}$.

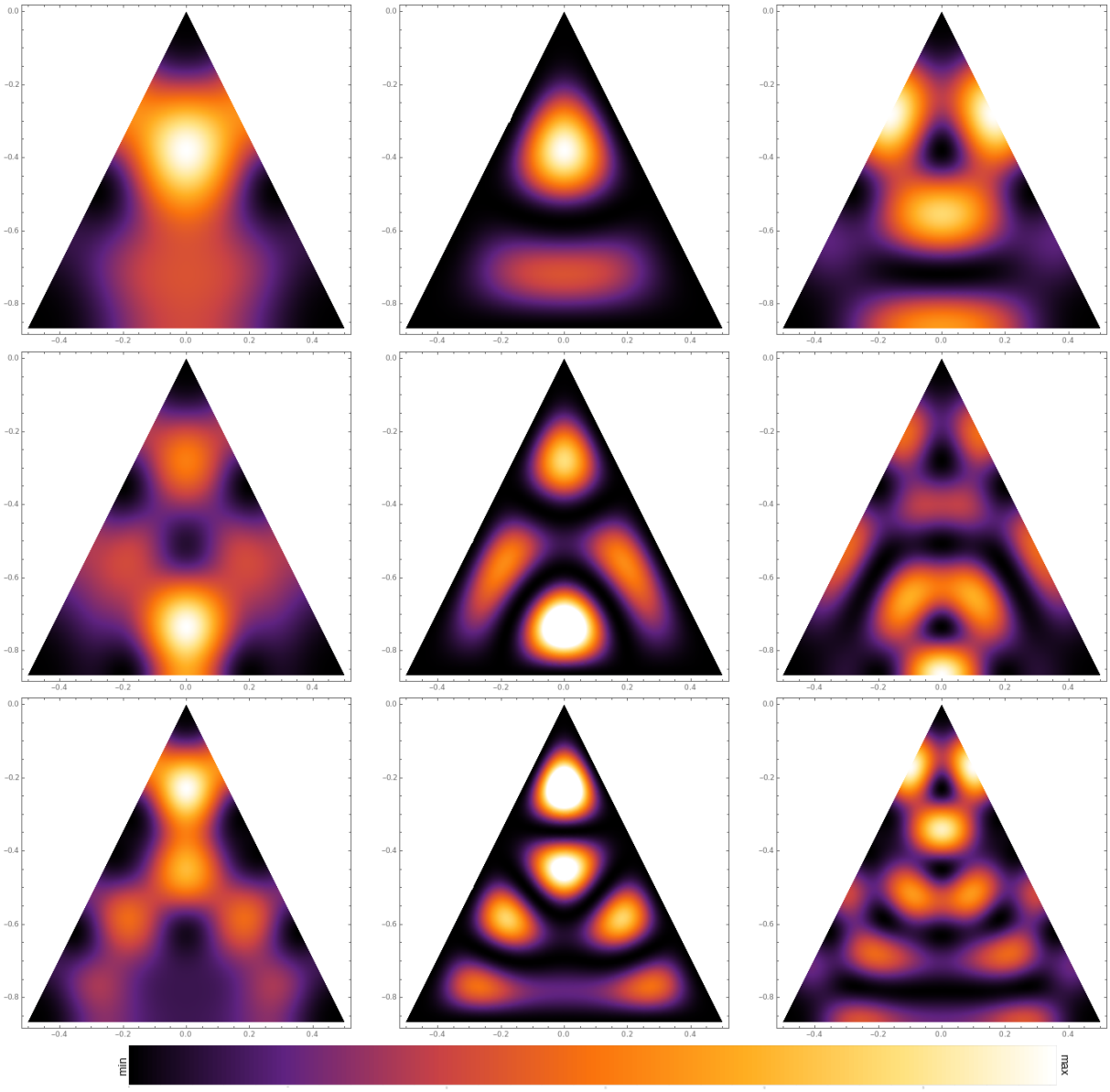

Figure B.2.3.: Left to right: $\left|\rho^{(+,2)}_{n_1,n_2}\right|^2$, $\left|\phi^{(2)}_{n_1,n_2}\right|^2$, $\left|\chi^{(+,2)}_{n_1,n_2}\right|^2$ with $(n_1, n_2) = \{(1,2),(1,3),(2,3)\}$.

B.3. Density Plots of $|\psi_A(x,y)|^2$ for the Lowest Energy Eigenfunctions of the Triangle

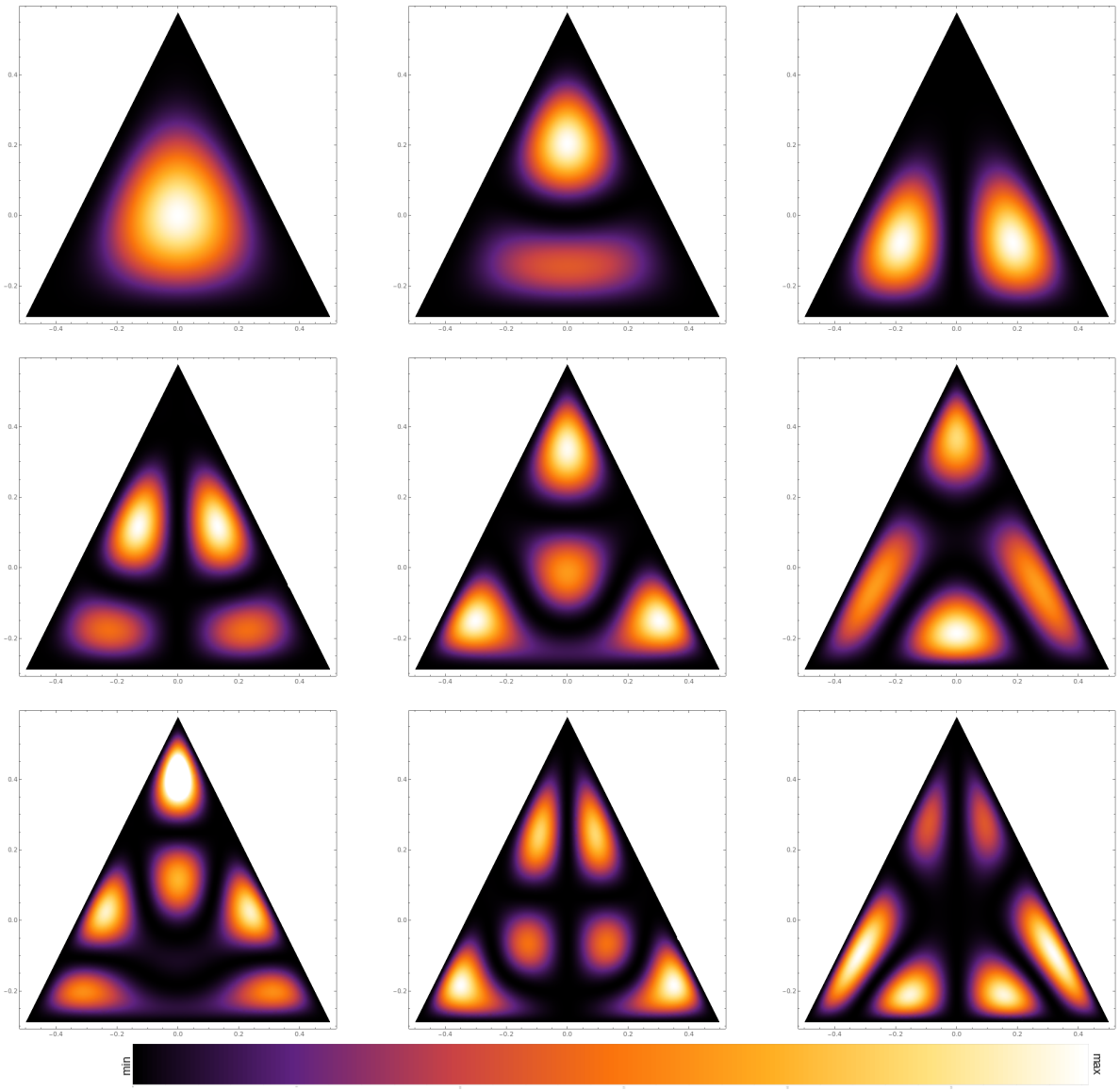

Figure B.3.1.: Density plots of $|\psi_A(x,y)|^2$ for the triangular billiards (energy increasing left to right, top to bottom).

B.4. Density Plots of $|\Psi(x,y)|^2$, $|\psi_A(x,y)|^2$ and $|\psi_B(x,y)|^2$ for the Lowest Energy Eigenfunctions of the Square

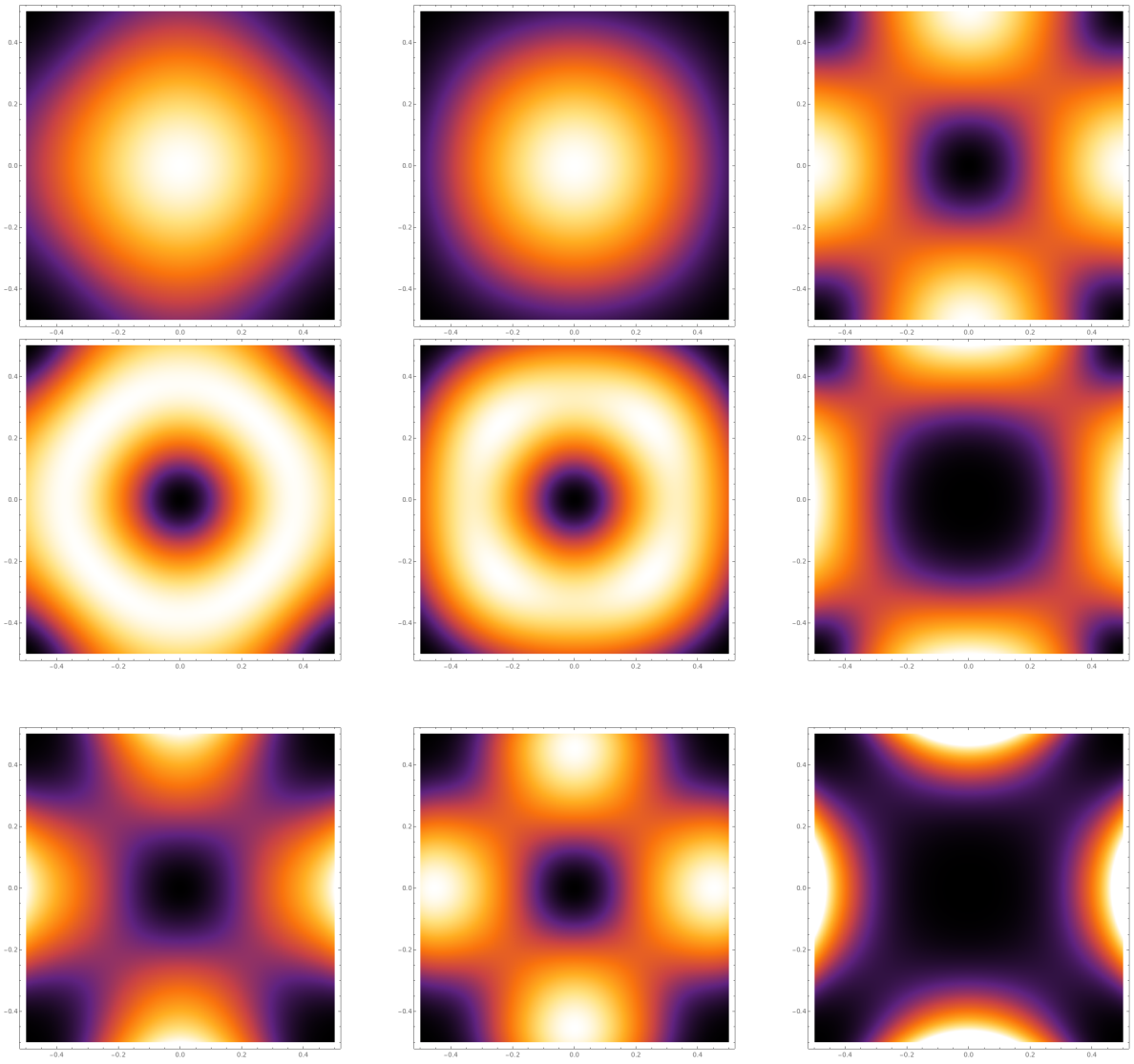

Figure B.4.1.: Density plots of $|\Psi(x,y)|^2$, $|\psi_A(x,y)|^2$ and $|\psi_B(x,y)|^2$ for the first three energy levels of the infinite-mass confined square (energy increasing top to bottom).

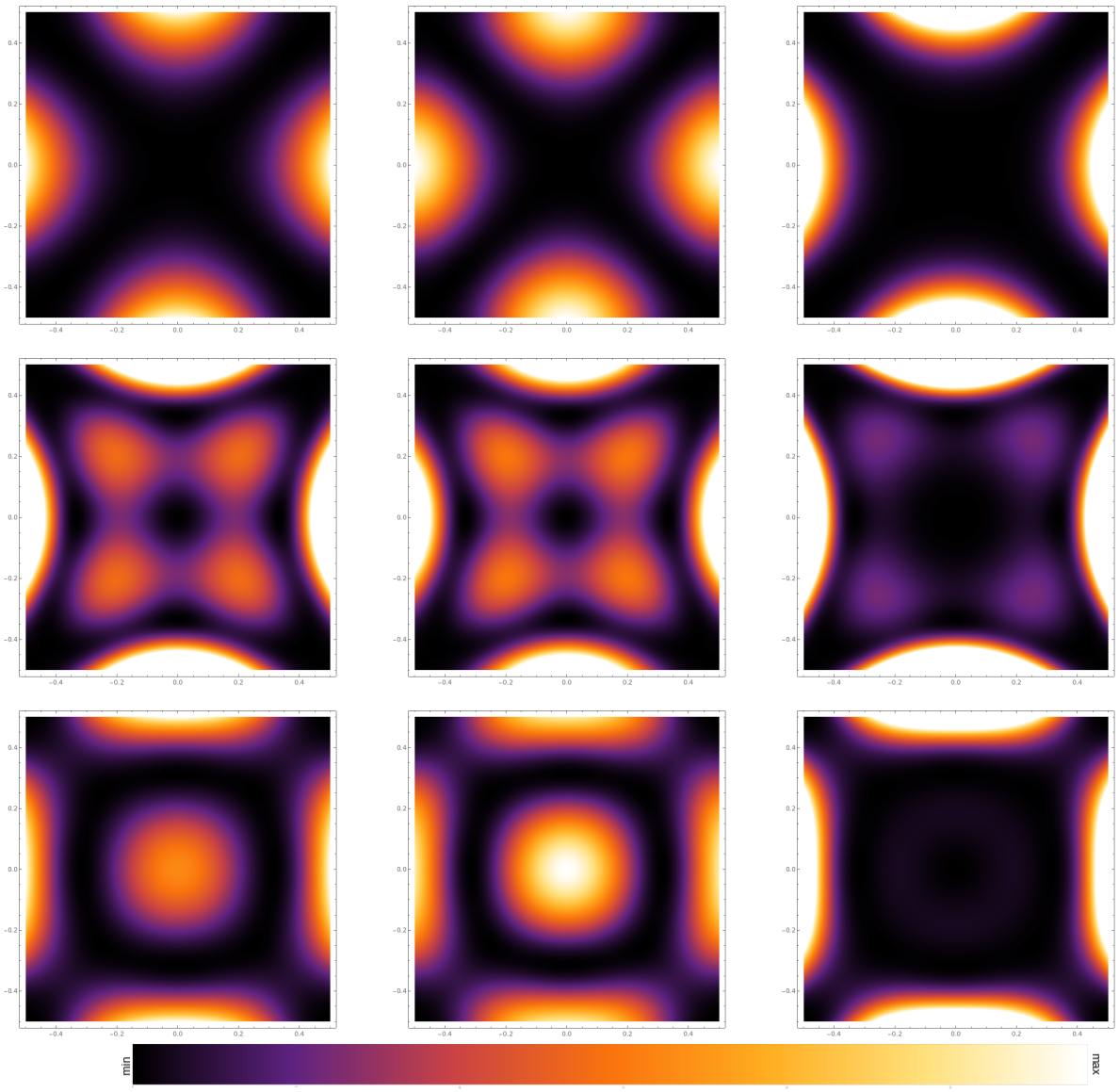

Figure B.4.2.: Density plots of $|\Psi(x,y)|^2$, $|\psi_A(x,y)|^2$ and $|\psi_B(x,y)|^2$ for the second three energy levels of the infinite-mass confined square (energy increasing top to bottom).

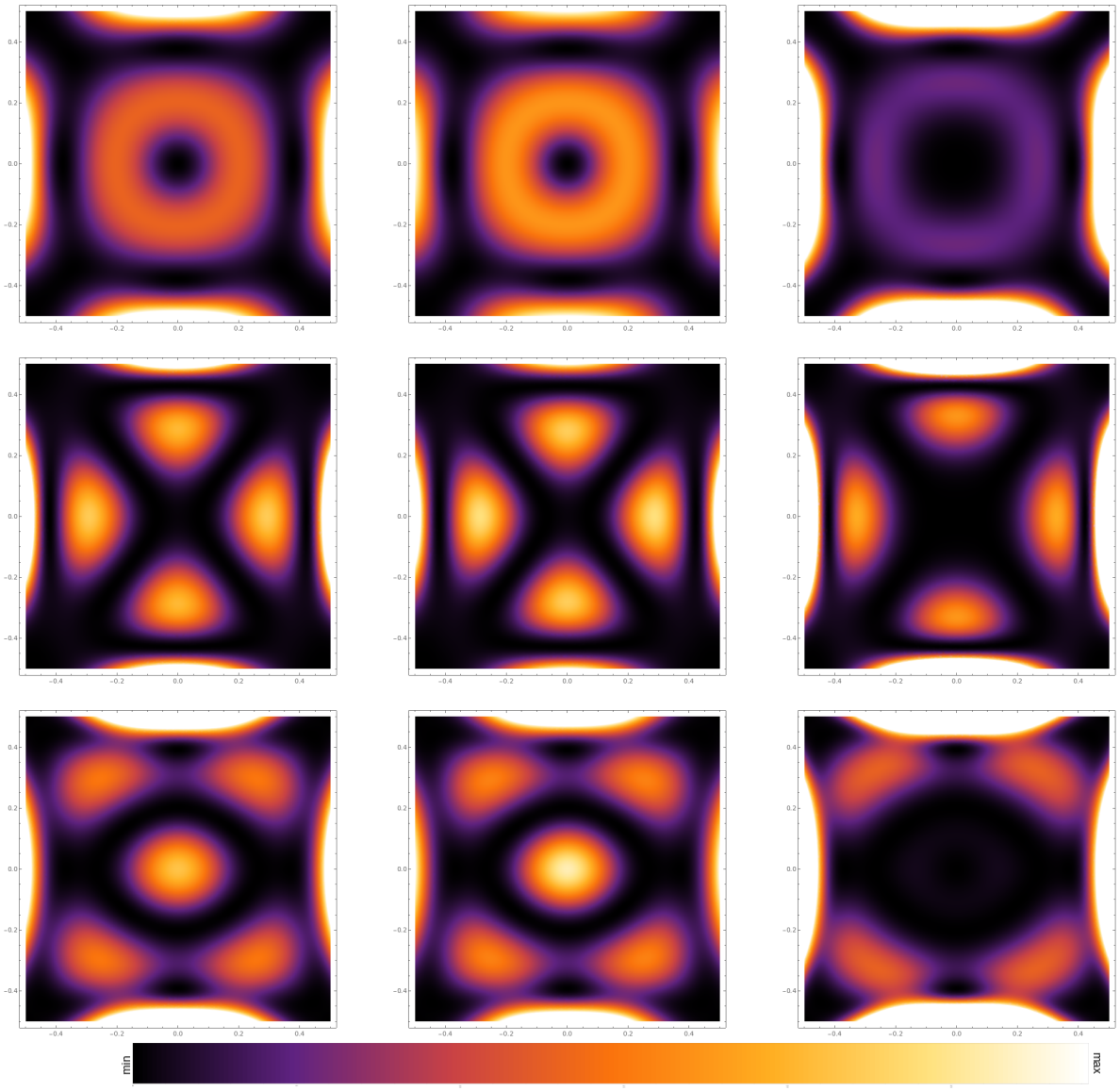

Figure B.4.3.: Density plots of $|\Psi(x,y)|^2$, $|\psi_A(x,y)|^2$ and $|\psi_B(x,y)|^2$ for the third three energy levels of the infinite-mass confined square (energy increasing top to bottom).

B.5. Density Plots of $|\Psi(x,y)|^2$, $|\psi_A(x,y)|^2$ and $|\psi_B(x,y)|^2$ for the Lowest Energy Eigenfunctions of the Hexagon

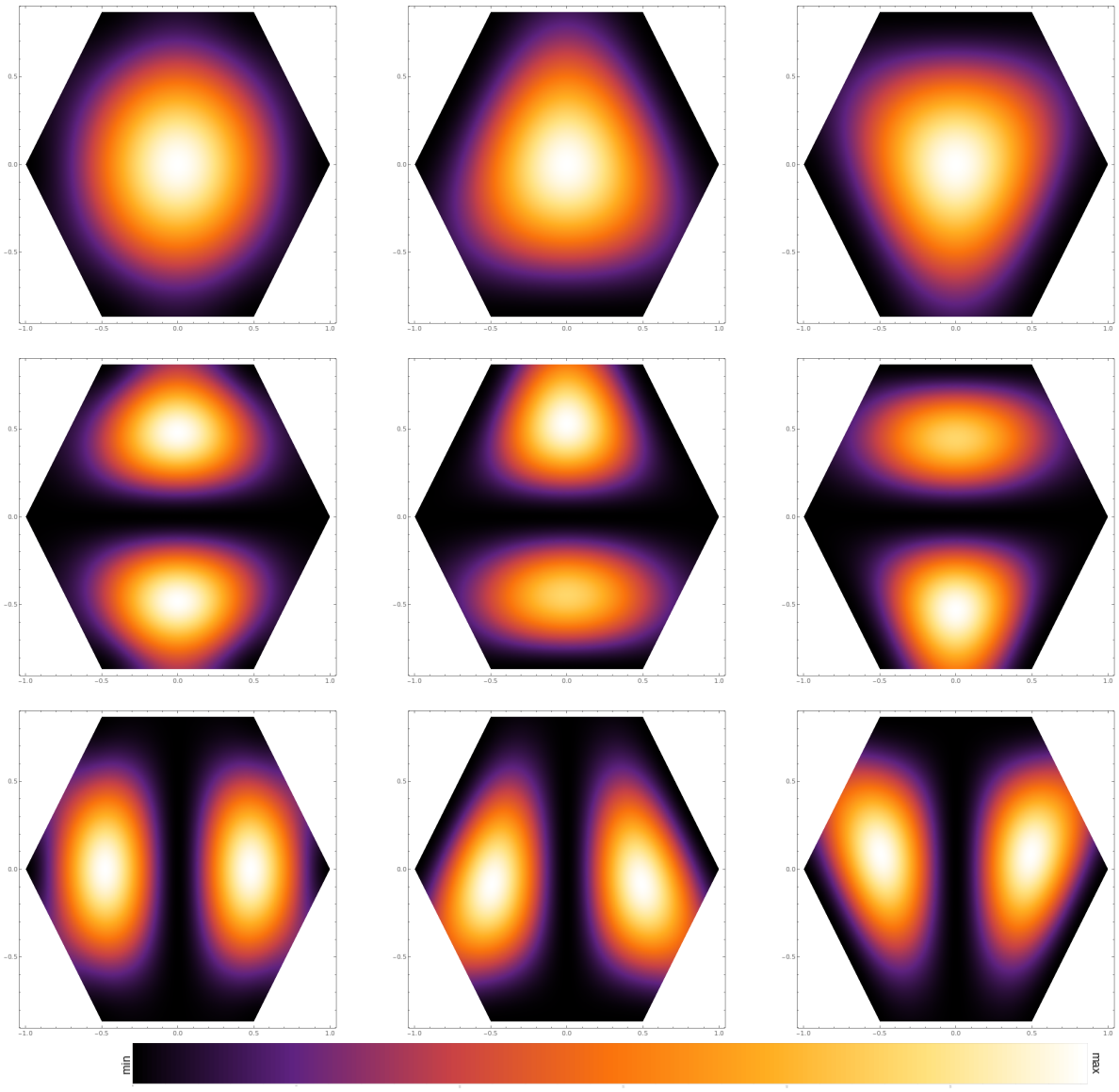

Figure B.5.1.: Density plots of $|\Psi(x,y)|^2$, $|\psi_A(x,y)|^2$ and $|\psi_B(x,y)|^2$ for the first three energy levels of a zigzag-like hexagonal graphene flake (energy increasing top to bottom).

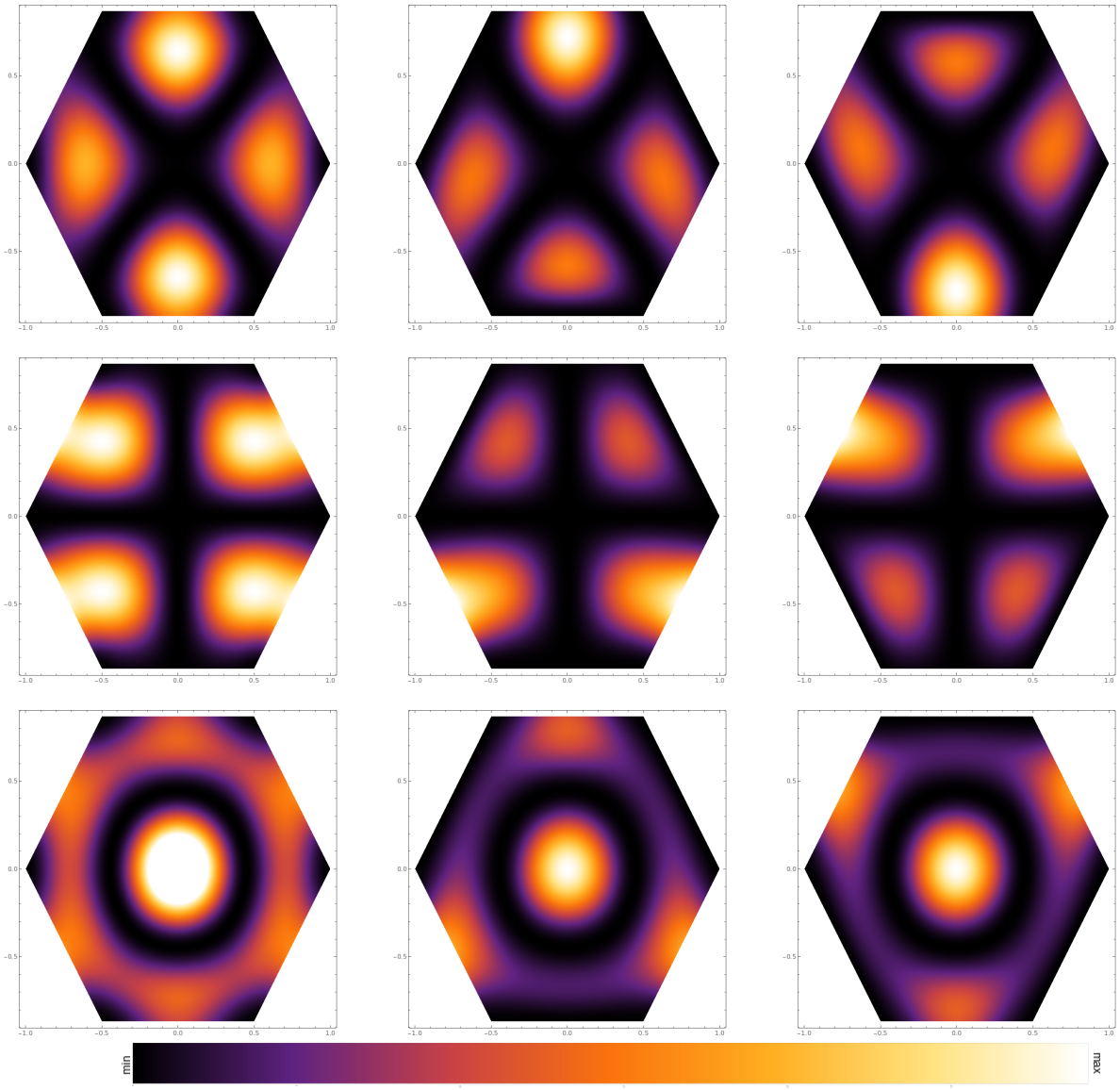

Figure B.5.2.: Density plots of $|\Psi(x,y)|^2$, $|\psi_A(x,y)|^2$ and $|\psi_B(x,y)|^2$ for the second three energy levels of a zigzag-like hexagonal graphene flake (energy increasing top to bottom).

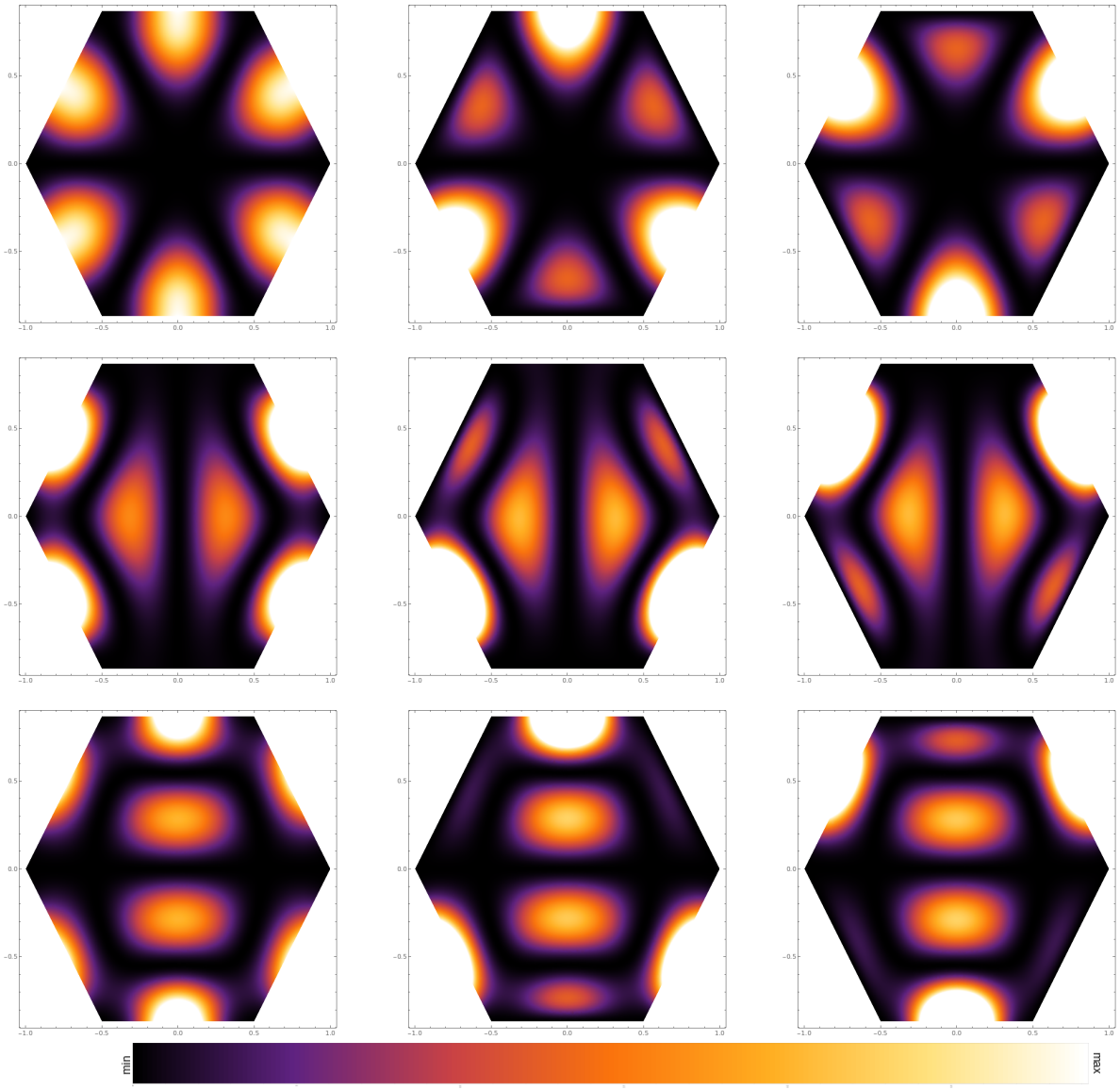

Figure B.5.3.: Density plots of $|\Psi(x,y)|^2$, $|\psi_A(x,y)|^2$ and $|\psi_B(x,y)|^2$ for the third three energy levels of a zigzag-like hexagonal graphene flake (energy increasing top to bottom).

[This page was intentionally left blank]

Bibliography

[1] K. S. Novoselov, A. K. Geim, S. V. Morozov, D. Jiang, Y. Zhang, S. V. Dubonos, I. V. Grigorieva, and A. A. Firsov. Electric Field Effect in Atomically Thin Carbon Films. *Science*, 306(5696):666–669, October 2004.

[2] K. S. Novoselov, A. K. Geim, S. V. Morozov, D. Jiang, M. I. Katsnelson, I. V. Grigorieva, S. V. Dubonos, and A. A. Firsov. Two-dimensional gas of massless Dirac fermions in graphene. *Nature*, 438(7065):197–200, November 2005.

[3] Kirill I. Bolotin, Fereshte Ghahari, Michael D. Shulman, Horst L. Stormer, and Philip Kim. Observation of the fractional quantum Hall effect in graphene. *Nature*, 462(7270):196–199, November 2009.

[4] V. P. Gusynin and S. G. Sharapov. Unconventional Integer Quantum Hall Effect in Graphene. *Physical Review Letters*, 95(14):146801, September 2005.

[5] K. S. Novoselov, E. McCann, S. V. Morozov, V. I. Fal'ko, M. I. Katsnelson, U. Zeitler, D. Jiang, F. Schedin, and A. K. Geim. Unconventional quantum Hall effect and Berry's phase of 2π in bilayer graphene. *Nature Physics*, 2(3):177–180, March 2006.

[6] N. M. R. Peres, F. Guinea, and A. H. Castro Neto. Electronic properties of disordered two-dimensional carbon. *Physical Review B*, 73(12):125411, March 2006.

[7] J. M. B. Lopes dos Santos, N. M. R. Peres, and A. H. Castro Neto. Graphene Bilayer with a Twist: Electronic Structure. *Physical Review Letters*, 99(25):256802, December 2007.

[8] J. M. B. Lopes dos Santos, N. M. R. Peres, and A. H. Castro Neto. Continuum model of the twisted graphene bilayer. *Physical Review B*, 86(15), October 2012.

[9] E. J. Mele. Commensuration and interlayer coherence in twisted bilayer graphene. *Physical Review B*, 81(16):161405, April 2010.

[10] S. Shallcross, S. Sharma, E. Kandelaki, and O. A. Pankratov. Electronic structure of turbostratic graphene. *Physical Review B*, 81(16):165105, April 2010.

[11] Rafi Bistritzer and Allan H. MacDonald. Moiré bands in twisted double-layer graphene. *Proceedings of the National Academy of Sciences*, 108(30):12233–12237, July 2011.

[12] S. Shallcross, S. Sharma, and O. A. Pankratov. Quantum Interference at the Twist Boundary in Graphene. *Physical Review Letters*, 101(5):056803, August 2008.

[13] Yuan Cao, Valla Fatemi, Shiang Fang, Kenji Watanabe, Takashi Taniguchi, Efthimios Kaxiras, and Pablo Jarillo-Herrero. Unconventional superconductivity in magic-angle graphene superlattices. *Nature*, 556(7699):43–50, March 2018.

[14] T. J. Peltonen, R. Ojajärvi, and T. T. Heikkilä. Mean-field theory for superconductivity in twisted bilayer graphene. *Physical Review B*, 98(22):220504, December 2018.

[15] Xianqing Lin and David Tománek. Minimum model for the electronic structure of twisted bilayer graphene and related structures. *Physical Review B*, 98(8), August 2018.

[16] Pilkyung Moon and Mikito Koshino. Energy spectrum and quantum Hall effect in twisted bilayer graphene. *Physical Review B*, 85(19), May 2012.

[17] Long Zhang. Lowest-energy moiré band formed by Dirac zero modes in twisted bilayer graphene. *Science Bulletin*, 64(8):495–498, April 2019.

[18] G. Tarnopolsky, A. J. Kruchkov, and A. Vishwanath. Origin of magic angles in twisted bilayer graphene. *Physical Review Letters*, 122(10):106405, March 2019.

[19] J. Bardeen, L. N. Cooper, and J. R. Schrieffer. Microscopic Theory of Superconductivity. *Physical Review*, 106(1):162–164, April 1957.

[20] R. Peierls. Zur Theorie des Diamagnetismus von Leitungselektronen. *Zeitschrift für Physik*, 80(11):763–791, November 1933.

[21] J. Hubbard and Brian Hilton Flowers. Electron correlations in narrow energy bands. *Proceedings of the Royal Society of London. Series A. Mathematical and Physical Sciences*, 276(1365):238–257, November 1963.

[22] N. F. Mott. The Basis of the Electron Theory of Metals, with Special Reference to the Transition Metals. *Proceedings of the Physical Society. Section A*, 62(7):416–422, July 1949.

[23] Paul Adrien Maurice Dirac and Ralph Howard Fowler. The quantum theory of the electron. *Proceedings of the Royal Society of London. Series A, Containing Papers of a Mathematical and Physical Character*, 117(778):610–624, February 1928.

[24] Hermann Weyl. Elektron und Gravitation. I. *Zeitschrift für Physik*, 56(5):330–352, May 1929.

[25] M. Zarenia, A. Chaves, G. A. Farias, and F. M. Peeters. Energy levels of triangular and hexagonal graphene quantum dots: a comparative study between the tight-binding and the Dirac approach. *Physical Review B*, 84(24):245403, December 2011.

[26] E. Schrödinger. An Undulatory Theory of the Mechanics of Atoms and Molecules. *Physical Review*, 28(6):1049–1070, December 1926.

[27] Wajdi Gaddah. A Lie group approach to the Schrödinger equation for a particle in an equilateral triangular infinite well. *European Journal of Physics*, 34(5):1175–1186, July 2013.

[28] K. M. Liew and K. Y. Lam. A Set of Orthogonal Plate Functions for Flexural Vibration of Regular Polygonal Plates. *Journal of Vibration and Acoustics*, 113(2):182–186, April 1991.

[29] R.B. Bhat. Flexural vibration of polygonal plates using characteristic orthogonal polynomials in two variables. *Journal of Sound and Vibration*, 114(1):65–71, January 1987.

[30] W. A. Gaddah. Exact solutions to the Dirac equation for equilateral triangular billiard systems. *Journal of Physics A: Mathematical and Theoretical*, 51(38):385304, September 2018.

[31] Michiel Hazewinkel. *Encyclopaedia of Mathematics (set)*. Springer Science & Business Media, February 1994.

[32] Dengsheng Zhang and Guojun Lu. A comparative study of fourier descriptors for shape representation and retrieval. In *Proc. of 5th Asian Conference on Computer Vision (ACCV*, pages 646–651. Springer, 2002.

[33] Arthur W. Leissa. *Vibration of Plates*. Scientific and Technical Information Division, National Aeronautics and Space Administration, 1969. Google-Books-ID: TfsfAAAAIAAJ.

[34] K. M. Liew, K. Y. Lam, and S. T. Chow. Free vibration analysis of rectangular plates using orthogonal plate function. *Computers & Structures*, 34(1):79–85, January 1990.

[35] Mark A. Armstrong. *Groups and Symmetry*. Undergraduate Texts in Mathematics. Springer-Verlag, New York, 1988.

[36] Wai-Kee Li and S. M. Blinder. Particle in an equilateral triangle: Exact solution of a nonseparable problem. *Journal of Chemical Education*, 64(2):130, February 1987.

[37] J. J. Sakurai and Jim Napolitano. *Modern Quantum Mechanics by J. J. Sakurai*. September 2017.

[38] J. M. B. Lopes dos Santos. Unpublished notes. 2019.

[39] Berry Michael Victor and Mondragon R. J. Neutrino billiards: time-reversal symmetry-breaking without magnetic fields. *Proceedings of the Royal Society of London. A. Mathematical and Physical Sciences*, 412(1842):53–74, July 1987.

[40] L. Brey and H. A. Fertig. Electronic States of Graphene Nanoribbons. *Physical Review B*, 73(23):235411, June 2006.

[41] Edgardo Stockmeyer and Semjon Vugalter. Infinite mass boundary conditions for Dirac operators. *arXiv:1603.09657 [math-ph]*, March 2016. arXiv: 1603.09657.

[42] G. N. Watson. *A Treatise on the Theory of Bessel Functions*. Cambridge University Press, August 1995.

[43] Carl Ludwig Siegel. *Über einige Anwendungen diophantischer Approximationen*. Akad. de Gruyter in Komm., 1929.

[44] Dean Moldovan, Miša Anđelković, and Francois Peeters. pybinding v0.9.4: a Python package for tight-binding calculations, July 2017.

[45] Alexander Weiße, Gerhard Wellein, Andreas Alvermann, and Holger Fehske. The kernel polynomial method. *Reviews of Modern Physics*, 78(1):275–306, March 2006.

[46] P. Potasz, A. D. Güçlü, and P. Hawrylak. Zero-energy states in triangular and trapezoidal graphene structures. *Physical Review B*, 81(3):033403, January 2010.

[47] M. S. Dresselhaus, G. Dresselhaus, and A. Jorio. *Group theory: application to the physics of condensed matter*. Springer, 1st edition, 2008.

[48] Issai Schur. *Arithmetische Untersuchungen über endliche Gruppen linearer Substitutionen*. 1906.